Models of Single Neurons and Network Dynamics in the Medullary Transverse Slice

A Dissertation
Presented to
The Academic Faculty

by

Liston Keith Purvis

In Partial Fulfillment
of the Requirements for the Degree
Doctor of Philosophy in the
Interdisciplinary Bioengineering Graduate Program
School of Electrical and Computer Engineering

Georgia Institute of Technology
December 2006

Models of Single Neurons and Network Dynamics in the Medullary Transverse Slice

Approved by:

Dr. Robert Butera, Advisor
School of Electrical and Computer Engineering
Georgia Institute of Technology

Dr. Stephen DeWeerth
School of Electrical and Computer Engineering
Georgia Institute of Technology

Dr. Robert Lee
Department of Biomedical Engineering
Emory University

Dr. Ronald Calabrese
Department of Biological and Biomedical Sciences
Emory University

Dr. Jeffery Smith
Cellular and Systems Neurobiology Section
NIH

Date Approved: November 10, 2006

ACKNOWLEDGEMENTS

I would like to take this opportunity to thank several folks who have helped me throughout my graduate career.

I want to thank my advisor, Rob Butera, for always encouraging his students to pursue their interest and for teaching me the skills necessary to become a successful researcher. Rob Butera made significant contributions to the research in this document.

Each member of my Ph.D. committee provided valuable contributions to my research. I want to thank Steve DeWeerth for introducing me to the Neurolab. Steve DeWeerth and Ron Calabrese were both instrumental in helping prepare me for the qualifying exam and guiding my research. I took advantage of Bob Lee's open-door policy more times than I can count, and he always happily provided advice and direction – for that I thank him. Jeff Smith contributed to much of the research in chapters 4 and 5 and was a valuable source of knowledge regarding unfamiliar experimental techniques.

I also want to thank the past and present members of the Butera-group, especially Amanda Preyer and Murat Sekerli who have worked with me for many years. Ya'll have been great! I also want to thank the faculty, staff, and students in the Neurolab.

I want to thank my family and friends for their love and support. My parents, John and Mary Etta Naftel, have been an inspiration to me. Thanks Mom for always loving me so much and encouraging me to excel in my studies.

Finally I want to thank my wife and helper, Deborah, who has given me (at least) three beautiful children. Me you.

TABLE OF CONTENTS

LIST OF TABLES

LIST OF FIGURES

SUMMARY

The pre-Bötzinger complex (pBC) is a sub-circuit of the respiratory central pattern generator. The pBC is required for eupnea and is contained in a transverse slice of the ventrolateral medulla. In the slice, pBC cells are responsible for generating the respiratory rhythm, and hypoglossal motoneurons (HMs) are responsible for transmitting the rhythm out of the brainstem to the muscles. Understanding how the transverse slice rhythm is generated and transmitted is a first step in understanding how this process occurs *in vivo*. To understand this network, we developed ionic current models of the individual network components and explored how the various ion channels affect single-cell firing characteristics and network dynamics. First, we used the considerable amounts of experimental data from neonatal HMs to develop an HM model. The model was used to explore the roles of ion channels in shaping the complex dynamics of the neonatal HM action potential (AP) and to investigate the age-dependent changes in HMs. We used a genetic algorithm to optimize the HM model to more closely fit experimental measures of AP shape. A comparison of feature-based and template-based fitness functions revealed that a feature-based fitness function performs best when optimizing the HM model to fit characteristics of the neonatal HM AP. Next, we used our existing pBC models to understand how different ionic currents affect rhythmogenesis in the pBC. Our results indicate that intrinsic bursters increase the robustness of rhythm generation in the pBC. Finally, we developed an improved pBC neuron model and explored how various ion channels affect bursting dynamics at the single-cell level. The HM and pBC models developed in this study will be used in future network models of the transverse slice.

CHAPTER 1: INTRODUCTION AND BACKGROUND

The production of a robust breathing rhythm is an essential function of the nervous system. The rhythm is generated by a central pattern generator (CPG) network located in the brainstem. Experiments have shown that a subregion of the ventrolateral medulla, the pre-Bötzinger complex (pBC), is critically important for rhythm generation [1, 2]. This network of cells and the associated rhythm can be preserved in reduced experimental preparations, such as the *en bloc* brainstem-spinal cord [3, 4], the sagittal slice [5], and the transverse slice [1]. The most reduced of these preparations, the transverse slice, contains an intact, functional subnetwork of the respiratory CPG with neurons for both the generation and transmission of the respiratory rhythm [1]. The transverse slice is currently the most widely used experimental preparation for studying respiration *in vitro*. Understanding the function of the subnetwork contained in the transverse slice is a first step in understanding how the brain generates and controls the respiratory rhythm *in vivo*.

1.1 Introduction

Despite the vast amounts of research to date, the mechanisms of rhythmogenesis in the pBC are still unknown. Numerous experiments have established that the pBC contains pacemakers, neurons that are capable of bursting in the absence of synaptic input [1, 6-14]. The role of these pacemakers in rhythm generation is currently being investigated in multiple labs, and modeling studies will be critical parts of these investigations. There are many combinations of ionic currents that enable a cell to be a pacemaker. Some of these ionic currents have been found in cells located in the pBC [7, 8, 15-17]. The ionic current underlying at least one type of pacemaker cell in the pBC is the persistent sodium current, a slowly in-activating, sub-threshold inward current [8]. Butera et al. [18, 19] previously developed an ionic current model of a pBC neuron incorporating the persistent sodium current. This minimal model is useful for studying the role of the persistent sodium current in rhythm generation in the pBC. More complex models incorporating the additional ionic currents that exist in the pBC must be developed to explore the roles of these currents in shaping burst dynamics.

The bursting rhythm generated by the pBC is transmitted to the hypoglossal motonucleus in the transverse slice [1]. As with pBC cells, hypoglossal motoneurons (HMs) possess numerous types of ion channels that influence their firing behavior [20]. In addition to the standard depolarizing and hyperpolarizing features of the action potential mathematically described by Hodgkin and Huxley [21], HMs have distinct membrane potential characteristics following the spike [20]. A detailed model of the HM does not yet exist. We will develop ionic current models to understand how various ion channels affect the firing behavior of both HMs and pBC neurons in the transverse slice. Modeling is well suited for this type of study because of the ease with which individual currents can be altered and their amenability to mechanistic analysis. Indeed, modeling allows specification of parameters that are inaccessible in the physical system (e.g. setting the conductance ratios of individual cells). This ability enables investigations that are otherwise impossible.

1.2 Specific Aims

Our long-term goal is to develop network models of the transverse slice that will be used to understand, on a reduced level, how the brain generates and transmits the respiratory rhythm. The objective of this research is to develop the individual component models that will be used in future network models and explore how the model's various ion channels affect single-cell firing characteristics and network dynamics. The respiratory neurons to be modeled include HMs and pBC neurons. The specific aims of this research are:

1. **Develop a single compartment physiological model of a neonatal rat HM.** Extensive experimental work has been done describing the parameters of most currents found in neonatal rat HMs [20]. We will use this data to describe the currents and use hand-tuning of individual parameters to create the HM model. The model will be used to explore the roles of the various ionic currents in HM firing and the age-dependent changes of firing properties observed in these neurons. We hypothesize that variations in specific current densities underlie these age-dependent changes. We will test this hypothesis by varying the maximum conductances of each current and measuring their effects on model output.
2. **Use a genetic algorithm to compare template-based and feature-based fitness functions for optimizing the HM model developed in Aim 1.** Optimization techniques are frequently used to fine-tune model parameters after the modeler has adjusted the parameters to a point where the parameters are "in the ballpark" of the final goal. We will use a genetic algorithm to optimize the parameters of

the HM model developed in Aim 1 to more closely match experimental data. This study will compare three different fitness functions: 1) a template-based fitness function that compares the model output to an ideal action potential waveform, 2) a feature-based fitness function that computes the deviation from the mean of several experimental measures of the action potential, and 3) a combination of the template-based and feature-based fitness functions.

3. **Examine the effects on dynamic range of the inclusion of pacemaker cells in a bursting network.** A currently debated topic in respiratory neurophysiology concerns the role of pacemaker cells in the pBC. Experimental results differ regarding both the number of pacemakers in the pBC and the necessity of those pacemakers in rhythmogenesis. We propose to use experimental data to construct a network model (based on the model of Butera et al. [18, 19]) to investigate the role of pacemaker cells in the pBC. Although pacemakers are not required to produce bursting in the model, we believe including pacemakers in the network will increase the dynamic range of frequencies of oscillations of the network. Simulations will be performed at various levels of synaptic strength and network excitability as the fraction of the network made up of pacemakers is increased.

4. **Develop an improved single-compartment model of a respiratory pBC neuron.** Previous network pBC models generate bursting rhythms [18, 19, 22-25]. Some models accurately incorporate a persistent sodium current as the mechanism for rhythm generation [18, 19, 24]. Those models, however, do not incorporate descriptions of the other ionic currents known to exist in pBC cells, such as low- and high-voltage-activated calcium currents, the A current, and the H

current [15-17]. A model describing these currents will help to reveal their roles in rhythm generation. We propose to develop an improved pBC model with a persistent sodium current as the bursting mechanism. The model will include other ion channels known to exist in pBC cells and their affects on burst dynamics will be explored.

1.3 Background and Significance

Respiration is inextricably linked to survival. Thus, diseases affecting the respiratory rhythm are of paramount importance. Many neurological diseases affect the neural control of respiration [26]. Sudden Infant Death Syndrome (SIDS) is the leading cause of death among infants over one month old. While the cause of SIDS is still unknown, evidence suggests that problems with the neural control of the respiratory rhythm are involved [27-30], and recent evidence points to developmental problems with medullary serotonin receptors [31]. The pBC cells investigated in our study require activation of serotonin receptors to produce a respiratory rhythm [32]. In order to understand and ameliorate the pathophysiology of diseases like SIDS, we must first understand how the brainstem generates and controls the respiratory rhythm.

1.3.1 The Transverse Slice

A breakthrough in respiratory physiology occurred in 1991 when Smith et al. [1] discovered a small region (approximately 300 μm thick) of the medulla that is essential for maintaining the respiratory rhythm [2, 33]. This small region is capable of producing an inspiratory related rhythm after it has been transected from the brainstem (Figure 1). The experimental preparation of Figure 1 is a medullary transverse slice commonly used

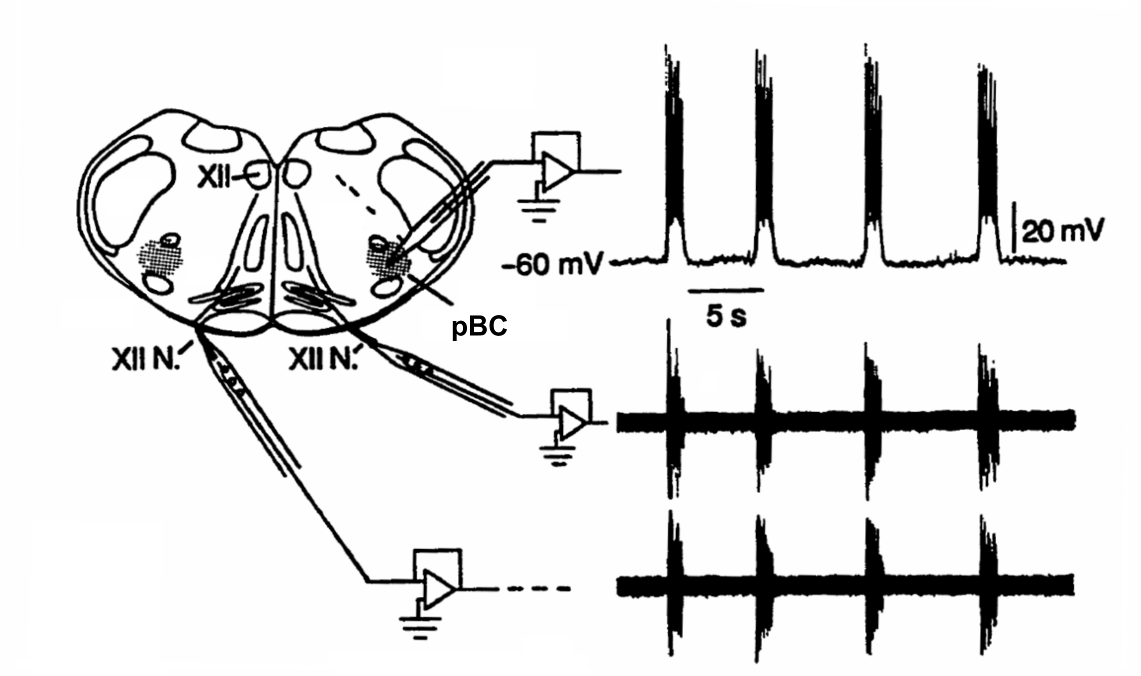

Figure 1. Schematic of the transverse slice containing the pre-Bötzinger complex (pBC) and hypoglossal motoneurons (XII). Recordings from the rootlets of the XII nucleus demonstrate that XII activity follows pBC bursting. Adapted from Smith et al. [1].

for studying respiration *in vitro* and is hereafter referred to as "the transverse slice." The region of cells that generates this rhythm in the transverse slice was named the pre-Bötzinger complex (pBC) [1]. The transverse slice also contains a motoneuron population and a disynaptic pathway from pBC to motor output [1]. This motoneuron population is part of the hypoglossal motonucleus and the ventral roots from this nucleus allow measurement of a population level output from the transverse slice. Analysis of neurons in the transverse slice revealed a possible role of the pBC in respiratory frequency control [34]. Some studies claim that different fictive breathing patterns, such as gasping and sighing, are generated in the slice [35].

What is the mechanism of rhythmogenesis within the pBC? Despite extensive research to date, the details of the mechanisms of rhythmogenesis in the pBC are still not completely resolved. Many experiments have established that the pBC both *in vitro* and in more intact states contains intrinsic bursters or pacemaker neurons – cells that are capable of rhythmic bursting in the absence of synaptic input [1, 6-14]. Furthermore, these and other pBC neurons are coupled by excitatory synaptic connections [13, 36] and the pBC excitatory network itself exhibits autorhythmic properties [37]. Recent literature raises questions about the significance and the abundance of pacemaker cells within the pBC network [7-9, 11, 12, 14, 38]. In the intact respiratory network, the pBC is part of a much larger circuit [39, 40] and pBC cells are responsive to modulation that controls inspiratory frequency [41-44]. Some studies have suggested that the number of pacemakers in the pBC can be dynamically varied by neuromodulators acting on the network [32, 45, 46]. The degree to which pacemakers are essential for rhythm generation in the pBC remains an open issue. Recent studies have shown that blocking pacemakers terminate the respiratory rhythm in all slices [7, 9]. However, boosting neural excitability is able to restore the rhythm in some cases, even after ostensibly blocking all pacemaker activity [9]. Models of the neurons located in the pBC could shed light on this complex problem.

The motoneuron that transmits the breathing rhythm out of the slice is the hypoglossal motoneuron (HM) The HM innervates the tongue and along with its roles in mastication and swallowing, the tongue plays an important role in breathing [30, 47, 48]. The muscle of the tongue contributes to effective breathing by maintaining a patent upper airway and problems with the control of HMs can cause the breathing disorder obstructive sleep apnea [49, 50]. For this reason, extensive experimental work has been done on these motoneurons [20].

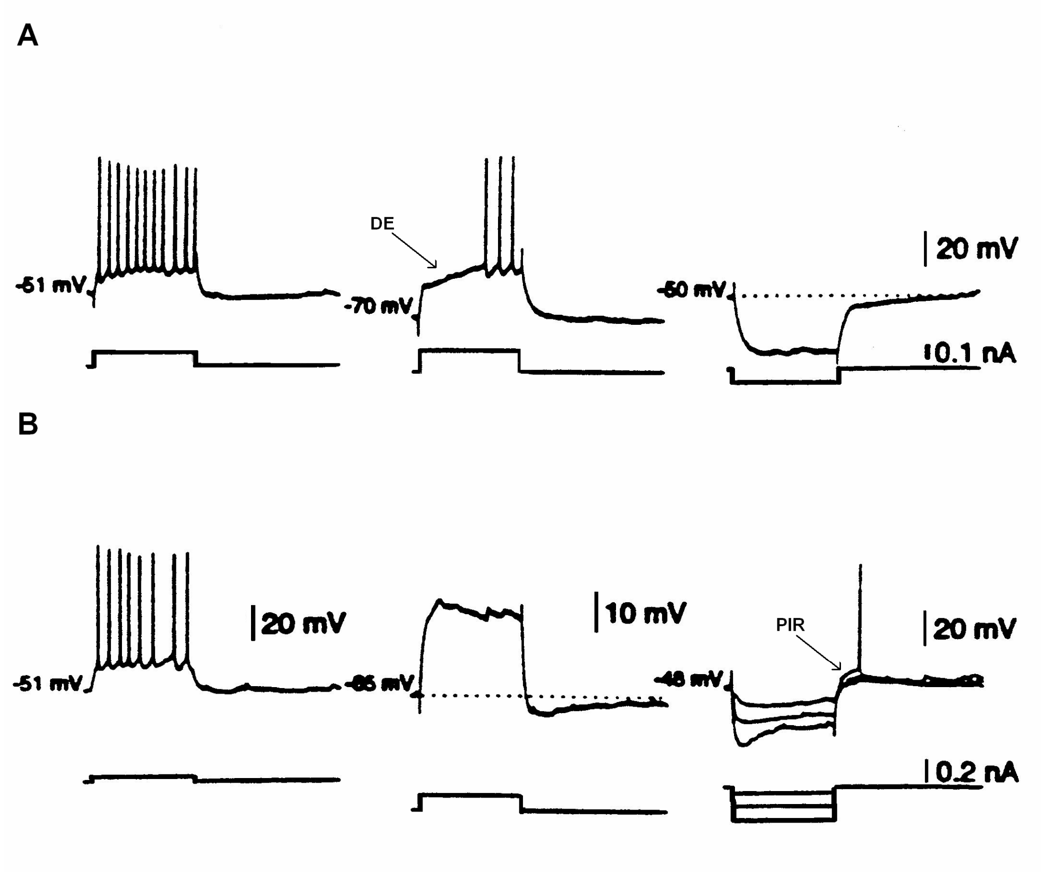

Figure 2. Different types of neurons identified in the pBC. **A**: Delayed excitation (DE) occurs in Type-I neurons after an inhibitory stimulus. **B**: Post-inhibitory rebound (PIR) occurs in Type-II neurons after an inhibitory stimulus. Adapted from Rekling et al. [17].

1.3.2 Experimental Data

Neurons within the pBC have been characterized in different ways. Rekling et al. [17] identified three types of cells based on their responses to hyperpolarizing prepulses. Rekling's Type-I neurons display delayed excitation (DE; Figure 2A). Type-II neurons display post-inhibitory rebound (PIR; Figure 2B). Independent of Type-I and II classification of Rekling et al. [17], Thoby-Brisson and Ramirez [10] have also described two types of bursting neurons in the pBC. These are Cd^{2+}-sensitive and Cd^{2+}-insensitive, based on how bursting is affected when Cd^{2+} replaces Ca^{2+} in the bathing solution (Figure

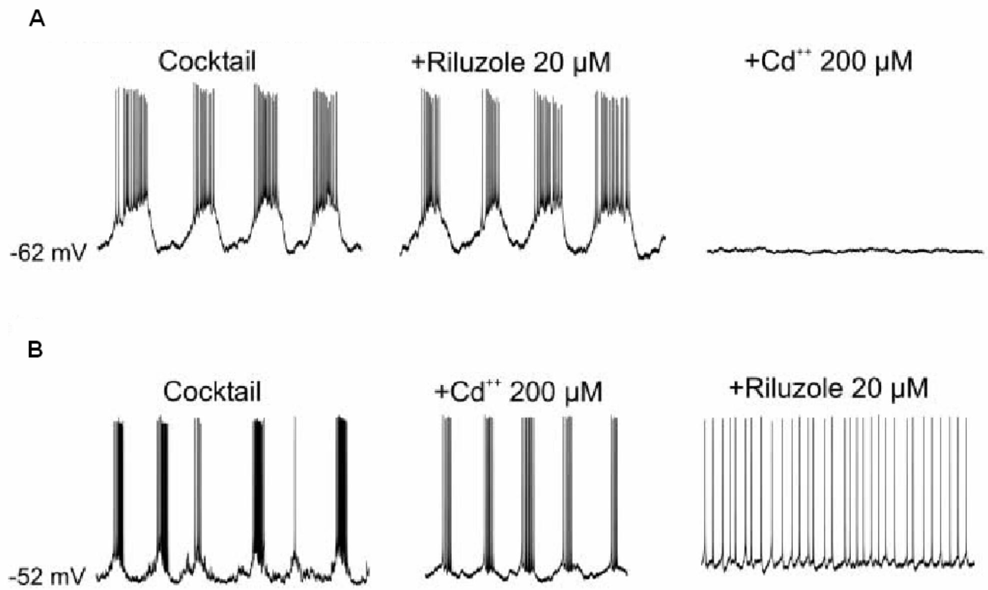

Figure 3. Cadmium-sensitive (**A**) and cadmium-insensitive (**B**) neurons in the pBC. Bursting in cadmium-insensitive neurons is blocked by riluzole. The 'cocktail' is a combination of drugs used to block all synaptic transmission. Adapted from Pena et al. [7].

3A,B). Pena et al. [7] later found that the mechanism that causes Cd^{2+}-insensitive neurons to burst is the persistent sodium current. These appear to be the same pacemakers previously discovered by Smith et al. [1]. Pena et al. [7] also discovered that the Cd^{2+}-sensitive neurons require a calcium-activated nonspecific cation (CAN) current to burst. The Cd^{2+}-sensitive pacemakers are found in the pBC of slice preparations from mice [7, 9, 10, 12], but not rats [9]. All of these results indicate the existence of multiple types of ion channels in the respiratory neurons located in the pBC.

Experiments to characterize the properties of the ion channels located in pBC neurons have been performed in numerous laboratories. Elsen and Ramirez [15, 51] discovered multiple types of calcium currents, and report parameters for the low-voltage activated (LVA) calcium current. They also report parameters for the high-voltage activated (HVA) component of the calcium current. However, the results for the HVA component are a combination of the effects of multiple (perhaps two to four) different HVA currents. The H current is well characterized by Mironov et al. [16]. Recently, Koizumi and Smith [52] obtained parameters for the persistent sodium current of visually identified respiratory neurons in the pBC [13].

The HM has been thoroughly studied for over a decade [20]. Besides the sodium and potassium channels that generate the action potential [53-58], HMs have several different types of calcium channels [56, 57, 59, 60] as well as a calcium dependent potassium channel [58, 61, 62]. HMs also include a hyperpolarization-activated cation channel whose density changes with age [63]. Other age-dependent changes that have been found are input resistance, action potential duration, and firing behavior [64, 65]. The firing behavior of neonatal HMs changes from a decrementing firing pattern during the first week postnatal to an incrementing firing pattern during the second week postnatal [65]. The various ion channels in HMs are responsible for the complex action potential shape that includes a fast after-hyperpolarization (fAHP), an after-depolarization (ADP) and a medium duration after-hyperpolarization (mAHP; Figure 4). It has been suggested that some of the age-dependent behaviors of HMs are caused by the age-dependent changes in conductance densities of ion channels [63]. Models of these neurons can be used to explore possible mechanisms for the age-dependent changes.

1.3.3 Previous Models

Various pBC models have been developed to explain how the respiratory rhythm is generated. Rybak et al. [22, 23] developed the first respiratory network model whose component neurons incorporate ion channel properties. In this model, the rhythm is

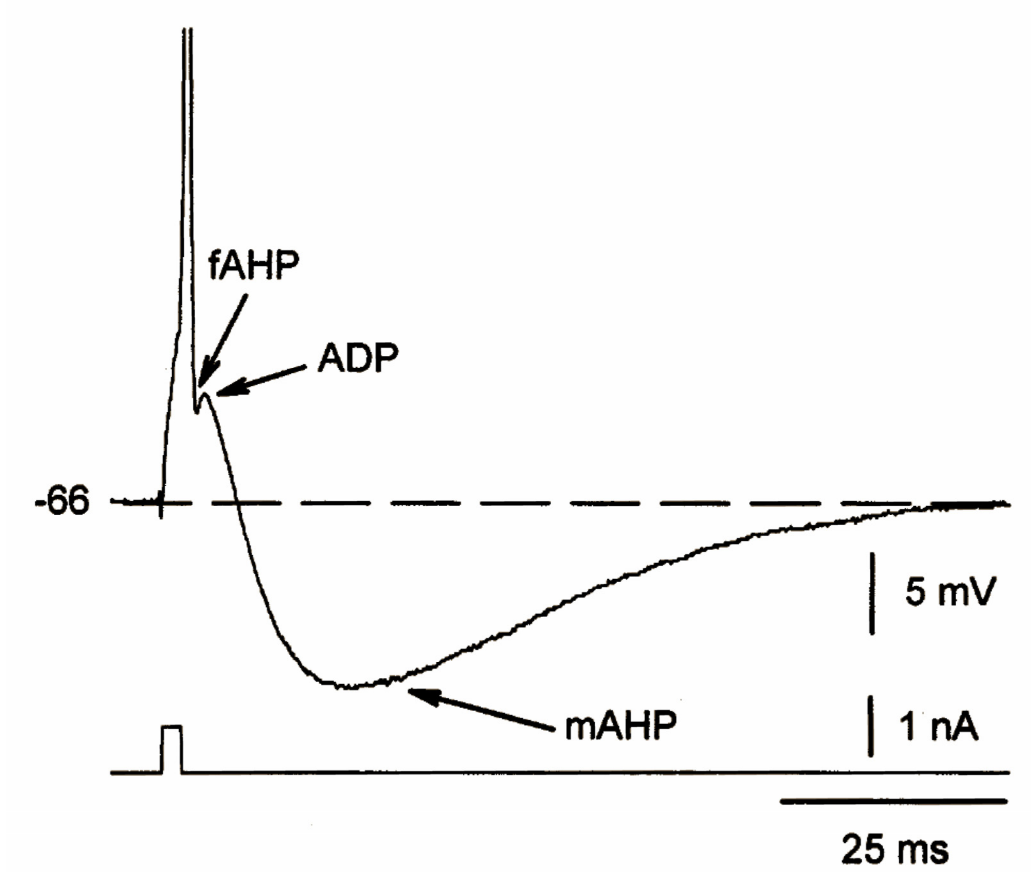

Figure 4. HM action potential. The action potential is evoked by a brief (1 ms) current pulse of 1 nA. The action potential is truncated to emphasize the fAHP, ADP, and mAHP following the spike. Adapted from Berger [20].

generated by network interactions of two types of model neurons: one type showing spike-frequency adaptation, and the other type showing spike-frequency augmentation. Later, Butera et al. [18, 19] developed a minimal, four current model of pBC cells with a different bursting mechanism, the persistent sodium current. This model appears to be more physiological because the persistent sodium current has been shown to cause bursting in some pBC cells [8]. Butera's model accurately reproduces many of the single-cell and network behaviors found in the transverse slice [66]. Rybak et al. [24, 67] extended Butera's model by measuring parameters for the persistent sodium current and including them in the model. With the more accurate parameters, the model reproduces results similar to those of Butera et al. [18, 19]. A third mechanism that causes bursting was modeled by Kosmidis et al. [25]. This mechanism uses a calcium-dependent potassium current with parameters for the model taken from a thalamic relay neuron model. This model also reproduces results similar to those of Butera et al. [18, 19]. None of these models incorporate the many ionic currents now known to exist in pBC neurons [15, 16, 51].

While there is a vast amount of data describing the ionic currents in neonatal HMs, there are no published neonatal HM models. However, models have been developed for adult HMs. Powers et al. [68] developed threshold-crossing motoneuron models to explore the three phases of adaptation seen in adult HMs.

1.3.4 Genetic Algorithms

Manual tuning of model parameters can be a complicated task, especially when using large models with many parameters. Optimization techniques are frequently used to fine-tune model parameters after the modeler has adjusted the parameters to a point where the parameters are "in the ballpark" of the final goal. When manually optimizing a model to meet specific requirements, if the modeler is biased towards only varying certain parameters based on an intuition of the sensitivity of those parameters, then other potentially important parameters may be disregarded. By using an automated optimization technique, the modeler hopes to more closely match experimental data and eliminate unintentional bias.

A Genetic Algorithm (GA) is a popular, biologically inspired optimization method. The GA starts with an initial population of models with randomly chosen parameters, and proceeds by letting the population evolve using mechanisms inspired by the idea of natural selection. Each model in the population is tested for fitness and assigned a score. This fitness score is the basis for that model's likelihood of reproducing (through crossover) and retention for subsequent generations. The desire is that with each generation, characteristics (parameter values) of the best performing individuals (models) will combine to produce better individuals. Researchers have previously used GAs for parameter optimization of neurons models [69-72] and models of other excitable cell types [73].

CHAPTER 2: HYPOGLOSSAL MOTONEURON MODEL

We begin this project by developing an ionic current model of a neonatal hypoglossal motoneuron (HM). HMs transmit the breathing rhythm out of the transverse slice to the effector muscles responsible for maintaining a patent upper airway during respiration. The neonatal rat HM contains a repertoire of ionic currents that have been thoroughly investigated in both current- and voltage-clamp studies. These experimental studies provide the basis for the ionic currents included in this model.

We have developed a single-compartment, electrophysiological, HM model based primarily on experimental data from neonatal rat HMs. The model is able to reproduce the fine features of the HM action potential: the fast after-hyperpolarization, the after-depolarization, and the medium-duration after-hyperpolarization (mAHP). The model also reproduces the repetitive firing properties seen in neonatal HMs, and replicates the neuron's response to pharmacological experiments. The model was used to study the role of specific ionic currents in HM firing, and how variations in the density of these currents may account for age-dependent changes in excitability seen in HMs. By varying the density of a fast inactivating calcium current, the model alternates between accelerating and adapting firing patterns. Modeling the age-dependent increase in H current density accounts for the decrease in mAHP duration observed experimentally, but does not fully account for the decrease in input resistance. An increase in the density of the voltage-dependent potassium currents and the H current is required to account for the decrease in input resistance. These changes also account for the age-dependent decrease in action potential duration.

2.1 Methods

In this section, we will describe the equations used to implement the HM model. The model is based on a single-compartment Hodgkin-Huxley formalism [21].

2.1.1 Simulations

Simulations were performed using the interactive differential equation simulation package XPP [74]. The integration was done using the Dormand-Prince integrator built into XPP. MATLAB (Mathworks, Natick MA) was also used for model formulation and data analysis.

2.1.2 Formulation of Model

The membrane potential is found using the differential equation

$$\frac{\mathrm{dV}}{\mathrm{dt}} = \frac{1}{\mathrm{C_m}}\left(-\sum I_{ionic} + I_{stim}\right)$$

where V is the membrane potential (mV), C_m is the whole cell capacitance (nF), t is time (ms), I_{stim} is the applied stimulus current (nA), and I_{ionic} are the ionic currents listed in APPENDIX A and have the form

$$I_{ionic} = g\left(V - E_{ionic}\right)$$

where E_{ionic} is the equilibrium reversal potential for the ionic species carried by the current and

$$g = \bar{g}x$$

where $\bar{g}$ is the maximum conductance of each current, and *x* is the product of one or more gating variables raised to integer powers, as described below.

The dynamics of the conductances of the ionic currents regulated by voltage-dependent activation or inactivation variables are described according to

$$\frac{dx}{dt} = \frac{x_\infty(\mathrm{V}) - x}{\tau_x(\mathrm{V})}$$

$$x_\infty(\mathrm{V}) = \frac{1}{1 + e^{(\mathrm{V} - \theta_x)/\sigma_x}}$$

$$\tau_x(\mathrm{V}) = \frac{\mathrm{A}}{e^{(\mathrm{V} - \theta_1)/\sigma_1} + e^{-(\mathrm{V} - \theta_2)/\sigma_2}} + \mathrm{B}$$

where $x_\infty(V)$ is the steady-state voltage-dependent (in)activation function of x and $\tau_x(V)$ is the voltage-dependent time constant. $x_\infty(V)$ is a sigmoid with a half-(in)activation at $V = \theta_x$ and a slope factor σ_x. $\tau_x(V)$ is a bell-shaped curve. If no experimental data exist for time constant measurements, or no significant change in the model results from including a voltage-dependent time constant, it is represented by a constant, B.

The dynamics of the calcium-dependent potassium (SK) conductance is described according to the same equation for dx/dt, but $x_\infty(V)$ is replaced by a Michaelis-Menten binding curve with a Hill coefficient of 2:

$$skz_\infty\left([Ca^{2+}]_i\right) = 1 \Big/ \left(1 + \left(\frac{\theta_c}{[Ca^{2+}]_i}\right)^2\right)$$

where $[Ca^{2+}]_i$ is the internal calcium concentration of the cell with a half-activation at $[Ca^{2+}]_i = \theta_C$. This SK current model was previously used by Engel et al. [75].

The modeling of calcium dynamics is performed by considering the cell to contain a single compartment with intracellular calcium accumulation and degradation of the form

$$\frac{d[Ca^{2+}]_i}{dt} = K_1 I_{ca} - K_2 [Ca^{2+}]_i$$

where I_{Ca} is the sum of the three calcium currents, K_1 is an accumulation scaling factor, and K_2 is a decay rate constant that represents calcium uptake and diffusion. A similar model has been used by other investigators in the past [76, 77]. In the model, the calcium-activated potassium (SK) current is the only current whose conductance depends on the internal calcium concentration.

All state variables and initial conditions are listed in Table 1. The maximum conductance and reversal potential for each current, along with various other parameters are listed in Table 2.

Table 1. Initial conditions for HM model.

$V(0) = -71.847$ mV
$m(0) = 0.015$
$h(0) = 0.981$
$m_{NaP}(0) = 0.002$
$h_{NaP}(0) = 0.797$
$n(0) = 0.158$
$m_T(0) = 0.001$
$h_T(0) = 0.562$
$m_P(0) = 0$
$m_N(0) = 0.001$
$h_N(0) = 0.649$
$z_{SK}(0) = 0$
$m_A(0) = 0.057$
$h_A(0) = 0.287$
$m_H(0) = 0.182$
$[Ca^{2+}]_i(0) = 0.0604$ μM

Table 2. Parameter values for HM model.

$\bar{g}_{Na}$ = 0.7 μS	$\bar{g}_{H}$ = 0.005 μS
$\bar{g}_{NaP}$ = 0.05 μS	E_{Na} = 60 mV
$\bar{g}_{K}$ = 1.3 μS	E_{K} = -80 mV
$\bar{g}_{leak}$ = 0.005 μS	E_{leak} = -50 mV
$\bar{g}_{T}$ = 0.1 μS	E_{Ca} = 40 mV
$\bar{g}_{P}$ = 0.05 μS	E_{H} = -38.8 mV
$\bar{g}_{N}$ = 0.05 μS	K_{1} = -0.0005 M/nC
$\bar{g}_{SK}$ = 0.3 μS	K_{2} = 0.04 ms^{-1}
$\bar{g}_{A}$ = 1.0 μS	C_{m} = 0.040 nF

Sensitivity analysis [78, 79] is used to determine the sensitivity of the membrane voltage to changes in maximum conductances. For a description of this method, see APPENDIX B.

2.2 Model Development

The model incorporates a fast and a persistent sodium current, a delayed rectifier and a fast transient potassium current, one low- and two high-voltage activated calcium currents, a calcium-dependent potassium current, and a hyperpolarization-activated cationic current. A detailed description of the basis for each of these currents is given below.

2.2.1 Sodium Currents.

HMs have a fast sodium current (I_{Na}) that when blocked by TTX removes the ability of the cell to generate an action potential [53, 54, 57]. In addition, the voltage-ramp data of Powers and Binder [56] suggests the existence of a persistent sodium current (I_{NaP}) in HMs. That data shows an increase in sodium current with increased ramp speed, and no decrease in sodium current at voltages above -30mV after application of TTX. This indicates a slowly inactivating sodium current (in this composition, persistent will mean slowly inactivating). Lape and Nistri [54] present voltage clamp data for the sodium current, but do not distinguish between the fast sodium and persistent sodium currents as was done by Rybak et al. [24]. Therefore, parameters for the fast sodium current in the model are more depolarized than the data of Lape and Nistri [54]. Since the persistent sodium current has not yet been fully described in HMs, the parameters for this current are based on data from other neurons [24, 80]. Kononenko et al. [80] report a time constant of inactivation of 50-250 ms at the peak of activation. The value for the time constant of inactivation of I_{NaP} chosen for the model is in this range ($\tau_{NaP}(V)$ = 150 ms).

2.2.2 Voltage-Dependent Potassium Currents.

Another current found in rat HMs is a TEA sensitive potassium current (I_K), the delayed-rectifier [53, 55, 58]. HMs also possess a potassium current that is sensitive to 4-aminopyridine (4-AP). This current is thought to be the fast transient A-type current [55, 58]. Viana et al. [58] show a dose-dependent increase in action potential duration with application of TEA and 4-AP in neonatal rat HMs, indicating the importance of both of these currents in shaping the action potential. Parameters for I_K and I_A in the model are based on the voltage clamp data of Lape and Nistri [55, 61], though the time constants used are faster than the reported values in order to produce an appropriate action potential duration (less than 2 ms) [64]. The model does not distinguish between (in)activation and de(in)activation as reported for the time constant data of I_A [55].

2.2.3 Calcium Currents.

It has been shown that rat HMs have both low-voltage-activated (LVA) and high-voltage-activated (HVA) calcium currents [56, 57, 59, 60]. The LVA calcium current is a T-type current [59]. The properties of the T-type current were found by characterizing the residual current after application of antagonists to the three HVA currents. The three HVA currents found in HMs are P-type, N-type, and L-type [56, 60]. Umemiya and Berger [60] report half-(in)activation and time constant values for these currents found by single channel recordings. The time constants used in the model are based on these recordings, however, the half-(in)activation values are shifted to a more depolarized value in order to provide a better fit to whole-cell data [57, 59]. The half-activation value for I_N required a considerable hyperpolarizing shift (55 mV) from the reported value of 25 mV in order to provide a significant contribution to the total calcium current that is consistent with the whole-cell data. The L-type HVA current in HMs has dynamics similar to that of the P-type channel (i.e. non-inactivating, high-voltage-activated) [60]. However, the L-type current makes up less than 10% of the total calcium current [56, 59]. For these reasons, the L-type current is not included in this model.

2.2.4 Calcium-Activated Potassium Current.

One essential feature of rat HMs is the medium-duration afterhyperpolarization (mAHP) following the action potential (see Figure 5). Previous experimental work has shown that the mAHP in rat HMs is calcium dependent, has a reversal potential near that of potassium, and is blocked by apamin [58, 61, 62]. This indicated the existence of the calcium activated potassium current, or SK current (I_{SK}). Lape and Nistri [61] made several important observations by subtracting outward currents measured from voltage-clamp data before and after application of apamin: 1) membrane depolarizations as short as 1 ms produce enough calcium entry to evoke measurable SK currents, 2) the membrane conductance underlying I_{SK} is voltage independent, 3) apamin does not affect resting membrane potential, suggesting I_{SK} is not activated at resting calcium concentrations, and 4) the I-V relation indicated an activation region between -40 and -10 mV. The model uses a non-inactivating and voltage independent conductance that activates with an increase in internal calcium concentration, similar to that used by other researchers [75]. This current, along with the model of internal calcium, satisfies the observations listed above through: 1) fast activation, 2) no voltage dependent gating variables, 3) an appropriate half-activation calcium level, and 4) dependence on activation of calcium currents in the -40 to -10 mV range.

2.2.5 Hyperpolarization-activated Cationic Current.

HMs also have a hyperpolarization-activated cationic current (I_H) that displays a large increase during postnatal development [53, 63]. In neonatal rat HMs, the H current is only about one-tenth the density of that in adult rat HMs [63]. The H current activates much more slowly than the other currents in HMs, with a peak activation time constant greater than 200 ms (compared to ~ 10 ms for the calcium currents).

2.2.6 Passive Properties.

The membrane capacitance of the model is set to match experimental data [55, 59]. Resting potential and input resistance (R_N) were set to match experimentally determined values for neonatal rat HMs [64] by adjusting the maximum conductances of the currents active at rest. The model's resting membrane potential is -72 mV. This value is within the range measured by many different observers for neonatal HMs [53, 61, 64]. The R_N of neonatal rat HMs is reported to be about 35 MΩ by Viana et al. [64], about 120 MΩ by Robinson and Cameron [81], and about 400 MΩ by Lape and Nistri [55]. The large difference in observed R_N is probably due in part to the different recording techniques and the use of sharp electrodes [64] vs. whole-cell patch-clamp [55, 81]. The difference between the two values found using whole-cell patch-clamp techniques could be due to the time elapsed before recording R_N, as suggested by Robinson and Cameron [81]. The R_N of the model is around 40 MΩ, closer to that reported by Viana et al. [64].

2.2.7 Maximum Conductances.

As stated above, the maximum conductances of the currents active at rest were set to match experimental data for R_N and resting potential. Also, the maximum conductance of I_{Na}, I_{NaP}, I_K, and I_A were adjusted in order to provide an action potential of the appropriate amplitude and duration [64]. The maximum conductance of the calcium currents were then constrained to match whole-cell voltage-clamp data [57, 59]. The maximum conductance of I_{SK} was chosen to provide a mAHP of appropriate amplitude and to reproduce the behaviors seen during repetitive firing [58, 61, 64, 65]. The maximum conductance of I_H was set to match the voltage-clamp data of Bayliss et al. [63] for neonatal HMs. All of these parameters are listed in Table 2.

2.3 Results

The model is used to investigate the contribution of each current in generating the HM action potential by simulating pharmacological experiments and performing

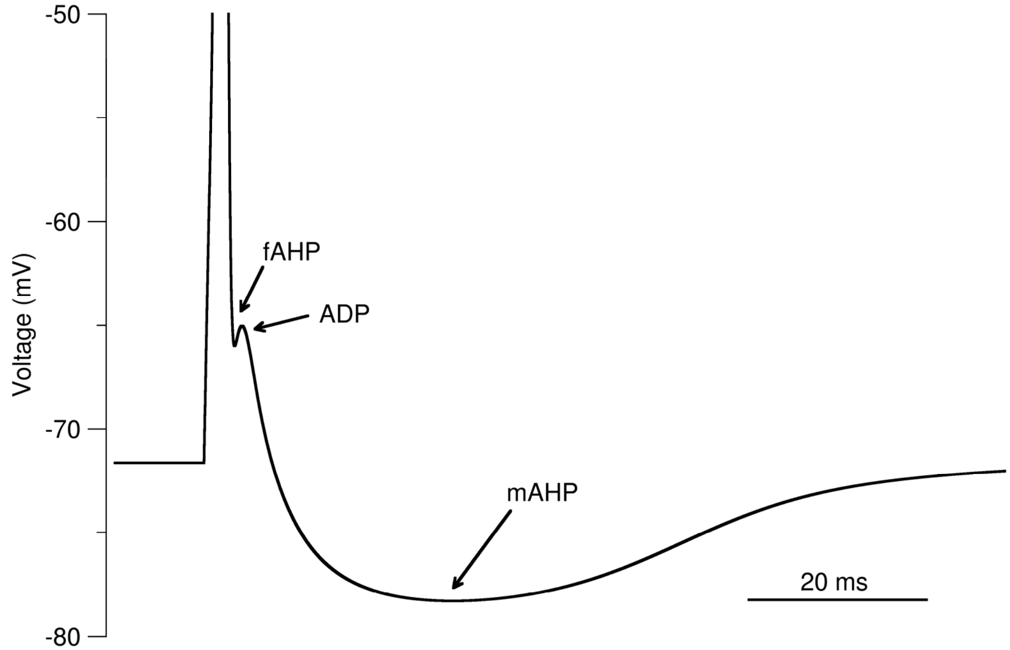

Figure 5. HM model action potential. Simulation results of the membrane potential during an action potential showing the afterpotentials seen in a neonatal rat HM. The action potential is evoked by a brief (1 ms) current pulse of 1 nA. The action potential is truncated to emphasize the fAHP, ADP, and mAHP following the spike.

sensitivity analysis. The firing properties and age-dependent changes exhibited by HMs are also explored.

2.3.1 Action Potential

A typical action potential produced by the model is illustrated in Figure 5. The action potential is elicited by a 1 ms depolarizing current pulse of 1 nA. Following the standard fast depolarization and repolarization, HM action potentials display three additional features: a fast after-hyperpolarization (fAHP), an after-depolarization (ADP), and a medium-duration after-hyperpolarization (mAHP). HMs do not fire spontaneously, and thus require a stimulus current to elicit an action potential. The stimulus current causes a sudden activation of the sodium currents, which leads to the rapid depolarization of the action potential. The repolarization is caused by a combination of sodium current inactivation, activation of the delayed rectifier, I_K, and activation of the fast transient potassium current, I_A. If the sodium currents are removed from the model, no action potential is generated. Removing I_K from the model extends the duration of the action potential from 1.4 ms to about 4 ms. If I_A is removed, the action potential duration is increased by about 0.5 ms and the resting potential is increased. Removing I_A also allows burst firing in the model, like that seen in some very young HMs [57]. These four currents, in combination with the slower activation of the calcium currents, cause the fAHP. A plot of the behavior of I_{Na}, I_{NaP}, I_K, I_A, and I_{leak} during an action potential is illustrated in Figure 6A,C. Because the conductance of I_H does not vary significantly over a single action potential, the voltage trace of I_H is similar in shape to I_{leak} during a single action potential and is not included in this figure. During repetitive firing, however, the magnitude of I_H does vary from spike to spike.

During the action potential, calcium currents become activated by the large depolarization produced by the sodium current, Figure 6B. These inward currents cause a large influx of calcium and depolarize the membrane after the cell has repolarized, which leads to the ADP. This ADP is both voltage and calcium dependent. Experiments have revealed that the amplitude of the ADP increases by elevating external calcium, after barium application, and by stepping from potentials hyperpolarized to the resting potential [57]. The model shows an increase in ADP amplitude by increasing the density

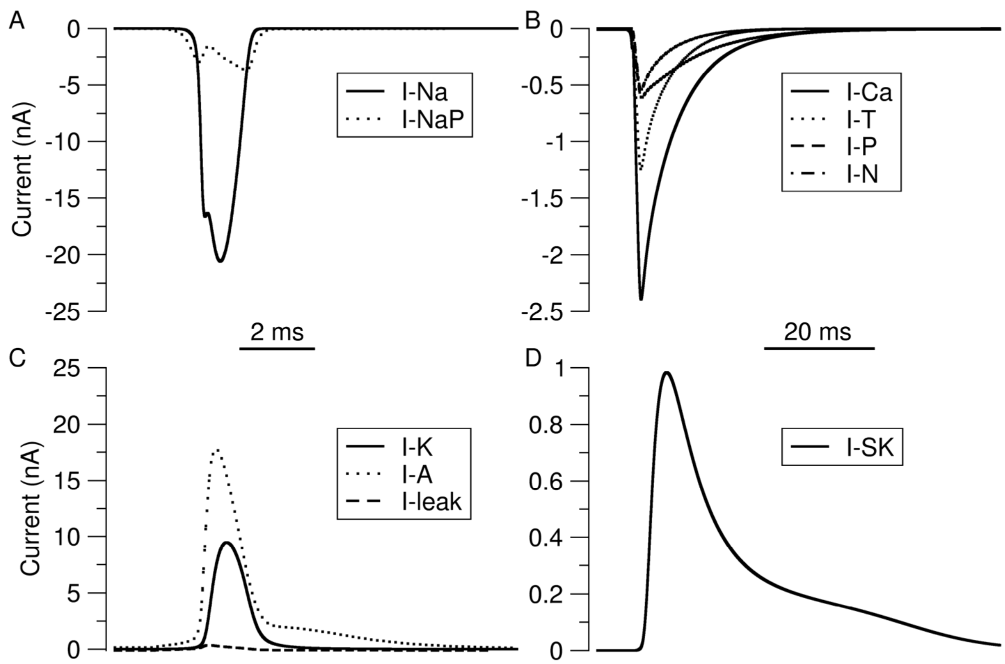

Figure 6. Model currents during an action potential. The currents active during the action potential shown in Figure 5. A 2 ms time scale is used in A and C, and a 20 ms time scale is used in B and D. A: Na and NaP currents are active during the first 2 ms of the action potential. B: The calcium currents are active during the first 20 ms of the action potential. I-Ca is the sum of the three calcium currents. C: The K, A, and leak currents are outward currents active during the first 2 ms. D: The SK current activates after the calcium currents and stays on throughout the remainder of the mAHP.

of calcium channels. For example, increasing $\bar{g}_T$ by 50% increases the ADP amplitude by 1.8 mV (Figure 7A). The model also exhibits an increase in ADP amplitude when stepping from hyperpolarized potentials. In Figure 7B, a prepulse current of 0, -0.1, and –0.2 nA was applied before eliciting an action potential. The increase in ADP height is caused by removal of inactivation of I_T and I_N.

The mAHP is due to the calcium-dependent potassium current, I_{SK}. The buildup of internal calcium caused by the inward calcium currents activated during the action

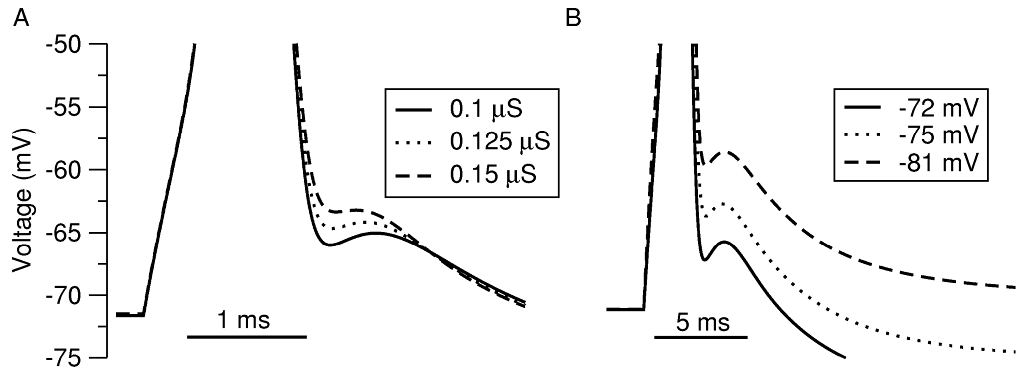

Figure 7. After-depolarization (ADP). A: The dependence of the ADP on the LVA calcium current, I_T. A 50% increase in $\overline{g}_T$ results in a 1.8 mV increase in the height of the ADP. B: The voltage dependence of the ADP. Holding potentials of -72, -75, and -78 mV produced by hyperpolarizing pre-pulses of 0, -0.1, and -0.2 nA, respectively. Voltage traces are superimposed and truncated to show the increase in ADP amplitude from baseline membrane potential.

potential activates the outward SK current, Figure 6D. The SK current in the model does not show inactivation, so it remains activated until the internal calcium concentration is decreased. Therefore, the time-course of decay for I_{SK} is determined by the depletion rate of calcium from the cell. The depletion rate is modeled in the calcium equation with the decay rate set to match the experimentally measured time course of the mAHP.

2.3.2 Apamin Simulation

The importance of the SK current in producing the mAHP is clearly identified by apamin, which selectively blocks SK channels [82]. Viana et al. [58] show that apamin reduces the peak amplitude of the mAHP by 90% in HMs, while having no effect on HM passive properties, the depolarizing phase of the action potential, or the time course of repolarization. Lape and Nistri [61] also report a complete block of the mAHP in HMs upon application of apamin. The model's response to apamin is simulated by setting the

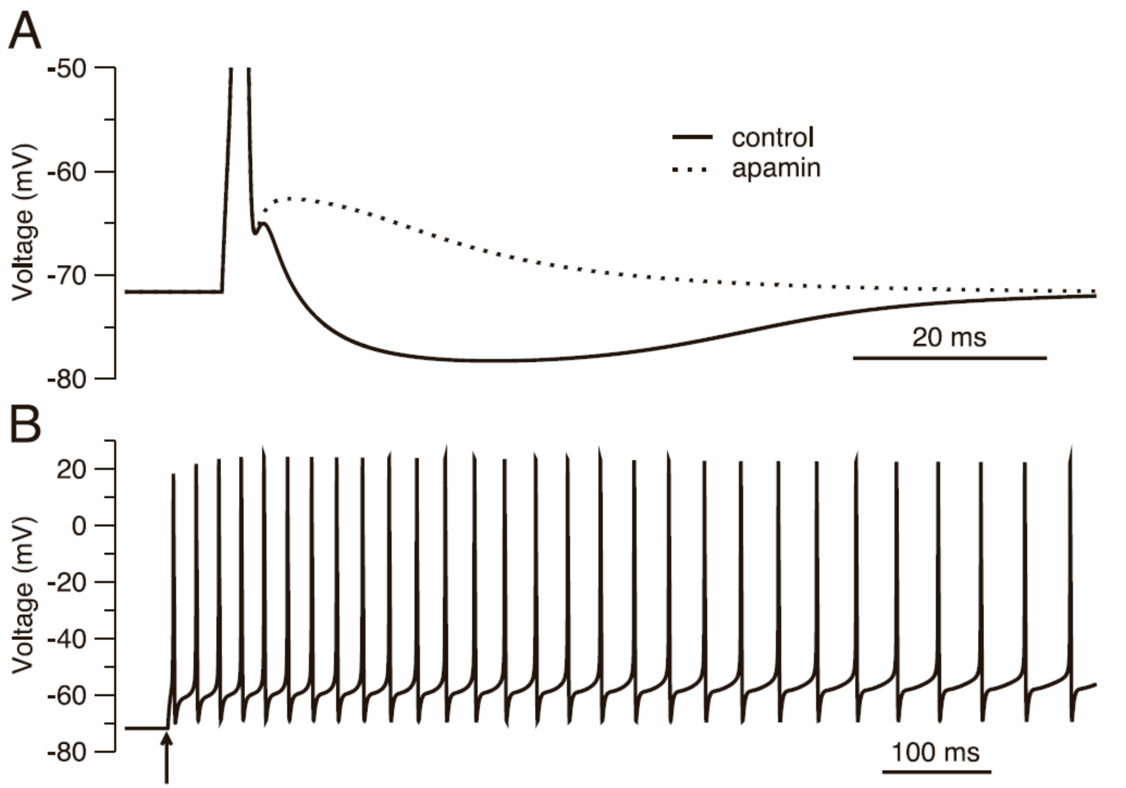

Figure 8. Apamin simulation. The effects of apamin are simulated by reducing the maximum conductance of the SK current. A: The response of the model to a 1 ms current pulse stimulus, $\overline{g}_{SK} = 0$ μS. The ADP is enhanced and the mAHP is removed. B: The response of the model to an extended current pulse with a reduced amplitude ($I_{stim} = 0.33$ nA), $\overline{g}_{SK} = 0.03$ μS. The arrow indicates stimulus onset.

maximum conductance of I_{SK} to zero ($\overline{g}_{SK} = 0$), effectively removing the current from the model. Figure 8A illustrates the result of this simulated experiment where a single action potential is elicited by a brief pulse of current. With $\overline{g}_{SK} = 0$, the mAHP's dependence on the SK current in the model is clearly seen. As reported [58], the mAHP is blocked without affecting the passive properties or the depolarizing/repolarizing phase of the action potential. There is also an increase in ADP height, consistent with experimental findings [58, 61].

Experiments have shown that the HM's response to a step of current after application of apamin is marked by spike frequency adaptation and a large increase in firing frequency [58, 61]. These features are reproduced by the model. Figure 8B is the model's response to a step of current with $\overline{g}_{SK}$ = 0.03 μS. Using a reduced stimulus amplitude of 0.33 nA, the firing frequency decreases from an initial rate of 48Hz to 22Hz after one second, and eventually stops firing altogether. The decrease in firing frequency seen here is caused by the slow inactivation of I_{NaP}. Without I_{NaP}, the firing frequency shows an initial increase (due to I_A) and quickly reaches a steady-state (not shown). Also, if $\overline{g}_{SK}$ is removed completely (i.e. $\overline{g}_{SK}$ = 0), the model does not show the initial spike frequency adaptation (see Section 2.4.1).

2.3.3 Sensitivity Analysis

Pharmacological studies, such as the apamin experiment to block the mAHP, have provided insights into which currents are affecting each feature of the HM action potential. Other examples include using TEA or 4-AP to increase action potential duration, using TTX to remove the action potential altogether, or replacing external calcium with barium and measuring its affects on the ADP. For the HM model, we sought a measure of the relative contribution of each current to features of the action potential waveform. Specifically, we wish to know how sensitive the voltage trajectory during the action potential is to the maximum conductance of each current in the model at a certain time. A mathematical technique that provides this measure is called sensitivity analysis [79]. Sensitivity analysis is used to measure the sensitivity of any state in a system, or model, to any parameter of that model. The state that we are most interested in here is the membrane voltage. Since it is our hypothesis that the distinct features of the action potential waveform are caused by the densities of intrinsic currents in the model, the parameters that we are most interested in are the maximum conductances for each current. A similar analysis was performed on a model of a human atrial cell [78].

As discussed in APPENDIX B, the sensitivity is found by computing the partial derivative of a state variable (in our case, membrane voltage) with respect to the model parameter of interest (maximum conductance). It is therefore a measure of how much a change in maximum conductance affects the voltage. We actually plot normalized sensitivities, which are found by multiplying each calculated sensitivity by the nominal value of the maximum conductance, defined as:

$$\varepsilon_k = \bar{g}_k \frac{\partial V}{\partial \bar{g}_k}$$

The sensitivity variables are integrated in parallel with the differential equations of the model. Of particular interest to us is the sensitivity function with the maximum amplitude at each point in time. This indicates which current has the largest affect on the voltage at that time, and consequently is most responsible for each feature of the HM action potential in the model. The results of the sensitivity analysis are illustrated in Figure 9. For clarity, Figure 9 is broken up into four panels. Figure 9A is an action potential generated by the model. Figure 9B plots the sensitivities for the Na, NaP, and K currents. These have the largest amplitudes during the sudden depolarization (Na, NaP) and repolarization (Na, NaP, and K) of the AP. Figure 9C provides the sensitivity functions for the A, H, and Leak currents. The membrane voltage is most sensitive to the A and Leak currents at rest, and to a lesser extent the H current. The A current also promotes AP repolarization. Figure 9D plots the sensitivities for the calcium currents and the SK current. The sensitivity of the calcium currents becomes largest after the action

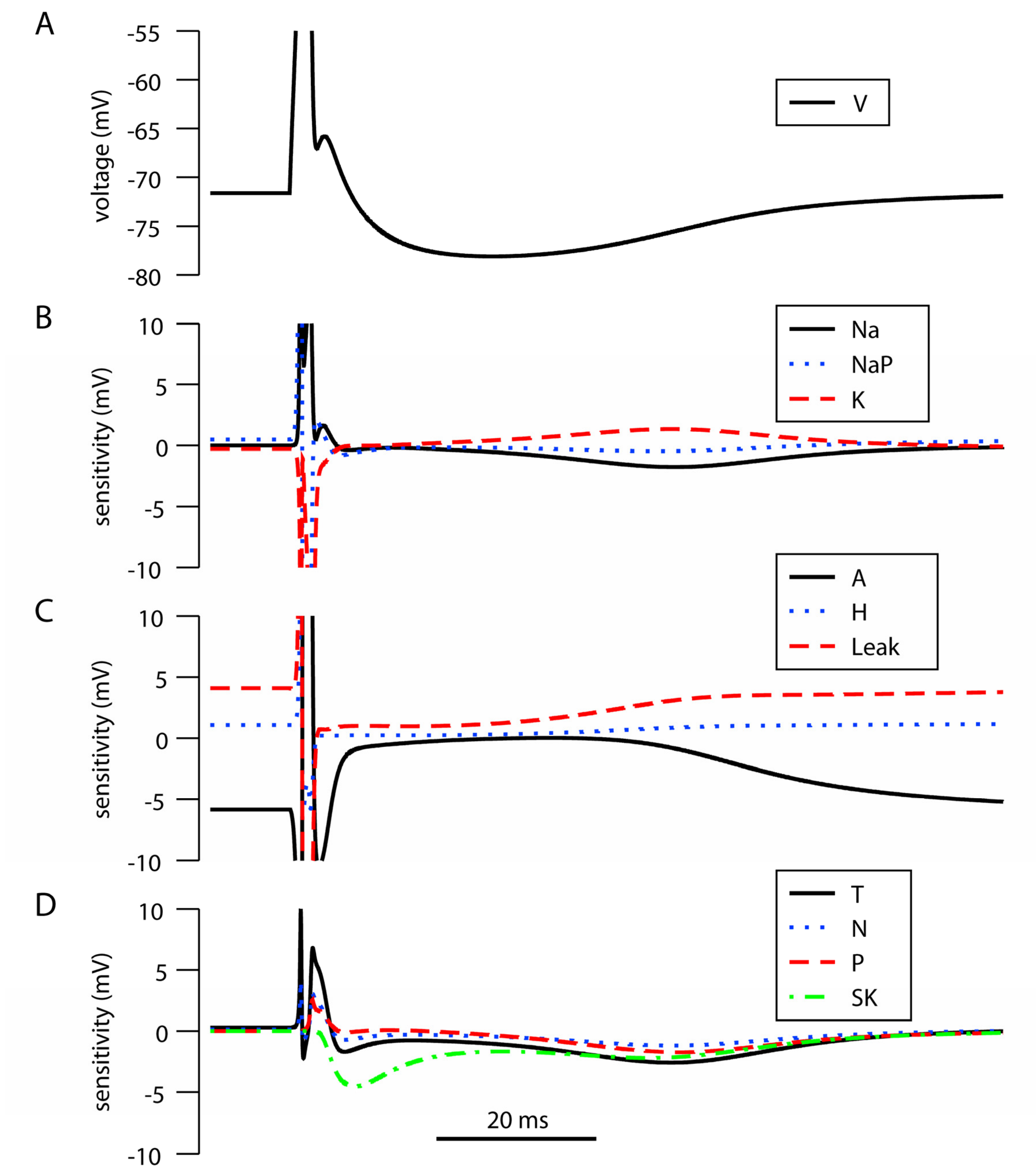

Figure 9. Sensitivity analysis of maximal conductances with respect to voltage. The sensitivities plotted are the relative sensitivities found by multiplying the sensitivity function by the maximum conductance of each current. All sensitivity functions are truncated at +/- 10 mV. **A**: The membrane potential during an action potential. The action potential and stimulus current are the same as Figure 5. Sensitivity functions are plotted for: Na, NaP, K, (**B**) A, H, Leak (**C**) T, N, P, and SK (**D**).

potential has begun to repolarize, just before and during the ADP. The most pronounced sensitivity function at the onset of the mAHP is that of the SK current, Figure 9D.

To further explore what can be learned from this sensitivity analysis, we will focus on the sensitivity of the membrane voltage to the maximum conductance of the P current (I_P; Figure 10A). The peak of the ADP occurs near t = 14.4 ms. At this time, the relative sensitivity of the voltage to the P current is measured to be 1.246 mV, i.e. a 100% increase in $\bar{g}_P$ will lead to a corresponding voltage increase of 1.246 mV. Because this analysis is a linear approximation and the results will only hold over a range about the nominal parameter values, we will only vary $\bar{g}_P$ by 20%. If we increase $\bar{g}_P$ by 20% (from 0.05 mS to 0.06 mS), the sensitivity analysis predicts that there will be a corresponding increase in voltage of 0.249 mV (1.246 mV * 20%) at t = 14.4 ms. The ADP of the model before and after the increase in $\bar{g}_P$ is illustrated in Figure 10B. The measured value of the membrane voltage at t = 14.4 ms is 0.246 mV larger after increasing $\bar{g}_P$. Figure 10B also illustrates the predicted voltage waveform during the ADP for maximum conductance increases of 20% and 50%. For the P current, the predicted waveforms closely match the actual waveforms during the ADP for both 20% and 50%.

The sensitivities of the calcium currents reverse sign during the mAHP. If the relative sensitivity function is negative, that means that a positive change in a parameter will result in a negative change in membrane voltage. During the mAHP, an increase in calcium current has a hyperpolarizing affect on the membrane voltage. This is seen with the P current in Figure 10C. Typically an increase in an inward current will have a depolarizing effect on membrane potential. Here, an increase in the inward calcium

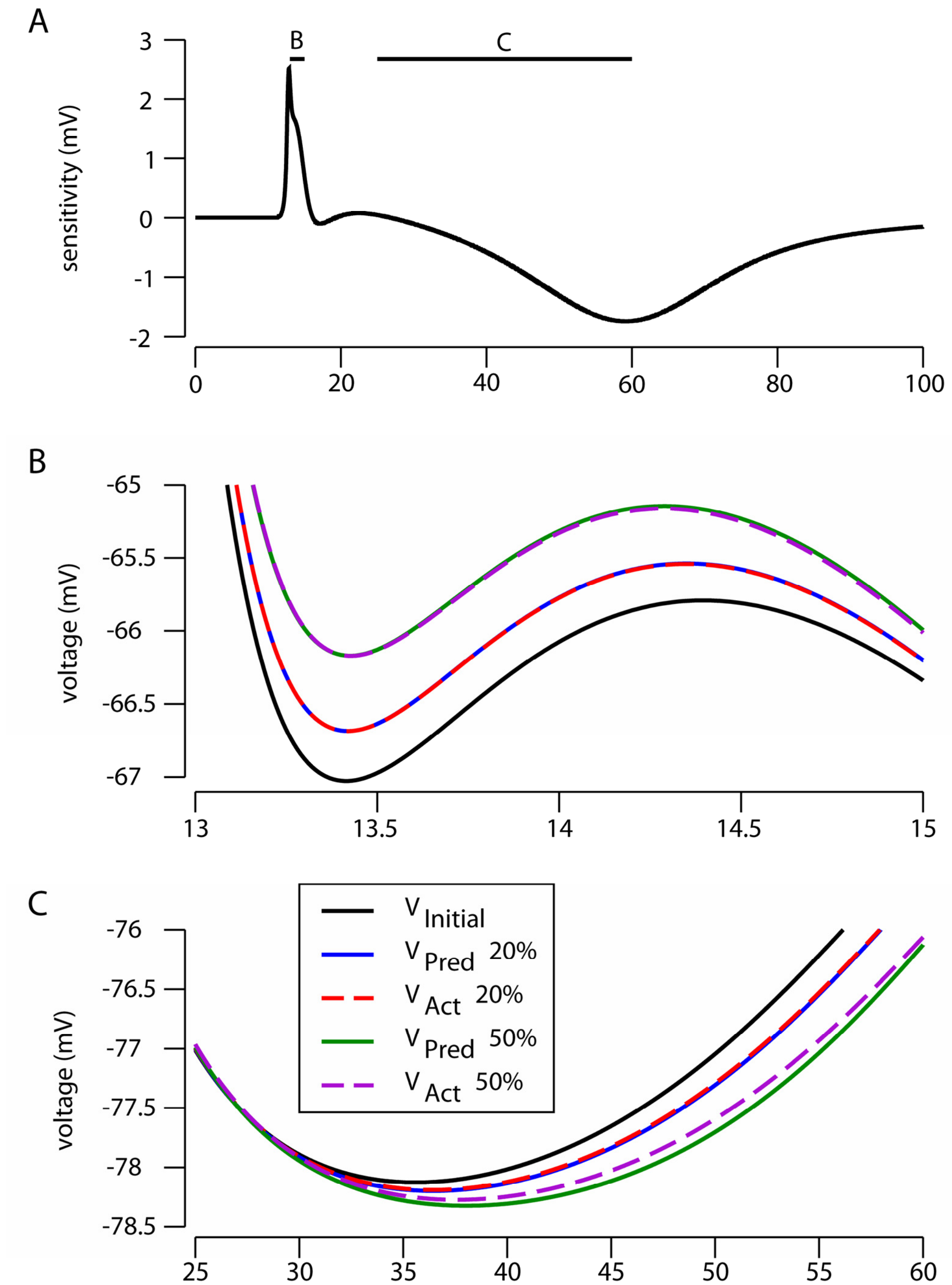

Figure 10. Sensitivity analysis for the P current. $\overline{g}_P$ is increased by 20% and 50%. The change in membrane voltage during the ADP (**B**) and mAHP (**C**) is plotted for both the predicted and actual waveforms. **A**: The relative sensitivity for the P current (see also Figure 9D). **B**: Membrane potential is increased during the ADP. **C**: Membrane potential is decreased during the mAHP.

current hyperpolarizes the membrane potential via the (outward) calcium-dependent potassium current. The sensitivity analysis predicts this behavior (Figure 10C).

In general, this method provides good results for maximum conductance variations of 20%. However, the predictions when using a 50% increase are not as good for some currents. For example, if the maximum conductance of the A current is increased by 50%, the model fails to fire an AP even though the sensitivity analysis predicts that an action potential will occur. Interestingly, the predicted waveform does possess a large hyperpolarizing dip in membrane potential at the start of the AP. The prediction of a large hyperpolarization could lead the modeler to conclude that the model will be incapable of firing an AP when the maximum conductance of A current is increased by 50%.

2.3.4 Firing Properties

2.3.4.1 Near Threshold

When the stimulus is near the threshold for firing, some HMs display two features that can be reproduced by the model (Figure 11). The first feature is spike frequency adaptation leading to a cessation of firing after several spikes (Figure 11A). The number of spikes before cessation is determined by the stimulus amplitude. A slightly smaller (or larger) stimulus amplitude will cause fewer (or more) spikes before ceasing. The persistent sodium current's contribution to spike frequency adaptation and AP generation can be seen here. It is the decrease in I_{NaP} amplitude due to slow inactivation that slows down the firing rate and leads to cessation of firing. If I_{NaP} is removed from the model, there is no near-threshold stimulus amplitude that will show adaptation or lead to a cessation of firing once firing has been initiated. The second feature reproduced by the

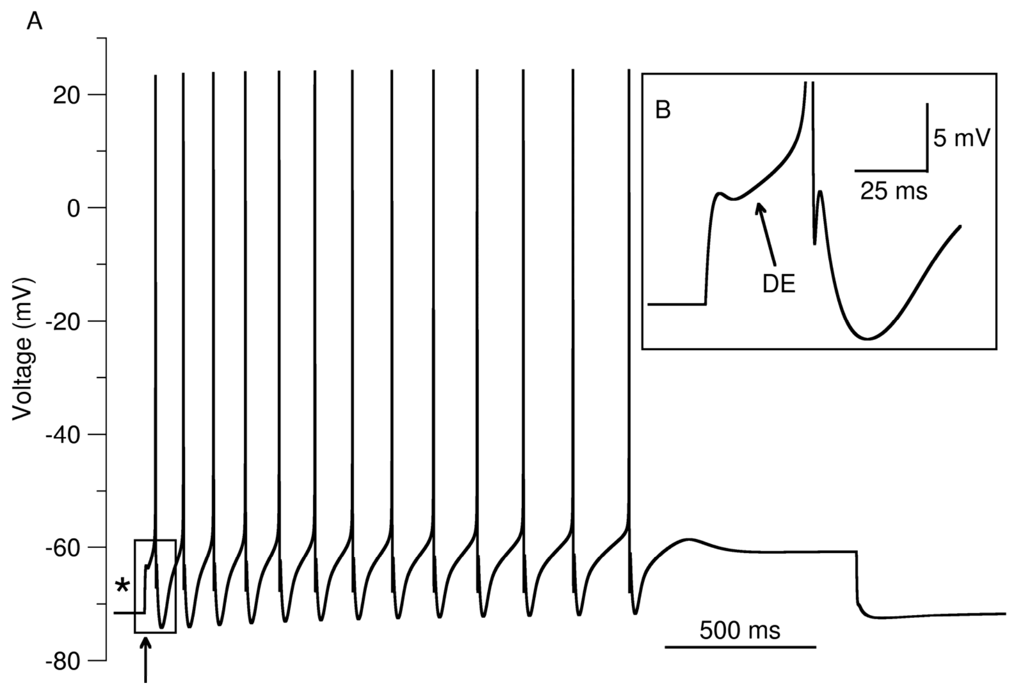

Figure 11. Near threshold firing. The response of the model to a stimulus amplitude near the threshold for firing action potentials, I_{stim} = 0.22 nA. A: The model shows spike frequency adaptation followed by a cessation of firing. B: Inset is * in A showing delayed excitation (DE) of the first spike. The arrow indicates stimulus onset.

model is delayed excitation (DE). DE is a common phenomenon caused by I_A where the onset of the first spike is delayed due to the large initial potassium current (Figure 11B). A small amount of DE can be seen in HM recordings [58, 61].

2.3.4.2 Adaptation

When using a stimulus amplitude above threshold, the repetitive firing behavior of neonatal HMs undergoes significant changes during postnatal development. Neonatal HMs show both spike frequency adaptation and acceleration. 79% of HMs at ages P0-3 show adaptation, and 79% of HMs at ages P8-15 show acceleration [65]. For adult HMs,

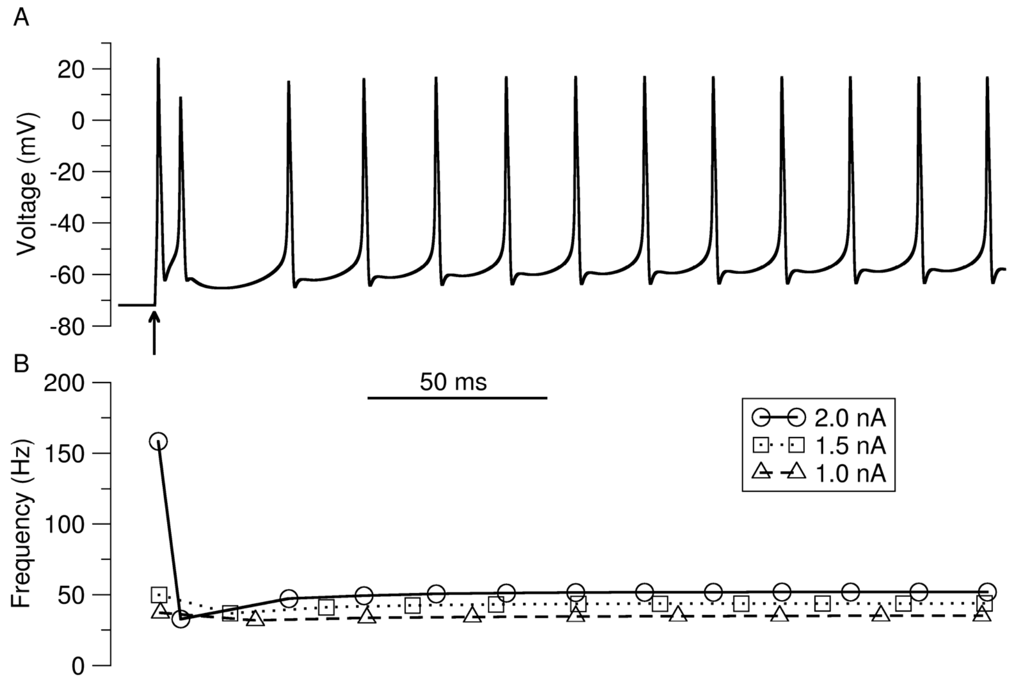

Figure 12. Spike frequency adaptation. The stimulus current is a 250 ms step of current. A: A train of action potentials generated by a 2.0 nA stimulus current. B: Frequency-time measurements. The amount of adaptation increases with an increase in stimulus current amplitude. Adaptation occurs during the first two inter-spike intervals. The arrow indicates stimulus onset.

the pattern reverts back to adaptation with 79% of HMs again showing adaptation [65]. The model is capable of generating spike trains that show both adaptation and acceleration, depending on conductance parameters. Figure 12 illustrates the model's response to a 200 ms step of current. Figure 12A is a typical train of model generated action potentials undergoing spike frequency adaptation. A small amount of adaptation occurs during the first few spikes, and then a steady-state firing frequency is obtained. Figure 12B is a plot of frequency vs. time for three different input currents. As the amplitude of the stimulus current is increased, the amount of adaptation increases greatly while the duration of the adaptation (number of spikes occurring before reaching steady state) remains short. This response is similar to that seen in Viana et al. [65] for the majority of P0-3 HMs. In HMs that show adaptation, the AHP following the first spike is more depolarized than succeeding AHPs [65]. The model reproduces this behavior. The initial adaptation is caused by the summation of the SK current, similar to that modeled by Powers et al. [68]. Experimental results show that the initial adaptation is, at least in part, controlled by the SK current [62].

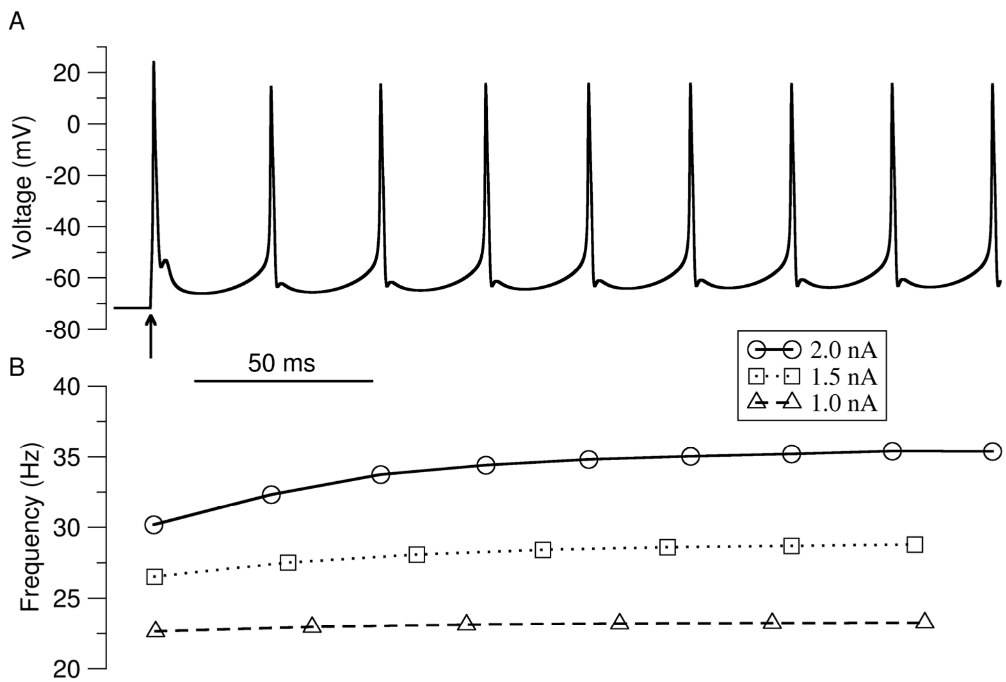

Figure 13. Spike frequency acceleration. The T current is increased by 10-fold (see Figure 14) from that shown in Figure 12. The stimulus current is a 250 ms long step of current. A: A train of action potentials generated by a 2.0 nA stimulus current. B: Frequency-time measurements. The amount of acceleration increases with an increase in stimulus current amplitude. Acceleration occurs during the first few inter-spike intervals. The arrow indicates stimulus onset.

2.3.4.3 Acceleration

By changing $\overline{g}_T$ or $\overline{g}_N$ (see below), the model's response to a step of current is transformed from adaptation to acceleration. Figure 13A is a typical train of model generated action potentials undergoing spike frequency acceleration. As with the case of adaptation, acceleration occurs during the first few spikes. Figure 13B is a plot of frequency versus time and reveals that the amount of acceleration increases with an increase in stimulus current amplitude. This simulation is similar to the behavior seen in Viana et al. [65] for the majority of P8-15 HMs. In contrast to the positive AHP summation seen in adaptation, accelerating HMs show a negative AHP summation [65]. In the model, the first AHP is more hyperpolarized than succeeding AHPs. The cause of the initial acceleration is addressed in Section 2.4.3.

2.3.5 Age-Dependent Changes

2.3.5.1 Adaptation vs. Acceleration

To identify a possible mechanism that explains the variation in firing characteristics during postnatal development, we considered two relevant experimental results. First, the calcium-dependent potassium current, I_{SK}, plays an important role in the frequency control of HMs [58, 61, 62]. Second, experiments have shown that the contribution of the T current to the total calcium current changes during neonatal development [59]. Because I_T affects I_{SK} through the buildup of internal calcium concentrations, and I_{SK} affects firing frequency, we hypothesized that the change in density of I_T plays a role in the age-dependent firing properties of HMs. To test this hypothesis, we varied the density of T channels in the model by varying $\overline{g}_T$ over a ten-fold range and measured changes of the first two interspike intervals (ISIs). The ISIs are

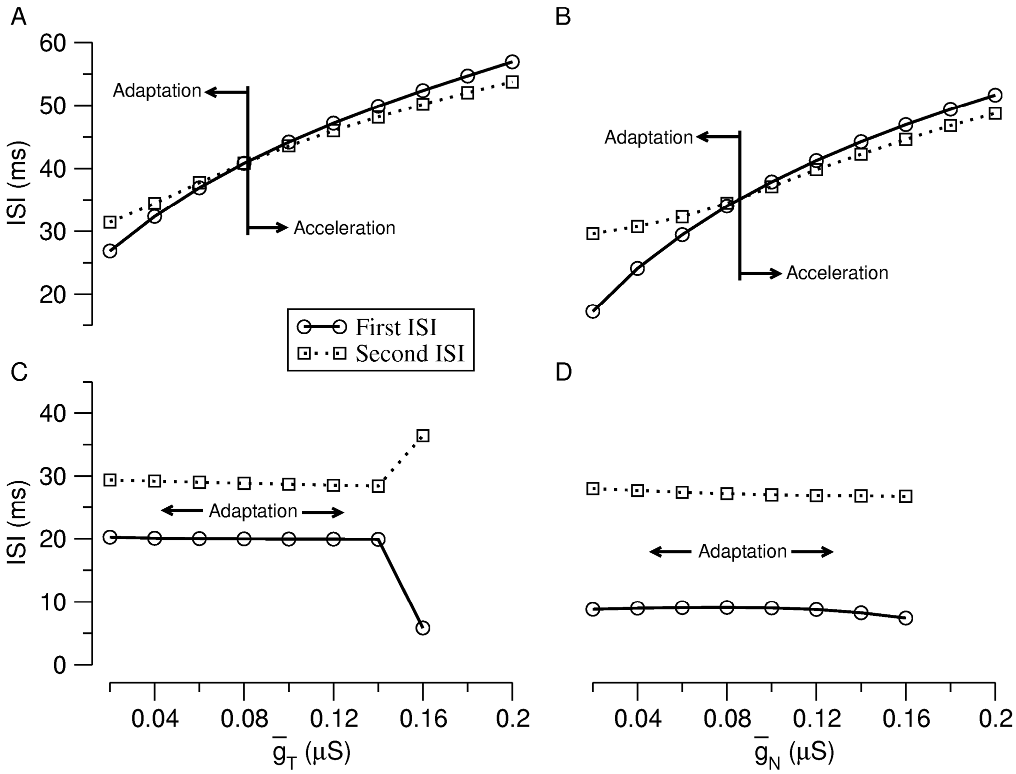

Figure 14. Adaptation vs. acceleration. The effect of varying the T and N current densities on firing behavior. ISI is measured from the peak of one spike to the peak of the next spike. If the first ISI is smaller than the second ISI, adaptation occurs. If the first ISI is larger than the second ISI, acceleration occurs. A and B: $I_{Ca} = I_P + I_N + I_T$. Increasing $\overline{g}_T$ (A) or $\overline{g}_N$ (B) changes the firing behavior from adaptation to acceleration. C: $I_{Ca} = I_P + I_N$. Adaptation is seen for all values of $\overline{g}_T$. D: $I_{Ca} = I_P + I_T$. Adaptation is seen for all values of $\overline{g}_N$. $\overline{g}_T$ is reduced to 0.02 µS for B and D.

measured from the peak of one spike to the peak of the following spike. Because adaptation (or acceleration) occurs during the first three spikes, only the first and second ISIs are considered. Figure 14A illustrates the effect of varying $\overline{g}_T$ on the first two ISIs. At low values of $\overline{g}_T$, the first ISI is smaller than the second ISI (i.e. the frequency decreases with time, or adaptation). An increase in $\overline{g}_T$ increases the duration of the first ISI at a rate greater than that of the second ISI. At large values of $\overline{g}_T$, this leads to the first ISI being greater than the second ISI (i.e. the frequency increases with time, or acceleration). Where the two curves meet, the first ISI is equal to the second ISI and there is no change in frequency over time. This constant firing rate is also a feature seen in neonatal HMs [65]. Since blocking the N current can eliminate the mAHP [58], we also varied the density of the N current and measured its affects on the first two ISIs. The results of varying $\overline{g}_N$ are similar to those of $\overline{g}_T$ (Figure 14B).

Another model experiment was performed to elucidate whether the change in density of I_T affects the firing rate specifically through its influence on I_{SK} via the calcium equation (see Section 2.1.2). For Figure 14C, the calcium equation was modified to exclude the contribution from I_T ($I_{Ca} = I_P + I_N$), and $\overline{g}_T$ was again varied while measuring the first two ISIs. When I_T is removed from the calcium equation, the first ISI is always smaller than the second ISI (adaptation), regardless of the value of $\overline{g}_T$. In fact, increasing $\overline{g}_T$ has almost no affect on the initial firing rate until $\overline{g}_T$ reaches 0.16 μS. Here, the increased depolarization due to I_T allows the sodium current to initiate a second spike immediately following the repolarization of the first spike (the second spike proceeds from the ADP of the first spike). This same model experiment was performed for the N current ($I_{Ca} = I_P + I_T$, Figure 14D). Again, adaptation was seen for all values.

2.3.5.2 mAHP Duration and the H current

Along with changes in firing properties, other changes accompany the HMs transition from neonatal to adulthood. These changes include a decrease in the duration of the mAHP, and a large increase in the density of I_H [53, 63, 64]. Bayliss et al. [63] reports that the density of H-channels increases by a factor of 10 from neonatal rats to adult rats. Therefore, we increased $\overline{g}_H$ and measured its effects on the model. The most

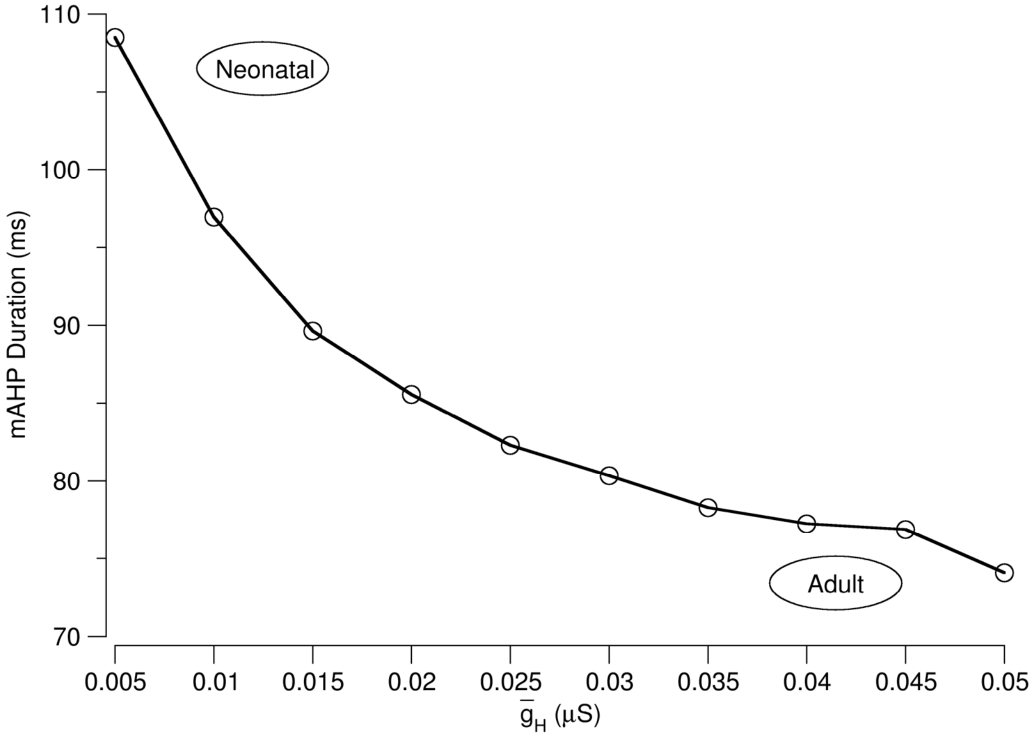

Figure 15. H current vs. mAHP duration. The effect of varying H current density on mAHP duration. A 10-fold increase in $\bar{g}_H$ decreases the mAHP duration from that of neonatal HMs (~110 ms) to that of adult HMs (~75 ms).

significant effect was seen on the duration of the mAHP (measured from the repolarizing phase of the action potential to the point in the AHP that reaches the resting potential). Neonatal HMs have a mAHP duration of 110 ms, and adult HMs have a mAHP duration of 75 ms [64]. Figure 15 is a plot of mAHP duration vs. $\bar{g}_H$. The original model is of a neonatal HM and consequently has an mAHP duration of 109 ms. Increasing $\bar{g}_H$ by a factor of 10 shortens the mAHP duration to 77 ms in the model, which is very similar to what is seen in the data [64]. This model experiment indicates that the change in the density of the H current in the data can potentially completely account for the change in mAHP duration in the data. Thus, our model supports this contribution of the H current suggested by Bayliss et al. [63].

2.3.5.3 Input Resistance and AP Duration

Other changes that occur from neonatal to adulthood are a decrease in R_N, and a decrease in action potential duration [64]. It has been suggested that the increase in H current density may be enough to account for the decrease seen in R_N [63]. However, in the model, a ten-fold increase in $\overline{g}_H$ only decreases R_N by 5 MΩ. The model requires a simultaneous increase of the maximum conductance of other currents active at rest, such as the A and K currents, to obtain the 20 MΩ decrease in R_N seen in the data [64]. Increasing these maximum conductances also causes a shortening of the action potential duration. With the nominal parameters for the neonatal HM model, the action potential duration is 1.4 ms and R_N is 40 MΩ. Following the 10-fold increase in H current density and a 100% increase in the maximum conductances of I_K and I_A, the action potential duration is 1.0 ms and R_N is 20MΩ. The 0.4 ms difference in AP duration and the 20 MΩ difference in R_N between neonatal and adult are consistent with experimental findings in HMs [64].

2.4 Discussion

Powers [83] developed a variable-threshold model of a cat alpha-motoneuron that was able to account for several motoneuron behaviors. That model is a simplified motoneuron model and is well suited for large networks. Powers et al. [68] also developed other simplified motoneuron models to explore the three phases of adaptation seen in adult HMs [84]. Our model is more complex, and is derived mostly from data taken from neonatal HMs. The model is able to reproduce the fine details of a HM action potential including the fAHP, the ADP, and the mAHP. The model reproduces both types of firing behavior observed in neonatal HMs: adaptation and acceleration. We proposed possible explanations for the age-dependent differences in firing properties, mAHP duration, resting R_N, and action potential duration.

2.4.1 Apamin Simulation

The model faithfully reproduces the response to a brief pulse of current when the SK current is removed. As in the experimental results, the passive properties and the depolarizing/repolarizing phase of the action potential are unchanged. This is accompanied by an enhancement of the ADP and the absence of the mAHP. Here, the critical role of the SK current in generating the mAHP can be clearly seen. The importance of I_{SK} for repetitive firing is revealed when the brief pulse of current is lengthened to a longer step of current. Reducing $\overline{g}_{SK}$ from 0.3 μS to 0.03 μS leads to a large increase in firing frequency accompanied with spike frequency adaptation. A similar response is obtained by reducing the total calcium current in the model to zero (not shown). Under either of these conditions, the HM model is able to display calcium-independent spike frequency adaptation, which has been shown to occur experimentally [58, 61, 62]. In the model, this adaptation is caused by the slow inactivation of I_{NaP}. However, under normal conditions, calcium and calcium-sensitive currents dominate the firing behavior of the model.

For the simulation in Figure 8B, $\overline{g}_{SK}$ was reduced to 0.03 μS and not 0 μS. When I_{SK} is completely removed ($\overline{g}_{SK}$ = 0), the model does not display the initial spike frequency adaptation. Instead, the model displays acceleration caused by inactivation of the A current. This contradicts the role of the A current suggested by Lape and Nistri [55] where they propose that the A current causes adaptation in HMs. The acceleration occurs regardless of whether the model parameters (prior to reduction of $\overline{g}_{SK}$ due to apamin) are set to produce adaptation, as in Figure 12, or acceleration, as in Figure 13. As discussed in Section 2.2.2, our implementation of the A current is simpler than the description given by Lape and Nistri [55]. Alternatively, a multi-compartment model similar to that of Booth and Rinzel [85] that physically separates the fast and slow currents may provide a more robust response.

2.4.2 Sensitivity Analysis

We used sensitivity analysis to provide a measure that allows us to state with certainty which currents are causing each feature of the HM action potential in our model (Figure 9). The large half-activation voltages for the calcium currents and the SK current's calcium dependence result in small sensitivity functions for these currents at rest. It is the A, leak, and H currents that have the largest sensitivities at rest, and therefore function to set the resting potential and R_N of the cell in the model. As expected, the Na, NaP, K, and A currents have the largest relative sensitivity functions during the depolarizing and repolarizing phase of the action potential. It is after the repolarization phase of the action potential and just before the ADP that the calcium currents activate and become the currents to which the membrane voltage is most sensitive. The sensitivity of the membrane voltage to the calcium currents allows the calcium currents to depolarize the cell and gives rise to the ADP. The increase in the intracellular calcium concentration activates the SK current. The SK current's sensitivity function then dominates the other sensitivity functions and therefore dictates the membrane potential's trajectory. This occurs just before and during the time that the HM action potential displays the mAHP. The results match up well with experimental observations concerning the currents that cause the depolarization and repolarization of the action potential, the fAHP, ADP, and mAHP (reviewed in [20]).

We then used sensitivity analysis to predict the effect on membrane potential of increasing the maximum conductance of the P current, $\overline{g}_P$ (Figure 10). We found that increasing $\overline{g}_P$ has a depolarizing effect on the membrane potential during the ADP, and a hyperpolarizing effect on membrane potential during the mAHP. It may be counter-intuitive that an increase in an inward current could have a hyperpolarizing effect on membrane potential. However, the increase in $\overline{g}_P$ causes more Ca^{2+} to flow into the cell, which allows for greater activation of the calcium-dependent potassium current, I_{SK}. After some delay, I_{SK} hyperpolarizes the cell. The other two calcium currents in the model display comparable depolarizing and hyperpolarizing behavior during the ADP and mAHP, respectively. A similar analysis can be performed on all other currents in the model to determine their effect on membrane voltage at specific times during the action potential.

2.4.3 Age-Dependent Changes

The model provides a possible explanation for the change in repetitive firing properties observed during development. If I_T or I_N is included in the calcium equation, then increasing the density of that current in the model changes the firing properties from adaptation to acceleration (Figure 14A,B). When the current density is low, the SK current is only partially activated during the first spike. The level of internal calcium increases during the second spike and causes summation of the SK current, which produces adaptation. When the T or N current density is large, the SK current is almost completely activated during the first spike. Because both the T and N currents quickly inactivate after the first spike, much less calcium enters the cell through those channels during subsequent spikes. This causes the level of internal calcium to reach its maximum during the first spike. As the level of internal calcium decreases, the activation of the SK current also decreases. The smaller SK current allows subsequent spikes to occur sooner (i.e. acceleration). This phenomenon is dynamic, and not merely a byproduct of increasing the overall level of calcium entering the cell. If the density of the P current (a slowly activating and non-inactivating calcium current) is increased, the model continues to show adaptation.

Experiments show that the density of the current resistant to the three HVA current antagonists (considered to be the T current) decreases during postnatal development. The decrease seen experimentally in T current density is measured between days 3 and 4 postnatal [59]. Experiments have shown that the majority of HMs show spike frequency adaptation during the first week postnatal, and acceleration during the second week [65]. Reducing the T current in the model changes the firing characteristics from acceleration to adaptation. If experiments confirm that the T current continues to monotonically decrease as the rat ages, then the model's results do not correlate (until the adult age). If a change in T current density as modeled is the sole cause of the change in repetitive firing properties during aging, then the T current density will have to increase during the second week postnatal and then decrease before adulthood. There have been no reports of an age-dependent change in N current density in HMs.

Figure 14 demonstrates that varying the density of a calcium current only affects the firing properties (adaptation vs. acceleration) if that calcium current has an influence on the SK current. Therefore, colocalization of calcium channels and the SK channels could play a role in determining HM firing behavior. Colocalization between specific calcium channels and calcium-dependent potassium channels has been observed in other neurons [86-88], and was proposed in HMs by Viana et al. [58]. Colocalization would allow the influx of calcium from only certain channel types to affect activation of the SK current. Thus, a current such as the L-type calcium current (not modeled) that makes up less than 10% of the total calcium current in HMs could have a large affect on the shape of the action potential. The dynamics of a single calcium channel type could control the firing properties of HMs through the SK current. If the SK channels are localized to the P or L channels at birth, and then shift their localization to the T or N channels, this will change the firing properties from adaptation to acceleration. Another possibility is that the SK channels may change from a global channel to one that is localized to a certain calcium channel type during aging, again changing the firing properties with age. To verify this, experiments to determine the existence of colocalization between the SK current and any of the calcium currents in HMs would need to be performed. Viana et al. [57] show a neuron where pharmacologically blocking N channels removes the mAHP. Though it is not stated, this neuron appears to display acceleration. This could then be tested by blocking P and/or L channels in a HM that displays adaptation.

Mammalian motoneurons experience anatomical and physiological changes during development (reviewed in [89]). Some of the age-dependent changes of neonatal rat HMs (reviewed in [90]) have been explored here. These changes include a decrease in mAHP duration, a decrease in R_N, a decrease in action potential duration, a change in repetitive firing properties, and changes in the density of different ion channels. Factors that affect the duration of the mAHP in the model include 1) the magnitude and time course of the calcium currents, 2) the SK current 3) the A current, 4) the H current, and 5) the depletion rate of calcium from the cell. We showed in Figure 15 that, in the model, the 10-fold increase in density of the H current is enough to account for the decrease in mAHP duration observed between neonatal and adult rats. However, the change in H current density is not enough to account for all of the age-dependent changes seen in HMs. According to Viana et al. [64], the resting membrane potential of HMs is the same for neonatal and adult rats. In the model, the resting membrane potential increases by approximately 5 mV as the H current density is increased. Also, increasing the density of the H current in the model can not completely account for the decrease in R_N or produce the decrease in action potential duration observed in HMs [64]. Concurrent changes in other currents are needed to account for these behaviors in the model. Cameron and Nunez-Abades [89] agree that the decrease in R_N is partly caused by a proliferation of ion channels. However, they suggest that this decrease is also caused by an increase in the number of synaptic inputs, something that is not included in our model.

Adult HMs fire at a higher rate than neonatal HMs [65]. The decrease in mAHP duration could allow for the higher firing rates observed in adult HMs. In addition to its possible role in modulating the steady-state firing rate, the H current could potentially play a role in spike frequency adaptation seen in adult HMs. In the model, the magnitude of the H current between spikes (during the mAHP) decreases over time with a time constant of approximately 300 ms during a train of action potentials. If the density of the

H current is sufficiently large, this spike to spike decrease in H current magnitude could result in an increase in mAHP duration between spikes. However, increasing $\overline{g}_H$ to 0.1 μS causes only a small amount of adaptation in the model (less than 1 Hz decrease over 1 second).

2.4.4 Limitations of the Model

2.4.4.1 Currents

The currents included in this model are only those known to exist in neonatal rat HMs (reviewed in [20]). We did not include those currents that have been observed in other motoneurons or other animal species. Currents such as the voltage- and calcium-activated potassium current (BK) and the sodium-activated potassium current (K, NA) found in other motoneurons (reviewed in [91, 92]) could also exist in neonatal rat HMs. These currents could certainly affect the model's behavior, but are not included because there is no data describing these currents in neonatal HMs. This is both a strength and a limitation of the model. A potential role of the BK current is the age- and calcium-dependent change in action potential shape during a train of action potentials observed in HMs [65]. An increase in density of a BK current, or an increase in density of a calcium current that activates a BK current, could cause this age-dependent change.

2.4.4.2 Morphology

Many motoneuron morphologies have been described previously. Some of these studies include a three-dimensional analysis of cat alpha-motoneuron morphology [93, 94] and phrenic motoneuron morphology from a neonatal rat [95]. HM morphologies have also been investigated in the cat [96], guinea-pig [97, 98] and rat [99]. The morphology of rat genioglossal motoneurons has been shown to change during postnatal development [100-102]. It is clear that morphology plays an important functional role in motoneurons (reviewed in [92]). Developmental changes in HM morphology may also partially account for the age-dependent changes in resting membrane potential and R_N. Extension of this model will be required to explain the effects of synaptic integration, including modeling dendritic structures. However, our single-compartment HM model is able to accurately reproduce several electrophysiological characteristics of HMs. In the next chapter we use an automated optimization technique to optimize the model parameters to more closely fit experimental data.

CHAPTER 3: MODEL OPTIMIZATION USING A GENETIC ALGORITHM

In the previous chapter, we developed an ionic current model of a neonatal hypoglossal motoneuron. The model was used to examine the roles of various ion channels in shaping the hypoglossal motoneuron action potential and to explore the age-dependent changes seen in those cells. In this chapter, we use an automated optimization technique to provide a closer fit to the experimental measures of action potential shape.

The quality of solutions produced by any optimization method is critically linked to the selection of the cost function, or fitness function, employed by that method. Regardless of the variation of method used, the choice of fitness function is the most important factor in determining the success of the algorithm. We use a genetic algorithm to optimize the parameters of a neonatal hypoglossal motoneuron model to fit experimental measures of a complex action potential shape. Multiple fitness functions were evaluated: 1) a template-based fitness function that compares the model output to an ideal action potential waveform, 2) a feature-based fitness function that computes the deviation from the mean of several experimental measures of the action potential, and 3) a combination of the template-based and feature-based fitness functions. We use both seeded and unseeded initial populations, and examine the final parameters of the best models. Although all parameters were allowed to vary, the best results were generated almost exclusively by changes in non-conductance parameters (such as half-activation values, time constants, etc.) as opposed to conductance parameters, which are a common target for optimization methods applied to neuron models. This result highlights the importance of including all parameters in an automated parameter search. After running multiple simulations for each type of fitness function, the feature-based fitness function alone provided the best fit to experimental data. However, if input impedance (a feature not accounted for by the template-based fitness function) is excluded from the data, the combined fitness function provides the best solution when fitting the complex action potential shape of hypoglossal motoneurons.

3.1 Methods

The following section describes the automated optimization technique used and the fitness functions compared in this study. The model and simulation details are also described.

3.1.1 Genetic Algorithm

A Genetic Algorithm (GA) is a popular, biologically inspired optimization method. The GA starts with an initial population of models with randomly chosen parameters, and proceeds by letting the population evolve using mechanisms inspired by the idea of natural selection. Each model in the population is tested for fitness and assigned a score. This fitness score is the basis for that model's likelihood of reproducing (through crossover) and retention for subsequent generations. The desire is that with each generation, characteristics (parameter values) of the best performing individuals (models) will combine to produce better individuals. Researchers have previously used GAs for parameter optimization of neurons models [69-72] and models of other excitable cell types [73].

In a GA, the model parameters to be optimized are stored in a chromosome, a string of binary values. The parameters typically used for optimization in neuron models

Table 3. Allowed ranges of maximum conductances. All other model parameters are allowed to vary +/- 10%. Ten bits were allocated to each maximum conductance.

	Current	Conductance
1	Na	0-5 μS
2	NaP	0-2 μS
3	K	0-5 μS
4	T	0-2 μS
5	P	0-2 μS
6	N	0-2 μS
7	SK	0-3 μS
8	A	0-5 μS
9	H	0-2 μS
10	Leak	0-2 μS

are the maximum conductances of each current. For all figures shown, the allowable range of maximum conductances for all currents is given in Table 3. For tuning the neuron model, this study does not limit parameter variation to maximum conductances alone. All other model parameters (e.g. half-activation values, time constants, etc.) are also allowed to vary, and these parameters, that is all parameters other than maximum conductances, are hereafter referred to as non-conductance parameters. For most of the results in this study, all non-conductance parameters in the model are allowed to vary by +/- 10% of their nominal value (i.e. the value reported in [103]). Simulations allowing large variations in all parameters were also run, and are briefly discussed in Sec. 3.2.6. Both random (unseeded) initial populations and initial populations that are biased (seeded) by including one member with the nominal parameters from Chapter 2 were investigated.

3.1.2 Fitness Functions

The experimental data that we are attempting to fit is list of experimental measures of neonatal hypoglossal motoneuron action potential (AP) and steady-state characteristics (reported as mean +/- standard error in [64]). These measures include: 1) resting membrane potential, 2) AP amplitude, 3) AP duration, 4) after-hyperpolarization (AHP) amplitude, 5) AHP duration, 6) AHP half-duration, and 7) steady-state input resistance (R_N). The characteristics of the after-depolarization exhibited by some HMs are highly variable, and are therefore not considered in this study. For this study, the quality of solutions produced by the GA is determined by how closely the model fits the seven listed measures.

3.1.2.1 Template-Based Fitness Function

Many GA and other parameter optimization studies have used a template waveform and a sum of squares error (SSE) measure in the fitness function [70, 71, 73, 104-106]. Often the template is created using a nominal model parameter set that the optimization routine is attempting to find, or the template is taken from experimental data. For this study, the experimental data that we want to fit is given as a list of AP measures. Therefore, we created a hand-drawn template AP that almost perfectly meets the criteria above and used a SSE measure as the fitness function for the GA. The score of the template-based fitness function, $Score_T$, is computed as

$$Score_T = \sum (V_{Template}[t] - V_{GA}[t])^2$$

where t is the time, $V_{template}$ is the voltage of the template AP at time t, and V_{GA} is the voltage computed by the model using parameters produced by the GA at time t.

3.1.2.2 Feature-Based Fitness Function

Next, we developed a feature-based fitness function that directly compares the output of the model to the experimental measures. Each feature was calculated as reported in Viana et al. [64] with standard error measures converted to standard deviations (SDs) for the fitness function. Additionally, since HMs are normally silent at rest, a measure was added to test whether or not the cell was silent before the stimulus current was applied. The voltage was measured for 10 ms prior to application of the stimulus and allowed an SD of 0.01 from its resting value. This measure was added to penalize the tonically firing models observed in preliminary studies. The fitness function computes these measures for each model, finds the number of standard deviations away from the experimental mean (z-score) for each measure, and then sums the absolute values of these numbers. For example, if the AP amplitude is 1.5 SD away from the mean, the AP duration is -0.5 SD away from the mean, and all other measures are equal to the mean, then the fitness of this model is assigned the score of 2. In this system, higher scores imply inferior models. A score of zero indicates that the model is initially at rest and the measured features exactly fit the mean values of the experimental data. The feature-based fitness function score, Score_F, is computed using the following equation

$$Score_F = \sum \left| \frac{F_{GA,i} - \mu_i}{\sigma_i} \right|$$

where i is the index of the current feature, $F_{GA,i}$ is the computed value of feature i, μ_i is the experimental mean of feature i, and σ_i is the experimental SD of feature i.

3.1.2.3 Combined Fitness Function

Others have seen increased performance for optimizing neuron models with GAs when increasing the number of constraints by combining fitness functions [71]. Therefore, we combined the two fitness functions by summing the output of each fitness function into a single score. However, the output of each fitness function had to first be normalized since each fitness function provides a different type of output. The normalization is done by dividing the score returned by the GA for each fitness function by the score produced by the manual-tuned model using the same fitness function. The score used by the combined fitness function, $Score_C$, is computed using the following equation

$$Score_C = \frac{Score_T}{Score_{MT}} + \frac{Score_F}{Score_{MF}}$$

where $Score_T$ and $Score_F$ are computed as above, $Score_{MT}$ is the score of the manual-tuned model using the template-based fitness function, and $Score_{MF}$ is the score of the manual-tuned model using the feature-based fitness function.

3.1.3 Hypoglossal Motoneuron Model

The HM model is taken from the previous chapter and can be found in published form [103]. The model of Chapter 2 is hereafter referred to as the model of Purvis and Butera [103]. The model is a Hodgkin-Huxley [21] style, single-compartment, electrophysiological model of a HM from a neonatal rat containing a repertoire of ionic currents. The currents found in the HM model include the fast sodium and delayed-rectifier potassium currents, high- and low-voltage-activated calcium currents, voltage- and calcium-dependent potassium currents, a hyperpolarization-activated cationic current, and a persistent sodium current. The model is composed of these currents with parameters determined from experimental data where possible, along with a simplified model of the dynamics of internal calcium concentration. The model reproduces several characteristics of HMs and replicates the neuron's response to pharmacological experiments. The model was previously used to explore the roles of each current in shaping action potential dynamics, and to explore the age-dependent changes seen in HMs [103]. The model consists of 16 differential equations and contains 89 free parameters.

3.1.4 Simulations

MATLAB (Mathworks, VA) and the "The MATLAB Genetic Algorithm Toolbox" [107] are used to run the GA. Model simulations are performed using the interactive differential equation simulation package XPP [108]. Each generation is run on a Beowulf computing cluster consisting of 54 2.4GHz (or higher) PCs running Redhat Linux 9.0. Perl scripts are used to communicate between MATLAB and XPP and to submit simulations to the cluster. In the GA, populations consist of 1,000 individuals and evolve for 100 generations. Toolbox default settings of 70% and 0.4% are used for crossover and mutation rates, respectively. Data is saved every 0.2 ms in the simulations, and as a result, the minimum z-score for AP duration is 0.19 (see AP duration scores in Table 4 through Table 6). Wilcoxon ranked sum tests were performed to determine statistical significance ($p<0.05$ unless otherwise stated) among the results of multiple simulations.

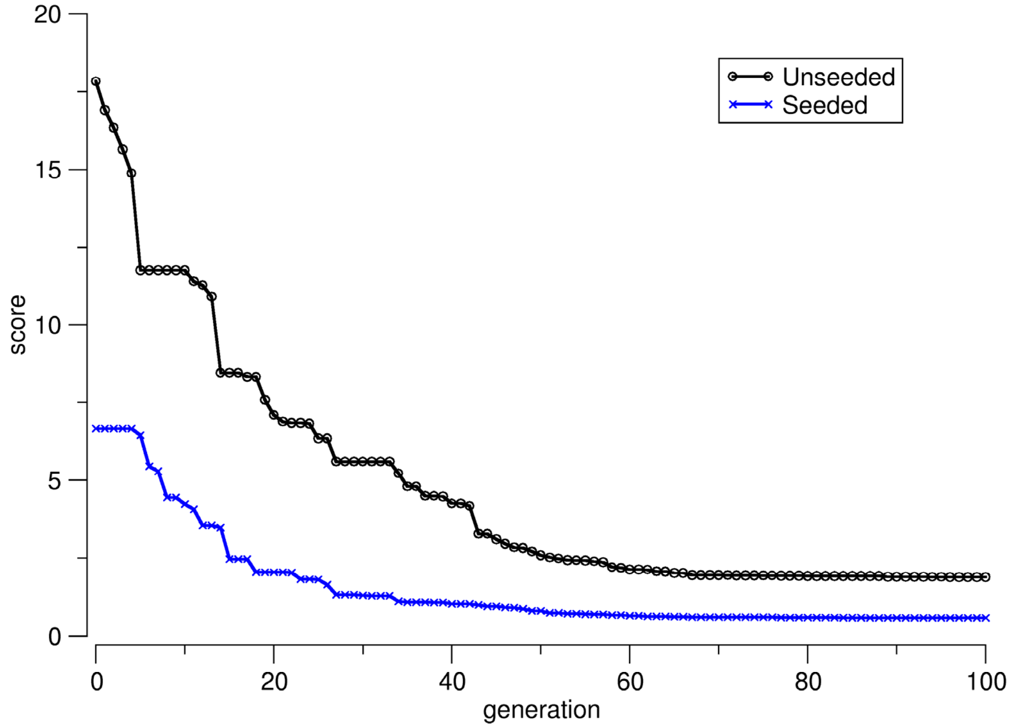

Figure 16. Best score of each generation from an unseeded (black) and seeded (blue), feature-based GA. Score levels off at around generation 60.

3.2 Results

First, we used the template-based fitness function to optimize the HM model with seeded and unseeded populations. Then we used the feature-based fitness function (seeded and unseeded). Next we combined the two fitness functions and compared the results. Finally, we explored the acceptable range of parameter space by extending the allowable range of parameters. Figure 16 illustrates the progression of the total score of the best model for each generation when optimizing the parameters of a neonatal HM model using a seeded and unseeded, feature-based fitness function. The results in Figure

16 are also indicative of all GA simulations in this study. The score quickly levels off after around 50-60 generations with only minor improvements in performance from generation 60 to generation 100. When referring to the best model for each simulation, the best model is the individual in the population with the lowest score at generation 100. After 100 generations, the parameters of the best scoring individuals converge. For example, the parameters among the 200 best scoring individuals have a mean coefficient of variation of 0.0016 for the seeded, feature-based GA. Therefore, the parameter set of the best model is representative of the best scoring members of the final population.

3.2.1 Template-Based Fitness Function

Our first task was to optimize the model produced by manual tuning [103] to fit the experimental measures for AP shape [64] using the template-based approach. For the template-based GA, the fitness function is an AP drawn by hand to fit the experimental measures for each feature. The template waveform only considers the AP shape, it does not consider R_N. The hand drawn template perfectly matched the experimental mean values for rest, AP amplitude, AHP amplitude, and AHP half-duration. AHP duration was 0.3 ms too short (-0.01 SDs away from the mean), and the temporal quantization error from AP duration produces an AP duration that is an additional 0.19 SDs away from the mean. Thus, the features of the hand drawn template sum to a total of 0.20 SDs away from the experimental mean.

The results of the best model produced using the template-based simulations and the hand drawn template AP are given in Figure 17. As stated above, the goal of this optimization is to create a model that will closely match the experimental measures for neonatal HM AP shape reported by Viana et al. [64]. The AP measures of the unseeded, template-based model shown in Figure 17 sum to a total of 4.85 SDs away from the experimental mean. Though rest and AP duration closely match the mean experimental values, all other features vary significantly from the experimental measures (Table 4). An error on R_N could be expected, since it is the only feature not directly characterized by the template AP. The error from AHP half-duration is almost as large as that of R_N (Table 4). Nine additional simulations were run using different random seeds and the problems with the first simulation were consistent among all ten simulations. After ten simulations, the unseeded, template-based approach failed to produce an action potential that closely matched the experimental data. Only 1/10 simulations performed better than the HM model developed by manual tuning [103]. The average number of SDs away from the experimental mean for all features after ten simulations for the unseeded, template-based GA was 8.44 (+/- 21%).

Next we seeded the initial population with one individual containing the nominal parameter set previously developed through manual tuning [103]. As seen in Figure 17, the seeded, template-based approach produced a model that closely matches the hand-drawn template AP. The best model generated using the seeded, template-based approach produces an AP that is 1.04 SDs away from the mean, and has minor variations from the mean for all features (Table 4). For the seeded GA simulations, only one member of the initial population is seeded with the parameters of Purvis and Butera [103]. The 999 other members of the initial population are randomly generated from within the limits specified above. Nine additional simulations were run where these 999 members of the initial population were generated using different random seeds. The average number of SDs away from the experimental mean for all features after ten

Table 4. Measure and z-score of template-based GA (seeded and unseeded) for each experimental feature. Data is taken from Viana et al. [64]. Standard error measures reported by Viana et al. [64] have been converted to SD for this publication. The TOTAL is the sum of the absolute values of each individual z-score and represents the number of SDs away the model is from the experimental mean. The total of the hand-drawn template waveform is 0.20. GA results are from the best performing model after ten simulations.

FEATURE	Neonatal Data		Template-based GA			
			Unseeded		Seeded	
	MEAN	+/- SD	MEASURE	Z-SCORE	MEASURE	Z-SCORE
Rest	-69.6 mV	5.47 mV	-69.6 mV	0.01	-69.5 mV	0.01
AP amp	87.3 mV	6.25 mV	84.2 mV	-0.50	86.0 mV	-0.21
AP dur	0.97 ms	0.16 ms	1.0 ms	0.19	1.0 ms	0.19
AHP amp	-9.3 mV	2.68 mV	-7.4 mV	0.69	-9.1 mV	0.08
AHP dur	110.5 ms	26.12 ms	102.0 ms	-0.32	113.6 ms	0.12
AHP 1/2-dur	39.4 ms	9.22 ms	52.8 ms	1.45	41.4 ms	0.22
R_N	29.4 MΩ	11.5 MΩ	10.1 MΩ	-1.68	31.8 MΩ	0.20
TOTAL	-	-	-	4.85	-	1.04

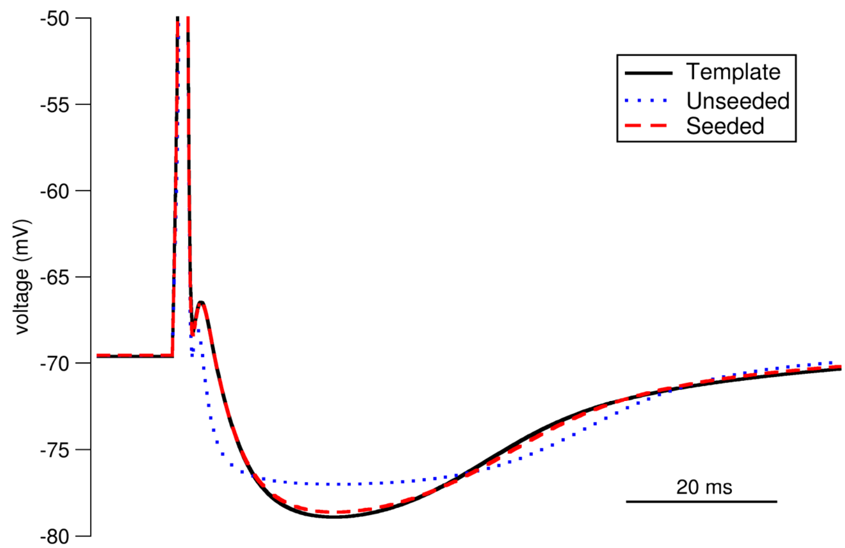

Figure 17. Comparison of the hand-drawn template (solid line), and the APs produced by the unseeded (dotted line) and the seeded (dashed line), template-based GA. Detailed measures for each feature are given in Table 4. AP is evoked by a brief (1 ms) current pulse of 1 nA. AP is truncated to emphasize the features following the spike.

simulations for the seeded, template-based GA was 2.64 (+/- 28%). As expected, the seeded populations performed consistently better than the unseeded populations and also performed better than the manually tuned model.

Since R_N is not directly characterized by the template AP, we computed the seeded, template-based results in the absence of the measure for R_N. The average z-score contributed by the R_N error for the ten simulations was 1.65. Therefore, the average number of SDs away from the experimental mean for all remaining features after ten simulations for the seeded, template-based GA in the absence of R_N was 0.99.

3.2.2 Feature-Based Fitness Function

Figure 18 provides a comparison of both the manually tuned model output and the best model APs produced by the feature-based simulations. As seen in Figure 18, the GA is able to generate models that result in a higher resting potential and a larger AHP amplitude compared to the manually tuned model. A detailed score for each feature for both the manually tuned model and the feature-based GA is given in Table 5. Table 5 reveals that the model produced by the unseeded GA performs better for almost every measured feature when compared to the model produced by manual tuning. The manually tuned model is 6.24 SDs away from the mean and the best unseeded, feature-based GA model is 1.88 SDs away from the mean. The main shortcomings of the unseeded model are an R_N that is almost 20 MΩ too low, a resting potential that is too high, and an AHP that is too small (Table 5). Nine additional simulations were run using different initial populations. Low R_N and a high resting potential are consistent problems among the ten simulations with the unseeded, feature-based GA. The average number of

Table 5. Measure and z-score of manually tuned model and feature-based GA (seeded and unseeded) for each experimental feature. Experimental data is given in Table 4 and taken from Viana et al. [64]. The TOTAL is the sum of the absolute values of each individual z-score and represents the number of SDs away the model is from the experimental mean. GA results are from the best performing model after ten simulations.

FEATURE	Manual tuning		Feature-based GA			
			Unseeded		Seeded	
	MEASURE	Z-SCORE	MEASURE	Z-SCORE	MEASURE	Z-SCORE
Rest	-72.89 mV	-0.60	-68.8 mV	0.14	-69.3 mV	0.06
AP amp	87.23 mV	-0.01	87.3 mV	-0.004	87.3 mV	0
AP dur	1.4 ms	2.75	1.0 ms	0.19	1.0 ms	0.19
AHP amp	-5.60 mV	1.38	-9.0 mV	0.12	-9.2 mV	0.03
AHP dur	105.4 ms	-0.20	110.6 ms	0.004	110.4 ms	0.004
AHP 1/2-dur	41.4 ms	0.22	39.4 ms	0	39.4 ms	0
R_N	41.82 MΩ	1.08	13.0 MΩ	-1.42	29.3 MΩ	-0.01
TOTAL	-	6.24	-	1.88	-	0.30

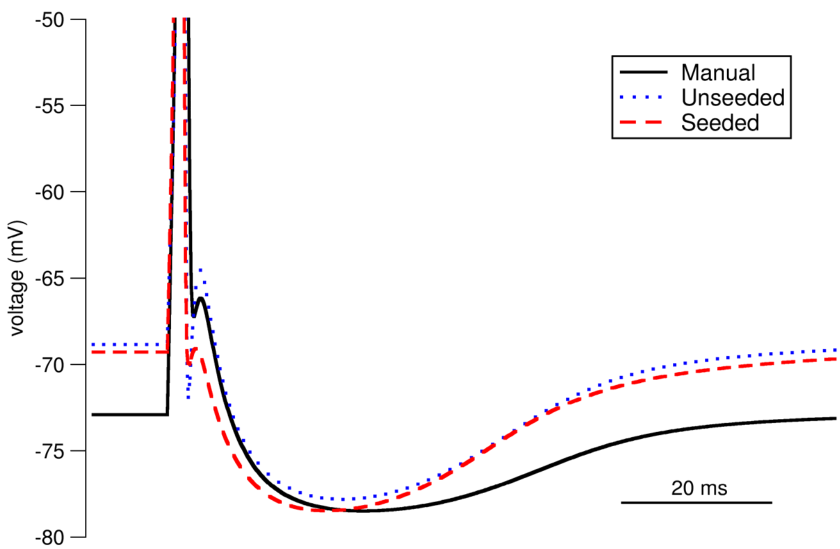

Figure 18. Comparison of manually tuned model (solid line), unseeded (dotted line), and seeded (dashed line), feature-based GA. Both unseeded and seeded GA results closely match experimental data for action potential (AP) shape (see Table 5). AP is evoked by a brief (1 ms) current pulse of 1 nA. AP is truncated to emphasize the features following the spike.

SDs away from the experimental mean for all features after ten simulations for the unseeded, feature-based GA was 4.28 (+/- 37%).

We again seeded the initial population and after 100 generations, the model produced an action potential (Figure 18) whose measures are 0.30 SDs away from the mean. This means that the seeded, feature-based GA produced a model that has a total difference for all seven measures that is less than one-half of one SD away from the experimental mean. The model produced by manual tuning [103] suffers from a resting potential that is too low, an AP duration that is too long, an AHP amplitude that is too small, and an input resistance that is too high (Table 5). The seeded, feature-based GA was able to produce a model that almost perfectly fits the experimental mean for all of these features.

The results just described are also representative of the nine additional simulations run. The average number of SDs away from the experimental mean for all features after ten simulations for the seeded, feature-based GA was 0.69 (+/- 47%). After ten simulations for both seeded and unseeded feature-based GAs, the worst seeded, feature-based GA (1.24 SDs away from the mean) is better than the best unseeded, feature-based GA (1.88 SDs away from the mean). All seeded and 8/10 unseeded, feature-based optimizations produced models that score better than the manually tuned model.

3.2.3 Combined Fitness Function

Finally, we used the combined fitness function (seeded only) to optimize the HM model. As before, ten simulations were run using different random seeds and the APs produced by the three best models generated using the combined fitness function are illustrated in Figure 19. Compared to the experimental data, the features of these three models are a total of 0.48, 0.51, and 0.77 SDs away from the mean (Table 6). The average number of SDs away from the experimental mean for all features after ten simulations for the seeded, combined GA was 0.97 (+/- 42%).

Since the template-based results provided a large error for R_N, we also computed the results of the combined simulations in the absence of R_N. The average SD contribution from R_N for the ten combined GA simulations was 0.51. Therefore, the average number of SDs away from the experimental mean for all remaining features after ten simulations for the combined GA in the absence of R_N was 0.46. The error contributed by R_N for both the seeded template and combined GA is over 50% of the total error for that method. As seen in Table 6, if the z-score contributed by R_N is removed from the three best scoring combined GA simulations, the resulting models are only 0.24, 0.29, and 0.33 SDs away from the experimental mean of the remaining features.

3.2.4 Fitness Function Comparison

After 50 simulations, the best individual model was generated using the seeded, feature-based fitness function alone when comparing the results to the experimental measures of Viana et al. [64]. On average, the seeded, feature-based simulations provided the closest fit to experimental data, but the difference in the seeded, feature-based and combined simulation results was not statistically significant ($p=0.12$). The seeded, feature-based GA also produced the greatest variability among simulations with an average score that varied by +/- 47% among the ten simulations. The seeded, template-based and combined GA produced variations of +/- 28% and 42%, respectively. The higher variability of the feature-based compared to the template-based GA may not

Table 6. Measure and z-score of best three models using the combined GA for each experimental feature. Experimental data is given in Table 4 and taken from Viana et al. [64]. The TOTAL is the sum of the absolute values of each individual z-score and represents the number of SDs away the model is from the experimental mean.

FEATURE	Combined GA					
	1		2		3	
	MEASURE	Z-SCORE	MEASURE	Z-SCORE	MEASURE	Z-SCORE
Rest	-69.4 mV	0.04	-69.5 mV	0.03	-69.3 mV	0.05
AP amp	87.3 mV	0	87.2 mV	-0.02	87.3 mV	0
AP dur	1.0 ms	0.19	1.0 ms	0.19	1.0 ms	0.19
AHP amp	-9.3 mV	0	-9.2 mV	0.03	-9.1 mV	0.06
AHP dur	110.4 ms	0	110.4 ms	0	109.6 ms	-0.03
AHP 1/2-dur	39.4 ms	0	39.6 ms	0.02	39.4 ms	0
R_N	32.2 MΩ	0.24	32.0 MΩ	0.22	34.4 MΩ	0.44
TOTAL	-	0.48	-	0.51	-	0.77

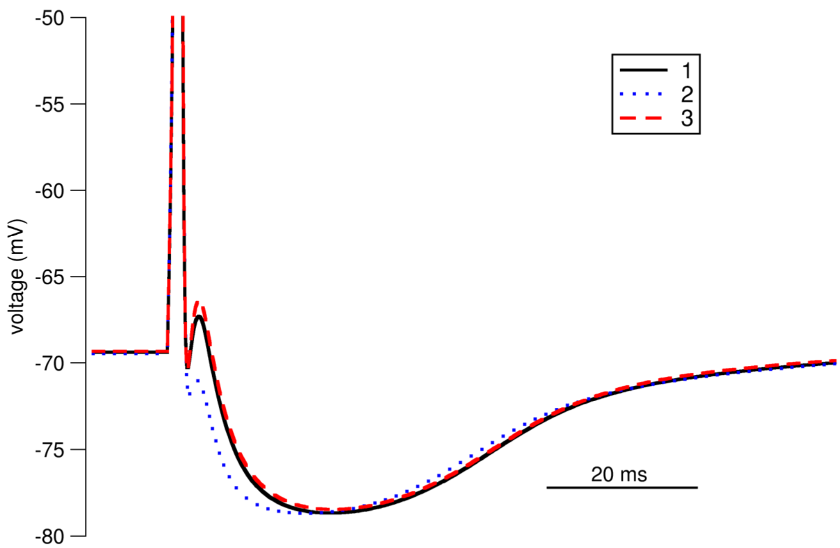

Figure 19. Best three APs produced using the combined fitness function. Detailed measures for each feature are given in Table 6. AP is evoked by a brief (1 ms) current pulse of 1 nA. AP is truncated to emphasize the features following the spike.

pose a problem given that the feature-based optimizations consistently out-performed the template-based optimizations.

Since R_N is not measured using the template waveform, we re-computed the results of the seeded GA simulations in the absence of R_N. In this case, both the template and the combined GA provide a marked improvement. The template-based GA continues to be the worst performing method, but the combined fitness function now provides the best fit to the remaining features (although the difference between the combined and the seeded, feature-based results is not statistically significant). The average number of SDs away from the mean for each method in the absence of R_N is as follows: template = 0.99, feature = 0.58, and combined = 0.46.

The preceding discussion compared the output of the best model from each simulation to the experimental data of Viana et al. [64]. The results of simulations employing each fitness function were also compared by scoring the best model produced by a given fitness function using each of the other two fitness functions. For example, the ten best models (one model from each of the ten simulations) produced using the seeded, feature-based fitness function were scored using the template-based fitness function and using the combined fitness function. The results of these comparisons are illustrated in Figure 20. As expected, the results using a given fitness function perform best for that fitness function (i.e. the results of the template-based simulations score better than the results of the feature-based and combined simulations when using the template-based fitness function, Figure 20A). However, when the results of the combined simulations are scored using the feature-based fitness function (Figure 20B), there is no statistically significant difference between the combined results and the feature-based

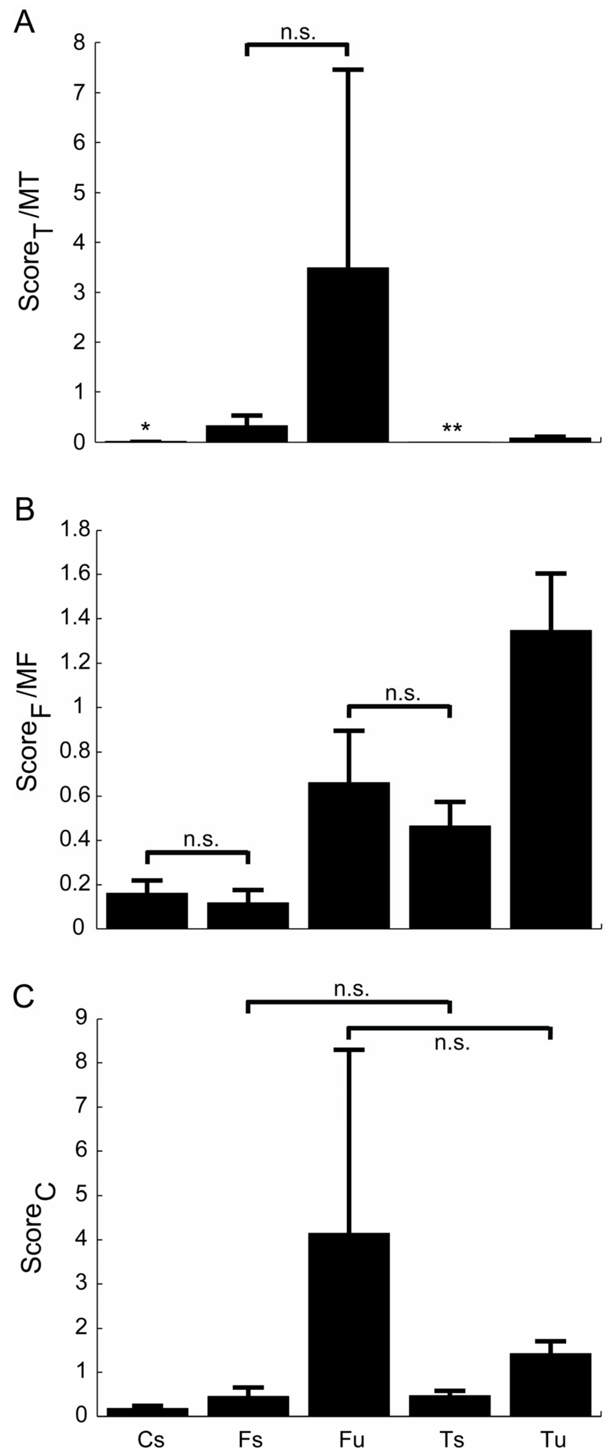

Figure 20. Average scores after 10 simulations of best models for the seeded, combined simulations (Cs), the seeded and unseeded, feature-based simulations (Fs and Fu), and the seeded and unseeded, template-based simulations (Ts and Tu). Results are scored using the template-based fitness function (**A**), the feature-based fitness function (**B**), and the combined fitness function (**C**). Scores given in **A** and **B** are normalized by the score produced using the manually tuned model, as described in Section 3.1.2.3. The differences between all scores are statistically significant ($p<0.005$) except where noted by n.s. (not significant). * Mean = 0.013 (+/-0.0075). ** Mean = 0.0015 (+/-0.0006).

results for the seeded simulations (although statistical significance might be achieved if more simulations are run). The results of the combined simulations score well for each type of fitness function. The feature-based simulations do not perform well using the template-based fitness function, but the template-based simulations score well using the feature-based fitness function. When comparing seeded to seeded and unseeded to unseeded, the feature and template-based simulations perform equally well (not statistically different) when using the combined fitness function (Figure 20C).

3.2.5 Parameter Comparison

In an attempt to determine the causes of the improved model performance, we examined the parameters of the best models for all simulations. Figure 21 illustrates the large variability of the maximum conductances of the best models for all twenty unseeded simulations (Figure 21A) and the lack of variability among the maximum conductances for all thirty seeded simulations (Figure 21B). The maximum conductances for the ten simulations with the unseeded, template-based GA differ greatly compared to the nominal parameter set with an average difference of 1.009 μS. The average variation of all non-conductance parameters for the ten unseeded, template-based simulations is 5.41%. The maximum conductances for the seeded, template-based GA were similar to the manually tuned model (average difference of 0.011 μS), and all other non-conductance parameters varied by an average of 4.95%. For the unseeded, feature-based GA, the maximum conductances show an average difference of 0.852 μS compared to the nominal parameter set, and all non-conductance parameters vary by an average of 5.41%. For the seeded, feature-based GA, the maximum conductances differ by an average of only 0.004 μS. The non-conductance parameters vary by an average of 4.28%. The

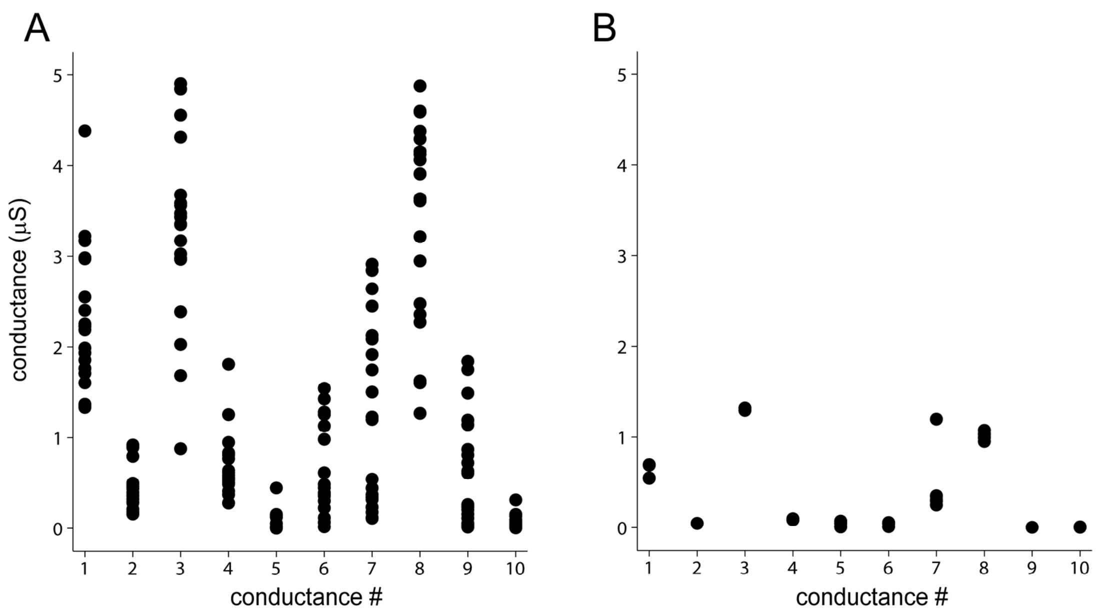

Figure 21. Maximum conductance values of best models for all simulations. Conductance range and # is given in Table 3. **A**: Template- and feature-based, unseeded simulations (20 models total). Maximum conductances vary significantly over the allowable range. **B**: Template-based, feature-based, and combined, seeded simulations (30 models total). Little variability exists for the maximum conductances of the seeded models.

maximum conductances for the ten simulations with the combined fitness function display similar trends to the other seeded methods. The maximum conductances for the combined GA were similar to the manually tuned model (average difference of 0.015 μS), and all other non-conductance parameters varied by an average of 4.35%. The significance of these parameter changes will be addressed in the discussion.

3.2.6 Parameter Ranges

We also performed simulations that allowed a greater range of all parameters values. Instead of using the +/- 10% for all non-conductance parameters in the model, half-(in)activation values were allowed to vary by as much as 50 mV from their nominal value, and slope factors were allowed to vary from 2-20. Similarly, time constants, reversal potentials, and maximum conductances were given greater ranges. With such wide parameter ranges, the GA was still able to produce APs that closely matched the experimental measures. However, these models employed some aphysiological ionic mechanisms that were not used as constraints. Although it was not the case in this study, discovering new mechanisms for producing characteristic features of a neuron is a potential benefit of using an automated search technique when investigating an unknown mechanism.

When using an automated optimization technique to fit model parameters, it is imperative that the model be tested to determine whether or not the new parameters produce a realistic model. For example, the AHP should be completely eliminated when I_{SK} is removed from the model [58]. We tested this with the models produced by the GA. Removing I_{SK} from the model with the extended allowable range of parameters had little effect on the shape of the AP. Instead, I_A was responsible for producing the AHP. Since the simulations with increased allowable parameter ranges produced unrealistic models, they were not further studied. Conversely, the more reduced ranges from the previous simulations provide models that contain realistic mechanisms and closely match the experimental measures.

3.3 Discussion

The GA produced models that more accurately reproduced experimental measures of AP shape than the model developed through manually tuning model parameters. When compared to the experimental measures, the manually tuned model is 6.24 SDs away from the mean. The best model produced by the GA in this study was generated using the feature-based fitness function alone and had features that measured a total of 0.30 SDs away from the experimental mean.

3.3.1 Fitness Function Comparison

Vanier and Bower [70] recommend including template waveforms in the fitness function when computational costs allow. Davison et al. [104] achieved poor results when using a template waveform, but performance improved when fitting to spike times, a feature-based measure. Weaver and Wearne [105] achieved good results after improving the template waveform fitness function of Davison et al. [104] by first aligning target and model APs before calculating the error. (This improvement is not necessary for our study since we are fitting to a single action potential triggered by a stimulus current at a specified time.) Keren et al. [71] obtained the best results when using a combination of metrics that included a measure of spike times and waveforms. Tabak et al. [106] also recommend using multiple methods for parameter estimation of neuron models after comparing time- and frequency-domain methods. Our simulations explored template-based and feature-based methods and revealed that a feature-based fitness function consistently provided parameter sets that more closely matched the experimental data than the parameter sets generated using the template-based fitness function. The difference between the results of the seeded, feature-based and combined simulations was not statistically significant ($p=0.12$). The feature-based simulations continued to outperform the template-based simulations when the error contributed by R_N was excluded from the calculation. However, if R_N is excluded from the combined fitness function score, then the combined fitness function produced models whose remaining features more closely matched experimental data (but again, the difference between the combined and feature-based simulations was not statistically significant). As expected, all results were enhanced when seeding the initial population with one model containing the nominal parameter set of Purvis and Butera [103]. On average, the unseeded, template-based approach provided parameter sets that are inferior to the model produced by manual tuning. In fact, only one out of ten of these simulations scored better than the manually tuned model.

Why does our feature-based fitness function outperform the template-based fitness function for optimizing the shape of the neonatal HM AP? We suggest the following: The feature-based fitness function employed in this study assigns equal value to each of the measures listed above. Many of these measures can be characterized by only one or two data points in the voltage trace. On the other hand, the template-based fitness function, due to the distribution of data points, weights some measures more than others (e.g. resting potential will be weighted higher than AP duration). If the GA quickly satisfies one of the higher weighted features, the solution could more easily get stuck in a local minimum of parameter space. Potential improvements to our template-based approach are listed in Section 3.3.3 below. If the desire is to fit certain experimental measures of AP shape, as it was in this study, then the unequal weighting of features when using a template-based approach should be carefully considered in future template-based studies. The HM AP is an example of a complex AP shape where a simple template-based approach provides inferior performance compared to a feature-based approach.

A cross validation of the fitness functions reveals that the combined fitness function scores well for all three types of fitness functions (Figure 20). This should be expected since the combined fitness function is a simple combination of the other two fitness functions. The cross validation also reveals that the feature-based results do not score well using the template-based fitness function, but the template-based results do score well using the feature-based fitness function. Thus, a good fit to the template waveform implies a good fit to the experimental features, but a good fit to the experimental features does not imply a good fit to the template waveform. This comparison was further verified by comparing the individual scores for each simulation (not shown).

3.3.2 Significance of Non-Conductance Parameters

Although the results of multiple unseeded simulations produce high variability among all parameters, the results from multiple seeded simulations produced parameter sets with little variation among maximum conductances (Figure 21). These maximum conductances were, on average, within 0.01 nS of the value used in the manually tuned model despite the greater allowable range provided to these parameters (Table 3). Thus the total score improvement from 6.24 down to 0.30 (Table 5) for the seeded, feature-based GA was caused almost exclusively by changes of less than 10% in the other, non-conductance parameters. This is a serendipitous discovery that resulted from the use of an automated optimization technique. Typically modelers might be biased towards mainly altering maximum conductances to fit experimental measures [71, 73, 103, 105, 109, 110]. The lack of change in the maximum conductances for the seeded, feature-based GA may be due to the location of these parameters in the chromosome and the crossover method. In our chromosome, maximum conductances are listed first and the GA uses single-point crossover. This will result in maximum conductances that are usually grouped together. The effect of alternate crossover methods or parameter placement inside the chromosome was not investigated in this study. Regardless of the cause of the phenomenon in this study, the importance of this discovery has clear implications for future parameter searches using neuronal models. Since even small changes (less than 5% on average) of parameters other than maximum conductances can lead to drastic improvements in model performance, the modeler should consider allowing all parameters to vary when using automated optimization techniques. It is possible that when close to an ideal solution (as in the seeded case), non-conductance parameters are more effective tuning parameters, while when starting in a global sense with no bias (as in the unseeded case), conductance parameters are most effective at tuning the model towards an optimal solution. This idea has not been fully investigated.

3.3.3 Limitations and Improvements

There are countless variations of GA strategies that can be included in any GA study. Some of these include different selection strategies for crossover, different rates of mutation, and inclusion of subpopulations and migration. It is possible that the poor results obtained using the unseeded, template-based simulations could be improved by using, for example, a higher mutation rate. However, in this study we are not concerned with finding the "best" possible GA to solve our problem. Rather, we are employing a freely available and easy to use GA toolbox with its default settings [107] to compare different types of fitness functions for optimizing a HM model.

For this study, the template-based approach produced inferior models. Though the model may produce acceptable scores for quantifiable measures of the template used (e.g. AP amplitude, AP duration, etc.), this method provides no direct measure for R_N. Therefore, this method could produce frequency-current (F-I) curves that do not match experimental data. An alternative would be to use multiple templates of the response to neurons at varying current levels [73]. This requires much more computation time, but would ensure a better fit to experimental F-I data. There are other potential improvements to the template-based approach used in this study. The template AP was hand-drawn to fit the mean values of the data for each feature, rather than using experimental recordings from actual cells. Though the hand-drawn AP nearly perfectly fit the experimental measures, it could suffer from errors introduced either by the "artist" or the method used to create the template. The final template shape (though it looks good to the naked eye) may not be biological, and therefore the model would not be expected to produce an AP that closely fits the template. Since the seeded, template-based and combined results were able to closely match the template waveform, artistic error does not seem to be a problem in this study. The template method might also be improved by more finely sampling the voltage trace. Simply decreasing the time step, though it would give more points during the 1 ms AP, would also increase the total number of points during all other phases of the voltage trace. Instead, increasing the number of data points only during the AP itself would more heavily weight the AP for the SSE measure. This may provide increased performance. However, weighting distinct parts of a voltage trace to enhance the importance of certain aspects of a waveform is the first step towards creating a feature-based method. Our results have shown that a feature-based fitness function performs significantly better than a template-based fitness function when fitting the complex action potential shape of hypoglossal motoneurons.

CHAPTER 4: SIGNIFICANCE OF PACEMAKERS IN THE PBC

In the previous chapters, we developed and optimized an ionic current model of a hypoglossal motoneuron. The hypoglossal motoneuron transmits the breathing rhythm out of the transverse slice to the muscles. In this chapter, we turn our attention to the pre-Botzinger complex (pBC), the group of cells that initiates the breathing rhythm in the transverse slice. In the pBC, the ratio of critical sub-threshold currents determines whether or not the cell is capable of intrinsic bursting. We will vary the ratio of certain sub-threshold currents in a previously developed ionic current model of pBC cells to determine the role of intrinsic bursters, or pacemakers, in this network.

The pBC is a vital sub-circuit of the respiratory central pattern generator. Although the existence of neurons with pacemaker-like bursting properties in this network is not questioned, their role in network rhythmogenesis is unresolved. Modeling is ideally suited to address this debate because of the ease with which biophysical parameters of individual cells and network architecture can be manipulated. We modeled the parameter variability of experimental data from pBC bursting pacemaker and non-pacemaker neurons using a modified version of our previously developed pBC neuron and network models. In order to investigate the role of pacemakers in network-wide rhythmogenesis, we simulated networks of these neurons and varied the fraction of the population made up of pacemakers. For each number of pacemaker neurons, we varied the amount of tonic drive to the network and measured the frequency of synchronous network-wide bursting produced. Excitatory networks with all-to-all coupling, as well as sparsely connected networks were explored for several levels of synaptic coupling strength. Networks containing only non-pacemakers were able to produce network-wide bursting, but with a low probability of bursting and a low input and output range. Our results indicate that inclusion of pacemakers in an excitatory network increases robustness of the network by more than tripling the input and output range compared to networks containing no pacemakers. The largest increase in dynamic range occurs when the number of pacemakers in the network increases above 20% of the population. Experimental tests of our model predictions are proposed.

4.1 Methods

This section describes the experimental data, the modified version of the model of Butera et al. [18, 19], and the techniques used to model the experimental data in this study. We also describe how the simulations and data analysis are performed.

4.1.1 Experimental Data

Experimental data obtained from neonatal rat pBC inspiratory neurons *in vitro* shows from voltage-clamp recording analysis that a primary difference between pacemakers (PMs) and non-pacemakers (NPMs) in the pBC is the ratio of the persistent sodium conductance to the leak conductance (g_{NaP}/g_{Leak}): all pBC inspiratory neurons that have been analyzed *in vitro* to date exhibit NaP and K^+-dominated leak currents, but the g_{NaP}/g_{Leak} ratio is larger in PMs than in NPMs [8, 52]. When viewing the recent data of Koizumi and Smith [52] as a scatter plot in g_{NaP} and g_{Leak} space (Figure 22A), there is a clear distinction between the PMs and NPMs (dashed line). In order to accurately compare the experimental data to the model (see below) in terms of conductance densities, the data for individual neurons (n=50) was normalized by the measured

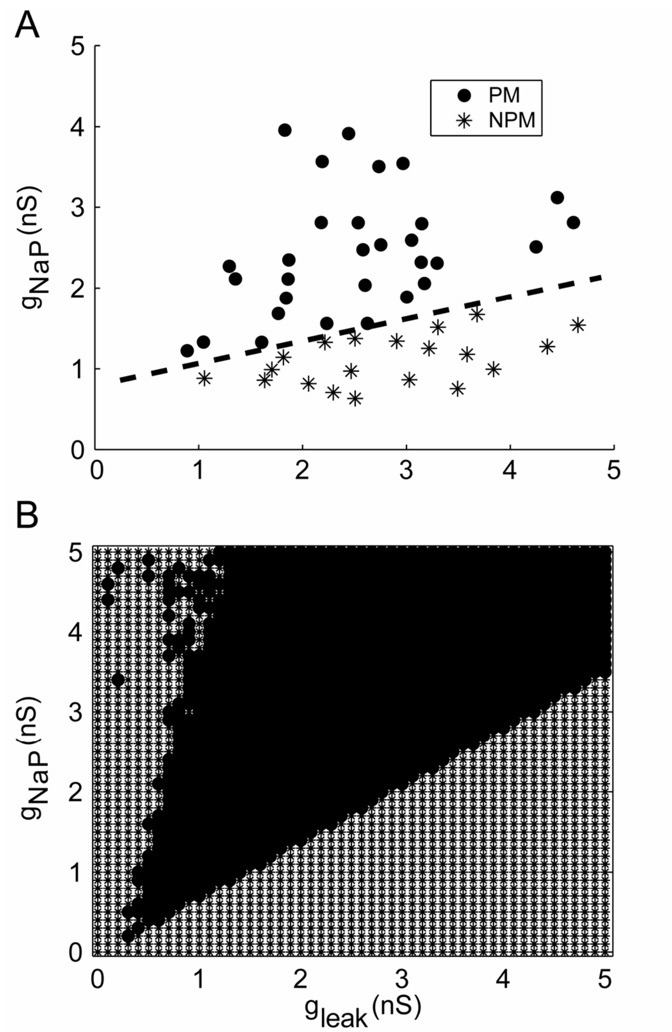

Figure 22. Parameter space and PM/NPM boundaries for experimental data and the model. Pacemakers are circles (●), non-pacemakers are stars (*). **A**: Scatter plot of experimental data "H. Koizumi and J.C. Smith, unpublished observations" obtained from voltage-clamp analysis of PM/NPM neurons identified in the pBC of neonatal rat in vitro slice preparations, employing neuron visualization and recording techniques similar to those described previously (Del Negro et al. 2002a; Koshiya and Smith 1999). Note the clear boundary between pacemakers and non-pacemakers (hand-drawn dashed line). n = 30 PMs, and n = 20 NPMs. **B**: Model's PM/NPM boundaries. The parameter set was classified as a PM if the model neuron bursts occurs at any level of stimulus current (dark region).

capacitance and then multiplied by the nominal whole-cell capacitance used in the model (21 pF). PMs used for this analysis were differentiated from NPMs after pharmacological block of glutamatergic excitatory synaptic currents as previously described [8, 13], and the dependence of intrinsic rhythmic bursting on g_{NaP} was confirmed pharmacologically for identified PMs. All g_{NaP} and g_{Leak} data used in this study are from the set of PMs and NPMs obtained by Koizumi and Smith [52] and are reproduced here for data parameter space mapping, model parameter adjustments, and data-model comparisons.

4.1.2 Neuron Model

This study uses our previous pBC neuron model (see APPENDIX C) and heterogeneous excitatory network models of these cells [18, 19]. The neuron model (Model 1 of [18]) is a Hodgkin-Huxley [21] style, electrophysiological model of a bursting pBC cell. The model consists of three voltage-gated ionic currents and a K^+-dominated ohmic leak current. The voltage-gated currents are: 1) a fast Na^+ current, 2) a delayed-rectifier K^+ current, and 3) a *slowly-inactivating* persistent Na^+ current (NaP). NaP is responsible for the intrinsic voltage-dependent, rhythmic bursting behavior displayed by these neurons (i.e. this is a model of the NaP-dependent, or cadmium-insensitive bursters; [18]). This is the biophysically minimal set of currents required to describe the main features (below) of pBC neuron properties. Other currents include a tonic excitatory drive current and an excitatory synaptic current. The excitatory drive, modeled as g_{tonic}, models input from a tonic spiking population, which is proposed to function for pBC network burst frequency control (e.g. see [19, 39]). The excitatory synaptic current models the EAA-mediated coupling between individual bursting neurons in all simulations using the conductance g_{syn} [19].

We should note that, although PMs are not required to produce network-wide bursting in our model [19], the NaP current is required. If this slowly inactivating inward current were completely removed from our model, there would be no slow process in the network to terminate network-wide bursting activity once it has begun. Thus we emphasize that NaP provides not only a mechanism for rhythmic bursting of individual PMs (when isolated from synaptic input), but also a mechanism for synchronized rhythmic bursting and its termination at the population level. This mechanism results from the voltage-dependence and kinetics of NaP inactivation and the dynamic interaction of NaP current with phasic excitatory synaptic drive currents in the coupled population of cells (see Figure 10 of [19]).

Some parameters of the original Model 1 neurons were adjusted to more closely match recent experimental data. Specifically, more accurate values for NaP half-activation ($V_{1/2max}$ = -45 mV) and slope factor (k = 5) are employed [52]. Since the NaP half-activation value was hyperpolarized by 5 mV, we also hyperpolarized the NaP half-inactivation by 5 mV. These adjustments are also consistent with other measurements of NaP properties of neurons isolated from the pBC region *in vitro* [67, 111]. NaP inactivation kinetics have not been quantified experimentally for pBC neurons, so the original Model 1 kinetics were employed. Simulations with these adjusted models provide very similar behavior to the original Model 1 neurons including voltage-dependent rhythmic bursting with a similar range of oscillation frequencies, controllable by applied current or tonic excitatory synaptic input (see Figure 6 in [18]). Figure 23

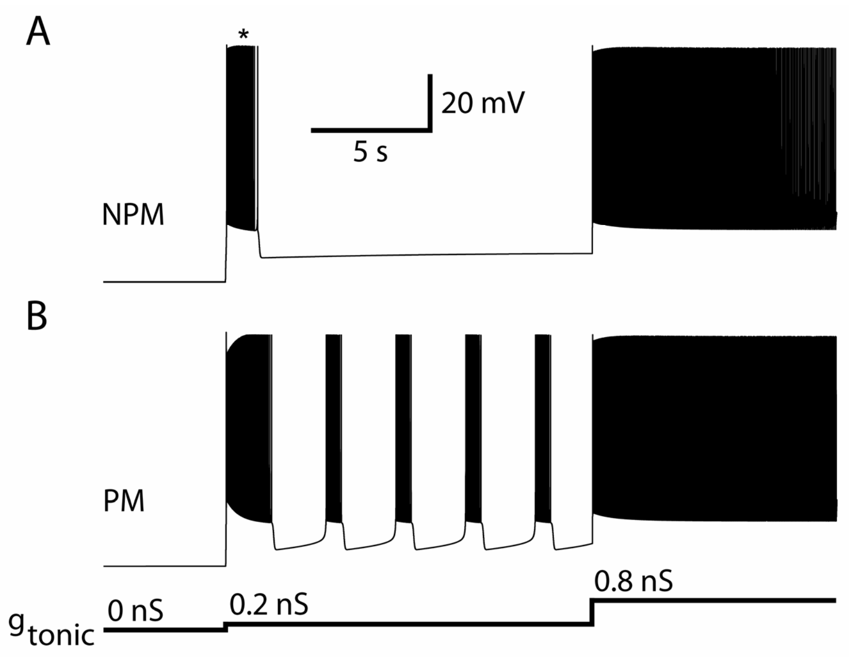

Figure 23. Model behavior for two different values of g_{NaP}. **A**: g_{NaP} = 2.0 nS. Non-pacemakers (NPM) progress from silence to beating (tonic firing) as g_{tonic} is increased. **B**: g_{NaP} = 2.5 nS. Pacemakers (PM) progress from silence to bursting to beating as g_{tonic} is increased. Only g_{NaP} is changed (g_{Leak} = 2.2 nS in **A** and **B**) to transform the NPM in **A** into the PM in **B**. *Transient firing activity in **A** is caused by step increase of g_{tonic} and is not a burst.

illustrates the pacemaker and non-pacemaker behaviors exhibited by the model for two different values of g_{NaP}. Non-pacemakers transition from silence directly to beating as excitatory drive is increased (Figure 23A, g_{NaP} = 2.0 nS); whereas pacemakers transition from silence to bursting to beating (Figure 23B, g_{NaP} = 2.5 nS). This model also captured prominent properties of the recorded data neurons, justifying our parameter sets, including: 1) silent, rhythmic bursting, and tonic spiking regimes determined by baseline membrane potential as controlled by an applied current, 2) bursting frequencies tunable over an order of magnitude range of frequencies by applied current (see also [13]), 3) subthreshold current-voltage relations obtained during slow voltage-clamp ramps (30 mV/s used to obtain the data) that are separable into g_{NaP} and g_{Leak} as the two main conductance components (see also [112]), and 4) rhythmic bursting controllable as seen experimentally by g_{NaP} and g_{Leak} (i.e. by g_{NaP}/g_{Leak} ratios). Detailed comparisons of the data-model g_{NaP}-g_{Leak} parameter spaces (Figure 24 below) also indicate that our simplified model is consistent with the differentiation between data PMs and NPMs in the majority of cases.

The network simulations required a mixed population of models of PMs and NPMs. Although previous modeling results classified the activity modes of the model (beating, bursting, silence, see Figure 7 of [18]) at rest (i.e. with no externally applied current), the PM and NPM classification of Figure 22A was experimentally determined by testing for bursting at *any* level of applied current under current clamp recording. Therefore, a similar process was applied to the model using the interactive differential equation simulation package XPP [74] for model simulations along with Perl scripts and MATLAB (Mathworks, Natick, MA) for data analysis. Both g_{NaP} and g_{Leak} were swept from 0 to 6 nS, which covers the full range of experimentally measured values. For each set of parameters represented in Figure 22B, the stimulus current was swept from -30 to +30 pA. The stimulus current was started at -30 pA to ensure that the cell is at rest. If the values of g_{NaP} and g_{Leak} are such that the model is a non-pacemaker, then the modes of activity as the stimulus current is increased will progress from silence directly to beating (Figure 23A). If rhythmic bursting occurs during part of this range (Figure 23B), the neuron is classified as a pacemaker with this parameter set. The results of these simulations are given in Figure 22B. Figure 22A,B share a clear boundary between the PM and NPM region. When creating a population of PMs and NPMs for the network simulations, the parameters must be chosen based on the modes of activity defined in Figure 22B.

Table 7. Conductance values for PMs and NPMs. Experimental data mean and SD of conductances for PMs and NPMs after mapping onto the model parameter space using 25% correction of gNaP. Computed mean and SD of model distributions after discarding/repicking procedure.

		Data		Model	
	Conductance	Mean	SD	Mean	SD
PM	g_{NaP}	2.43 nS	31%	2.44 nS	31%
	g_{Leak}	2.51 nS	37%	2.20 nS	37%
NPM	g_{NaP}	1.10 nS	27%	1.11 nS	27%
	g_{Leak}	2.82 nS	34%	3.00 nS	28%

4.1.3 Modeling Intrinsic Parameter Variability

The heterogeneous network simulations use parameters chosen from a two-dimensional parameter space (only g_{NaP} and g_{Leak} are varied). For these simulations, we created two heterogeneous populations of PMs and NPMs whose variability reflects the variability that exist in the experimental data (Table 7). That is, we constructed population distributions reflecting not only the ranges of NaP and leak conductance densities but also the experimentally determined variability of these parameters (Table 7). Accomplishing this requires completing three tasks: 1) correcting experimental conductance data for measurement errors, 2) determining the model's acceptable operating range for PMs and NPMs, and 3) defining parameter distributions inside the model's acceptable operating range that provide mean and standard deviation values consistent with the corrected experimental data.

4.1.3.1 Correcting Experimental Data

It is known that experimental measurements of g_{NaP} depend on the rate of voltage-clamp ramps [8] used to estimate values of g_{NaP}, which is consistent with our model kinetics for NaP inactivation. We simulated the ramp protocol used to determine the g_{NaP}

values of the experimental data we are attempting to model in order to produce an estimate of the underestimation due to ramp-rate. The simulation suggests an underestimation due to ramp-rate of approximately 20%, and we conservatively estimated an additional 5% error from other potential measurement errors (e.g. space-clamp). Therefore, we corrected the g_{NaP} data by multiplying by the expected underestimation of 25%. The value of g_{Leak} was not found experimentally to be affected by ramp rates as predicted by the model and was therefore left unchanged. After correcting the data, 86% of the data points are on the appropriate side of the model's PM/NPM boundary (Figure 24A).

4.1.3.2 Determining Operating Range

In order to completely describe an allowable parameter space of the model for network simulations, both the PM/NPM boundary, as well as a boundary that defines the operating range of the model must be defined. An accurate description of this space is necessary to reliably separate PM and NPM model neurons, and parameter sets outside of the model's operating range will produce spurious results (e.g. plateau potentials) or unphysiological models (e.g. negative conductances). The boundary between PMs and NPMs was chosen by fitting a diagonal line to the boundary previously computed (Figure 22B and Figure 24A). A model whose parameters lie on the PM/NPM boundary will produce doublet or triplet bursts of spikes. Therefore, the y-intercept of the line was increased by 0.2 for PMs and decreased by 0.2 for NPMs (see white space between PM and NPM regions in Figure 24C) to provide a conservative separation between PMs and NPMs and definitively determine that a model in that region is a PM or NPM. The minimum value for g_{NaP} for all simulations was chosen to be 0.5 nS. The other diagonal

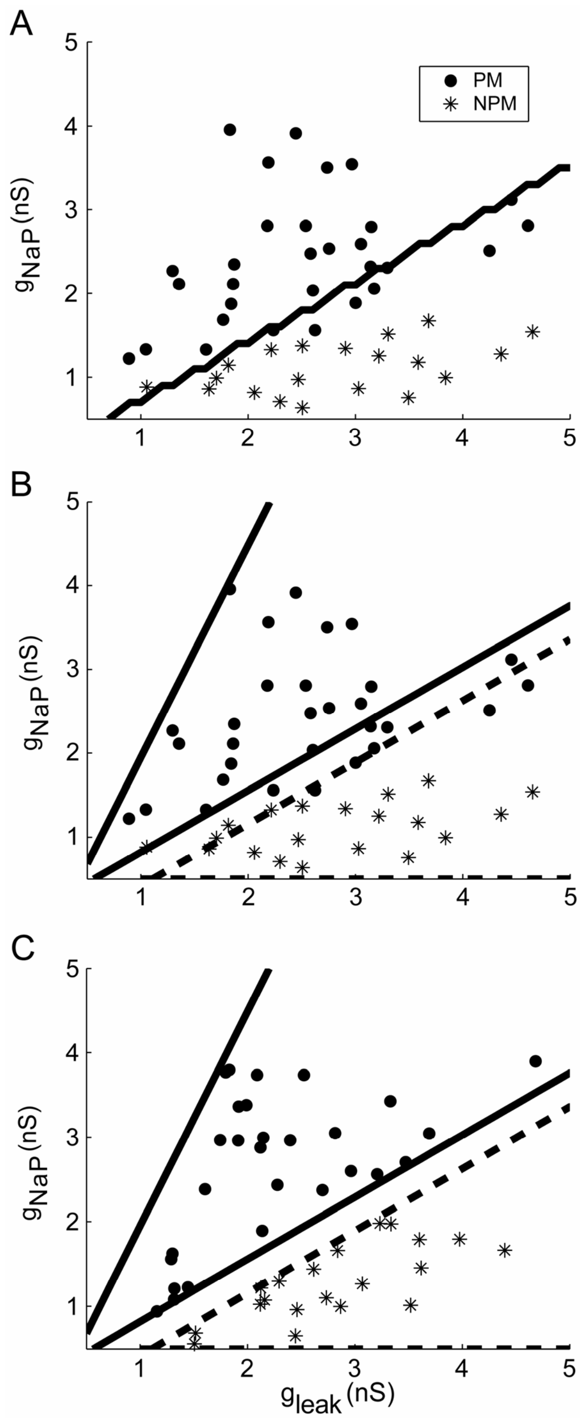

Figure 24. Comparing data space to model space. Pacemakers are circles (●), non-pacemakers are stars (*). Experimental data from Figure 22A is corrected by increasing g_{NaP} values by 25%. **A**: Corrected experimental data plotted with the model's PM/NPM boundary. **B** and **C**: Plots of data and random parameter distributions with the outline of the conservative PM region (denoted by solid lines) and NPM region (denoted by dashed lines) of model parameter space. In **B**, experimental data is plotted with the conservative model boundaries. Several data points fall outside of the conservative boundary allowed for model parameters. **C** illustrates sample randomly generated model parameter distribution with 30 PMs and 20 NPMs.

boundary at the upper edge of the PM space was set to keep the model inside its operating range. Figure 24B displays these conservative model boundaries plotted with the experimental data of Figure 22A. 74% of the data points are inside the conservative boundaries allowed for the model parameters.

4.1.3.3 Defining Random Distributions

As stated above, the network simulations will use values from a two-dimensional normal distribution in g_{NaP} and g_{Leak} for PMs and NPMs. When randomly choosing parameters to generate a PM model, the parameters must be verified to ensure that the model actually is a PM (likewise for NPMs). The parameters must also be tested to ensure that they are not outside of the operating range of the model. Thus, some of the values that are randomly chosen from the two-dimensional distribution must be discarded because they fall outside of these boundaries. Therefore, the values for mean and SD of the experimental data listed in Table 7 can not be used for the random number generator because the act of discarding and repicking from the normal distribution will result in a different mean and SD for the population. C++ simulations were run that selected 10,000 random sets of parameters to determine the actual mean and SD values after bounding the allowable parameter space. The simulation was then repeated for various nominal means and SDs until the actual mean and SD after discarding/repicking was similar to the mean and SD of the corrected data (Table 7). These trials were repeated 100,000 times and the best parameter distributions were determined by taking the minimum of the summed percent error between the computed mean/SD and the data mean/SD. Table 7 provides the optimal means and SDs for g_{NaP} and g_{Leak} whole distribution statistics that best match the experimental data.

Once initial mean/SD values for the normal distribution were chosen such that the calculated mean/SD after discarding/repicking closely matched the experimental data, we used these distributions to choose model parameters of PMs and NPMs for the network simulations. For example, Figure 24C provides a sample parameter distribution to be used for model simulations that includes 30 PMs and 20 NPMs. Although this data-mapping scheme is not perfect (26% of the corrected experimental data falls outside of the model's allowable range, Figure 24B), it does provide a model approximation of the variability of the experimental data.

4.1.4 Network Simulations

The network simulations consist of a population of 50 cells, of which there are K PMs and 50-K NPMs. It is important to note that the total number of cells in the network remains constant at 50 while K is varied from 0 to 50 in increments of 1 (i.e. only the percent of the population that are PMs or NPMs changes). For each K, the amount of excitatory drive, or g_{tonic}, is varied in 0.1 nS increments from 0 to 1.5 nS. Varying the amount of drive allows us to explore this voltage-dependent frequency control, as exhibited by the isolated pBC in slice preparations [1, 66]. Also, since the exact amount of excitatory synaptic coupling is unknown, the level of excitatory coupling is varied over physiological ranges for each simulation. Physiological range was determined by examining the synaptic current for various values of g_{syn} (see e.g. Figure 13 of [19]) and comparing it to values measured experimentally (see e.g. Figure 1 of [8]). The model of fast excitatory synaptic dynamics used is as previously specified in Butera et al. [19]. The results presented are from networks with all-to-all excitatory coupling. Similar results were obtained with sparsely connected networks (see below).

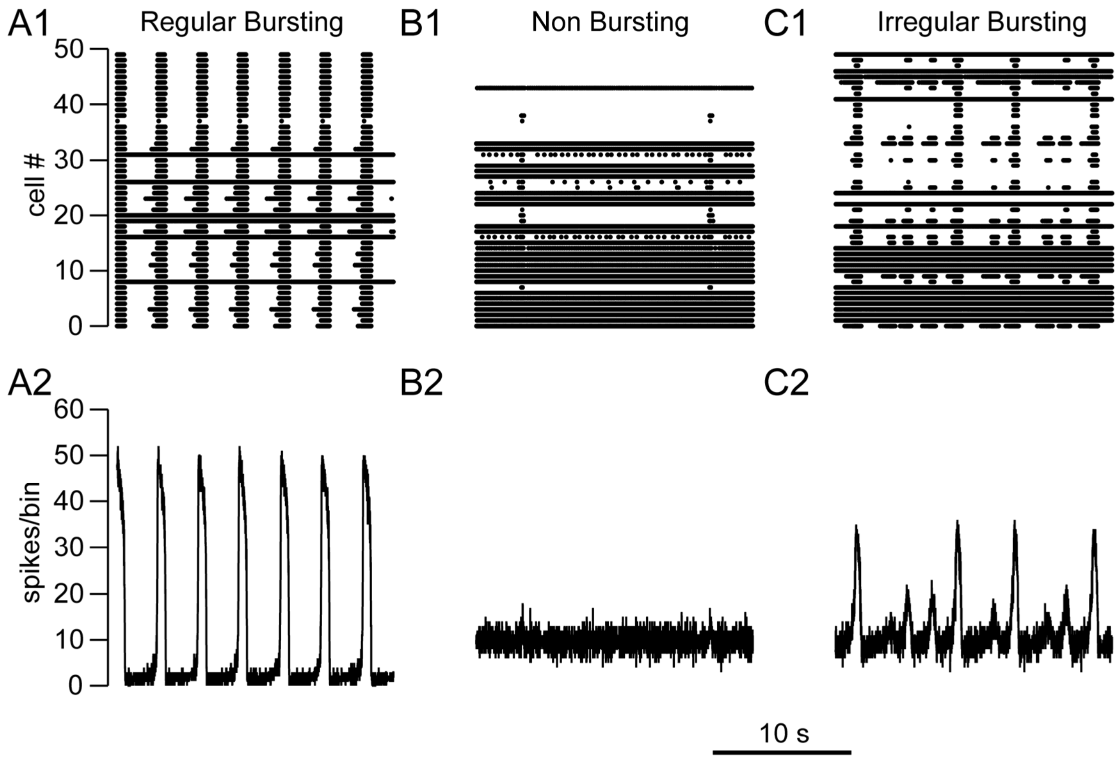

Figure 25. Network activity modes. **A1-C1**: raster plots. **A2-C2**: network activity, defined as histograms of spike times across the population (bin size = 10 ms). **A1-2**: Regular bursting network. Most cells are bursting. **B1-2**: Non bursting network. Most cells are silent or tonically firing. **C1-2**: Irregular bursting network. Burst period is highly variable.

Network simulations were run on Linux and Unix workstations using C code [19], and the results were analyzed using Perl scripts and MATLAB (Mathworks, Natick, MA). Network simulations were run for two minutes of simulation time with the first 30 seconds being ignored to allow startup transients to decay.

4.1.5 Data Analysis

An automated burst detection technique was implemented by generating a combined histogram of spike times from every cell in the network (Figure 25). The maximum and minimum amplitude of the histogram was calculated and the difference between those values was compared to a threshold. If the threshold was met, and if the amplitude of the histogram remained below 10% of the maximum amplitude for some minimum amount of time, then the output was defined as a burst. The values for amplitude threshold and minimum time below 10% of maximum amplitude were chosen by visual inspection of the histogram data. This method classifies the results illustrated in Figure 25A and C as bursting, but the network producing the pattern illustrated in Figure 25B is classified as a non-bursting network. For the results given in this manuscript, only "regular" bursting patterns were considered; therefore, the bursting patterns in Figure 25A and C were further analyzed. To determine if regular bursting patterns were present, the burst period (BP), burst duration (BD), and burst amplitude were measured. Before measuring these values, the data was smoothed using a 20-point moving average. After smoothing, the start of a burst was calculated using a rising phase threshold of 30% of the maximum amplitude and the end of the burst was calculated using a falling phase threshold of 10% of the maximum amplitude. The BD is the time between these two thresholds, the BP is the time between the rising phase of two subsequent bursts, and the burst amplitude is the maximum amplitude measured during the BD. If each of these values had a coefficient of variation among all bursts in a trace below 20%, and if more than two bursts were found in the 90 second time window, then the bursting was defined as regular and is hereafter referred to as network-wide bursting. Thus, the automated burst detection would define the bursts in Figure 25C as irregular because the BP has a coefficient of variation greater than 20%. The bursting pattern in Figure 25A meets all requirements for regular network-wide bursting. This analysis scheme was verified in preliminary simulations studies by inspection of raster plots of the

50 cell activity patterns to confirm the degree of cell synchrony between successive cycles. The values reported for the frequency of network-wide bursting were calculated using the inverse of the mean BP.

Once the existence of network-wide bursting has been established, input and output ranges are computed. Input range is defined as the size of parameter space where network-wide bursting occurs. The simulation data for input and output range are analyzed in some cases by grouping the number of PMs into bins where bin 0 is the special case when the network contains no PMs, bin 1 contains 1 to 5 PMs, bin 2 contains 6 to 10 PMs, etc. Input range is then defined as the percent of the maximum number of simulations inside a bin that produce network-wide bursting, i.e. the fraction of the range of g_{tonic} where network-wide bursting occurs. For example, bin 1 contains 5 values of PMs (from 1 to 5 PMs) and 16 values of g_{tonic} (from 0 nS to 1.5 nS in 0.1 nS increments) for each number of PMs giving 80 total simulations inside that bin. If network-wide bursting is found in only 4 of the 80 simulations (as is the case for bin 1 where g_{syn}=0.2 nS, see below), then the input range would be 4/80 or 5%. Output range is computed by subtracting the maximum frequency of network-wide bursting for a given number of PMs from the minimum frequency of network-wide bursting for the same number of PMs (as g_{tonic} is varied) and averaging this range across all PMs in that bin. Therefore, for a given number of PMs, if the network bursts with a maximum frequency of 0.75 Hz when g_{tonic}=0.9 nS and the network bursts with a minimum frequency of 0.25 Hz when g_{tonic}=0.1 nS, the output range is defined as 0.50 Hz for that number of PMs.

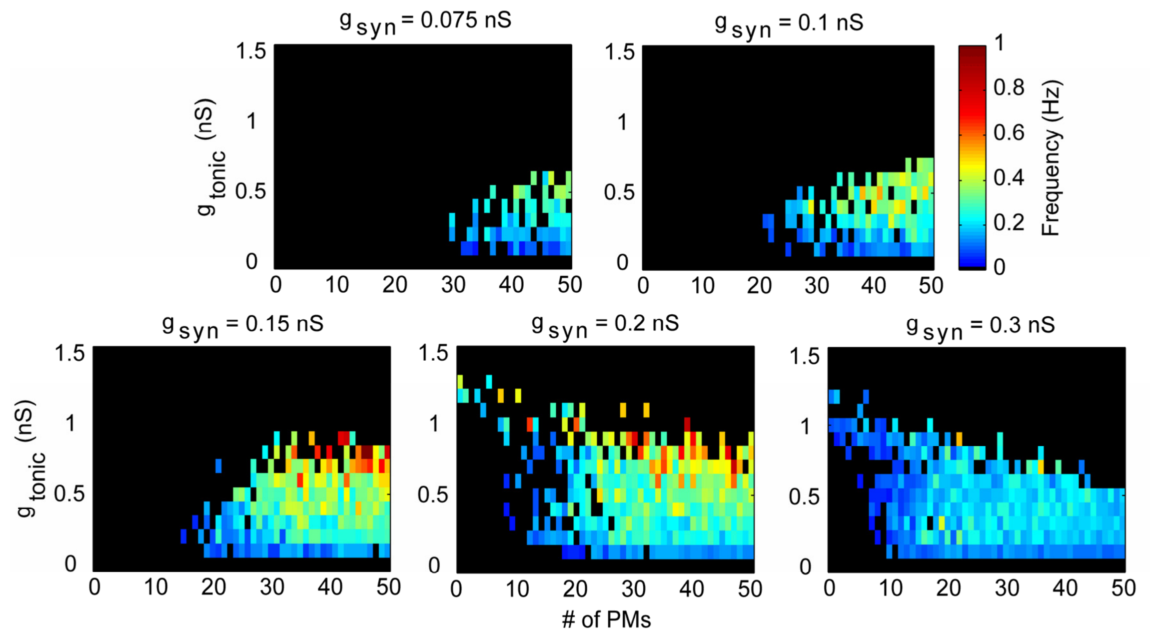

Figure 26. Results of varying number of PMs (x-axis), g_{tonic} (y-axis), and g_{syn} (from top left, 0.075, 0.1, from bottom left 0.15, 0.2, and 0.3 nS). Color indicates frequency of network wide-bursting. Black regions indicate the absence of network-wide bursting and could be either silence, a few cells bursting, irregular bursting, or tonic firing. Each point represents a distinct simulation with different randomly generated parameters.

4.2 Results

Figure 26 illustrates the existence and frequency of network-wide bursting as the number of PMs and excitatory drive (g_{tonic}) are varied for five values of excitatory synaptic coupling (g_{syn}). The color indicates the frequency of network-wide bursting; black regions indicate the absence of network-wide bursting. The simulations in the black region could produce a network containing neurons that are all or mostly silent, a network containing neurons that are all or mostly tonically firing, or a network that produces an irregular bursting pattern. Each point in Figure 26 is the result of a single simulation with a new randomly generated set of parameters. It is this independent parameter selection for each simulation that causes the "noise," or variability among adjacent points. Figures 27 to 29 further quantify the results shown in Figure 26, and

Figure 30 and Figure 31 illustrate the averaged results of multiple simulations using a single value for g_{syn}. Figure 32 provides a method of displaying our results that will allow a straightforward comparison to future experimental data.

4.2.1 Network-Wide Bursting

At lower levels of synaptic conductance (top panels, Figure 26), more PMs are required to generate network-wide bursting. At higher levels of synaptic conductance (bottom right panel, Figure 26), network-wide bursting is seen with fewer PMs, but the range of frequencies produced by the network is greatly reduced. Other levels of synaptic conductance (higher than 0.3 nS and lower than 0.075 nS) were explored, but did not result in significant amounts of network-wide bursting. Also, increased excitatory drive (g_{tonic} > 1.5 nS) did not produce network-wide bursting at any level of synaptic conductance or for any fraction of PMs. At these high levels of excitatory drive, only tonically firing activity within the network was seen. The results of Figure 26 also suggest that, for a fixed level of synaptic conductance and g_{tonic}, reducing the number of PMs, in general, reduces the frequency of network-wide bursting until the rhythm is eventually abolished.

4.2.2 Input Range and Output Range

Figure 27 is a plot of the input range for all values of g_{syn} as a function of K and levels of excitatory coupling. For the lower values of g_{syn} (0.075, 0.1, and 0.15 nS), the input range displays a generally increasing trend as the percent of PMs increases from 0 to 100% of the population, with the lowest levels of synaptic conductance failing to produce any network-wide bursting until more than 20 or 25 PMs are in the population

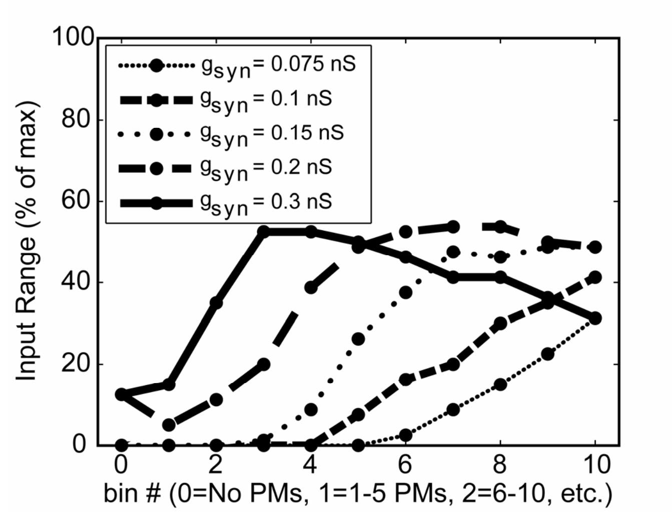

Figure 27. Input range for several values of g_{syn}. The input range is computed as the percent of the total number of simulations where network-wide rhythmic bursting occurs. X-axis is bin number where bin 0 is no PMs, bin 1 is 1 to 5 PMs, bin 2 is 6 to 10 PMs, etc.

(bin 5, g_{syn}=0.1 nS and bin 6, g_{syn}=0.075 nS). For the larger values of g_{syn} (0.2 and 0.3 nS), the input range increases as the number of PMs is initially increased, and then decreases slightly for higher percentages of PMs. Networks with g_{syn}=0.15 and 0.2 nS span the greatest range of input ranges (Figure 27).

Table 8 quantifies the input and output range for three cases: a network containing no PMs, a network where less than (or equal to) half of the population is made up of PMs, and a network where more than half of the population is made up of PMs. Only two of the five synaptic conductances explored produced network-wide bursting when no PMs are present in the network (Figure 27, bin zero). At g_{syn}=0.2 nS and 0.3 nS, network-wide bursting occurs with no PMs over 13% of the input range. The average input range for a network with 1-25 PMs at g_{syn}=0.2 nS and 0.3 nS is 25% and 41%, respectively. The average input range for a network with more than half of its population made up of PMs at g_{syn}=0.2 nS and 0.3 nS is 52% and 39%, respectively (Table 8). Thus,

Table 8. Input and output range. Average input and output range when the network contains no PMs, less than or equal to 50% PMs, and more than 50% PMs.

	Input Range			Output Range		
Synaptic Conductance	0 PMs	1-25 PMs	26-50 PMs	0 PMs	1-25 PMs	26-50 PMs
g_{syn}=0.075 nS	0	0	16%	0	0	0.11 Hz
g_{syn}=0.1 nS	0	2%	29%	0	0.01 Hz	0.24 Hz
g_{syn}=0.15 nS	0	7%	46%	0	0.03 Hz	0.43 Hz
g_{syn}=0.2 nS	13%	25%	52%	0.20 Hz	0.19 Hz	0.43 Hz
g_{syn}=0.3 nS	13%	41%	39%	0.04 Hz	0.13 Hz	0.12 Hz

for a given level of synaptic conductance, increasing the number of PMs in the network can more than triple the input range compared to a network containing no PMs.

Figure 28 illustrates the output range of the network for each level of synaptic conductance. The maximum and minimum frequencies for each number of PMs in a bin are given by closed and open circles, respectively. For most cases, the frequency range increases as the number of PMs is increased (Figure 28). Networks containing no PMs were able to burst (bottom center and right panels of Figure 28); however, the output range in this case is greatly reduced compared to simulations with larger percentages of PMs. At g_{syn}=0.2 nS and 0.3 nS, the output range with no PMs is 0.20 Hz and 0.04 Hz, respectively. The average output range when g_{syn}=0.2 nS with 1-25 PMs and with 26-50 PMs is 0.19 Hz and 0.43 Hz, respectively. When g_{syn}=0.3 nS, the average output range with 1-25 PMs and with 26-50 PMs is 0.13 Hz and 0.12 Hz, respectively (Table 8). The largest attainable output ranges for a given number of PMs when g_{syn}=0.15 nS and 0.2 nS are 0.88 Hz (with 46 PMs) and 0.71 Hz (with 41 PMs), respectively. These values are more than triple the largest output range obtained with no PMs in the network.

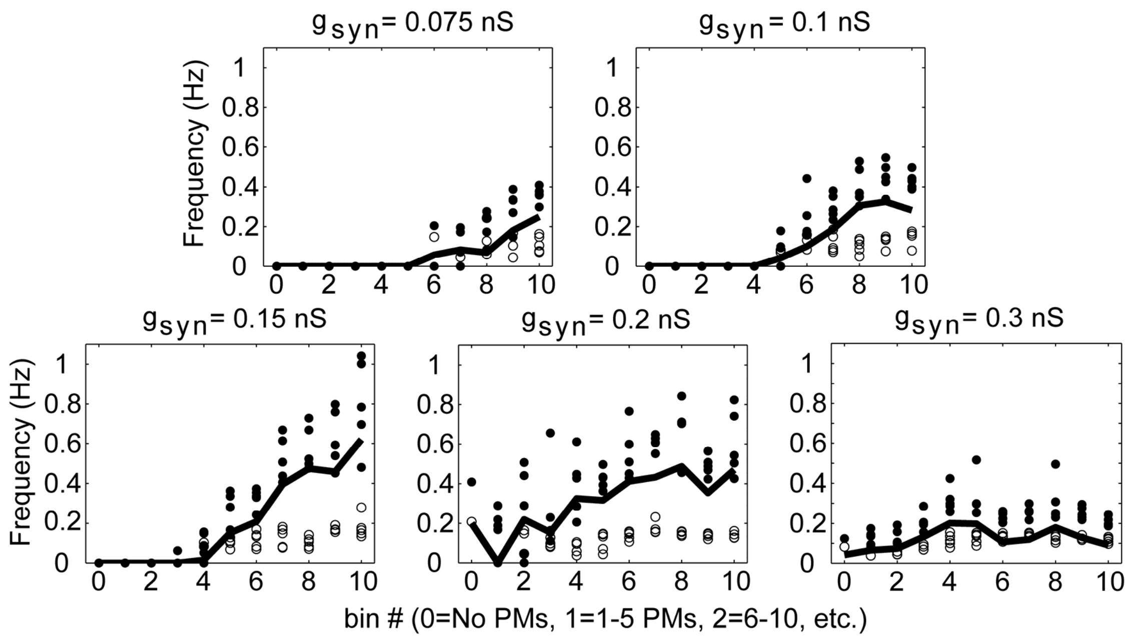

Figure 28. Output range for several values of g_{syn}. Results of varying number of PMs (x-axis is binned # of PMs), g_{tonic}, and g_{syn} (from top left, 0.075, 0.1, 0.15, 0.2, and 0.3 nS). Solid line is frequency range and is computed by subtracting the maximum frequency of network-wide bursting for a given number of PMs (closed circles) from the minimum (non-zero) frequency of network-wide bursting for the same number of PMs (open circles) and averaging this range across all PMs in that bin. X-axis is bin number where bin 0 is no PMs, bin 1 is 1 to 5 PMs, bin 2 is 6 to 10 PMs, etc., and y-axis is frequency.

4.2.3 Input/Output Range Tradeoffs

For a given level of g_{syn}, input range (Figure 27) and output range (Figure 28) were quantified and averaged across a range of K. Figure 29 plots input and output range vs. each other as K and g_{syn} are varied, allowing a compact visualization of how varying K and g_{syn} affect these metrics. Figure 29A is a plot of the input range vs. output range for different numbers of PMs. The plot of Figure 29A displays a clockwise trend as the level of synaptic conductance is increased for each number of PMs. In general, input and output range increase as the number of PMs is increased. There is an optimal value of g_{syn} for a given number of PMs that maximizes input and output range. Figure 29B is a plot of the input range vs. output range for different levels of synaptic conductance.

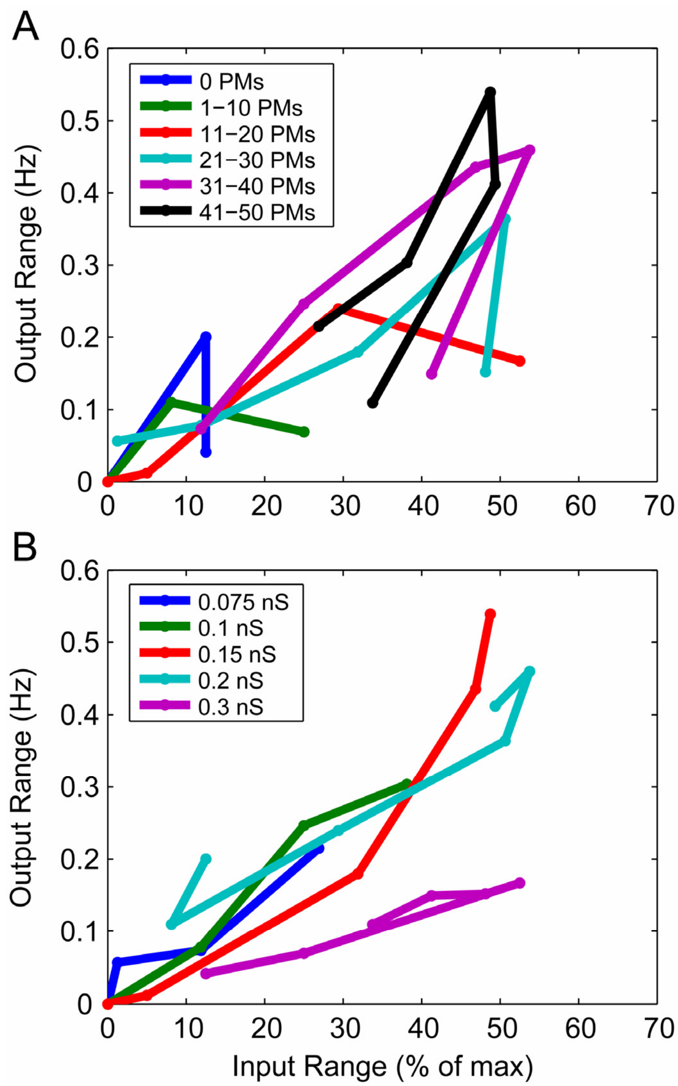

Figure 29. Input range vs. output range for different numbers of PMs (A) and for five different levels of synaptic coupling (B). A: The synaptic conductance increases from 0.075 up to 0.3 nS as each trace progresses clockwise. B: The number of PMs increases as each trace progresses from left to right. The number of PMs are grouped according to the legend of A (i.e. 0 PMs, 1-10 PMs, etc.).

Here, the number of PMs increases as the trace progresses from left to right. Figure 29B emphasizes the depressing effect on output range of increasing synaptic strength. Weaker coupling produces a smaller input range, and coupling too strongly produces a smaller output range. The moderate levels of synaptic conductance that provide the largest input and output ranges are found where g_{syn}=0.15 nS and 0.2 nS. At these moderate levels of synaptic conductance, the largest gain (or largest rate of change) in input and output range occurs when the number of PMs increases above 20-40% of the population (see, for example, the large increase between the second and third points where g_{syn}=0.2 nS in Figure 29B, see also Figure 26).

4.2.4 Multiple Simulations

Since the optimal synaptic conductance level was found to be between g_{syn}=0.15 nS and 0.2 nS, four additional simulations were run at both levels of synaptic conductance. This was to validate general trends just described and average over the variability of individually randomly generated simulations. The input and output range for each simulation is given in Figure 30, and the average of all five simulations is plotted as a bold line. The input range is fairly consistent among all simulations for g_{syn}=0.15 nS and 0.2 nS (Figure 30A,B). The output range for g_{syn}=0.2 nS is more variable (Figure 30D) but both display a clear upward trend as the number of PMs is increased (Figure 30C,D). Previously, the largest output range obtained for a network with no PMs was 0.20 Hz when g_{syn}=0.2 nS. However, none of the four additional simulations at g_{syn}=0.2 nS produced network-wide bursting at more than a single value of g_{tonic} with no PMs in the network. This reduces the average output range with no PMs in the network to 0.04 Hz.

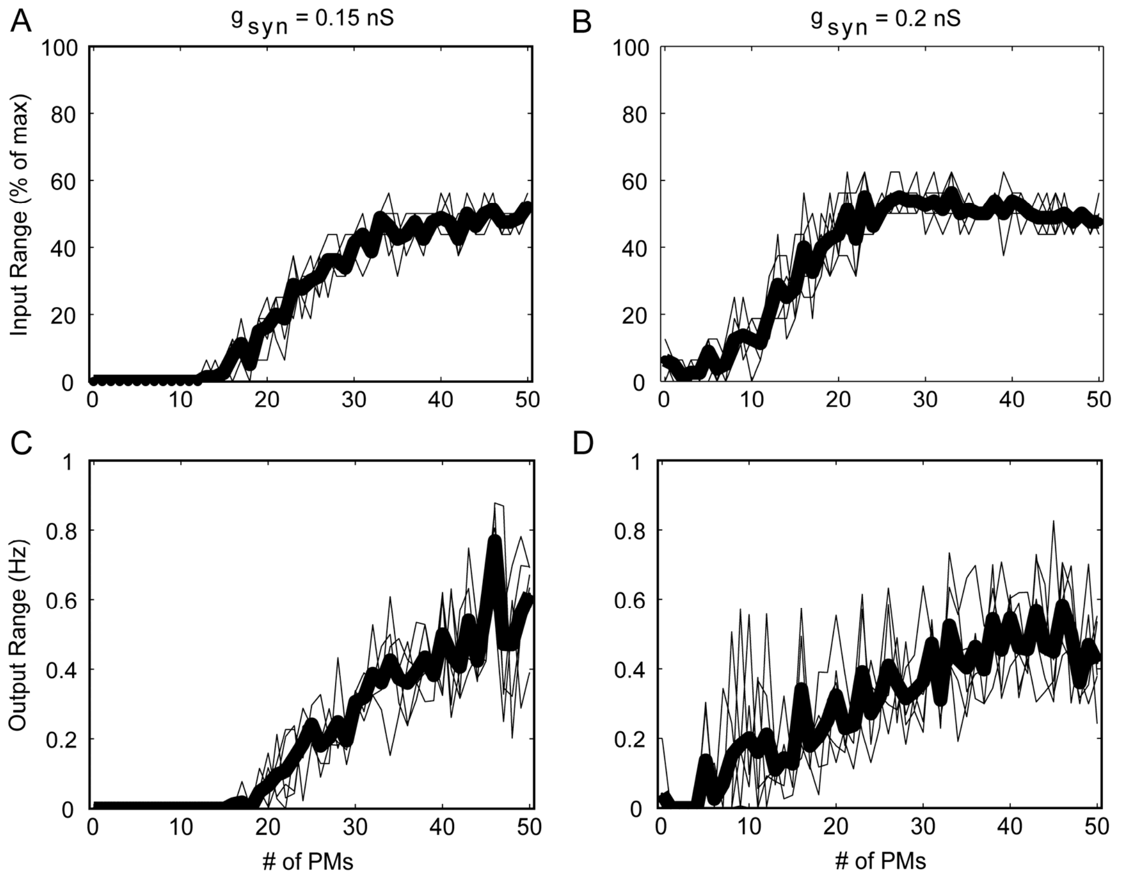

Figure 30. Input (A,B) and output (C,D) range of 5 simulations where g_{syn}=0.15 nS (A,C) and 0.2 nS (B,D). The bold line is the average of 5 runs.

Figure 31A displays the average results of varying g_{tonic} and number of PMs for all simulations with g_{syn}=0.15 nS and 0.2 nS. When computing the average, simulations that did not produce network-wide bursting were ignored (rather than including a zero frequency in this average). Averaging multiple runs removes much of the variability among adjacent points seen in the results from a single run (compare Figure 31A,B to bottom left and center panels of Figure 26). Figure 31C,D reveals the likelihood of choosing a random set of parameters that can produce network-wide bursting with a certain number of PMs in the population for a given level of excitatory drive. In Figure 31C,D, the (black and white) colorbar indicates in how many of the five simulations

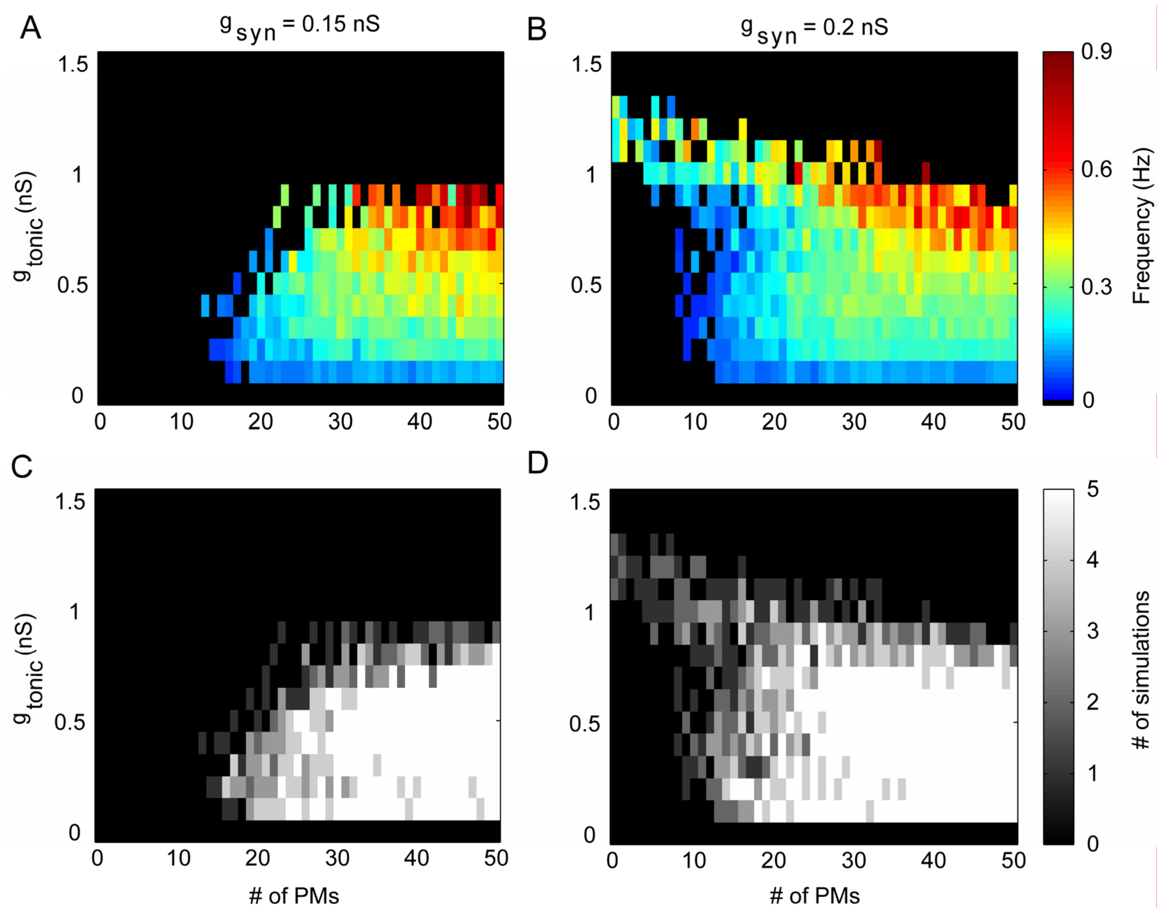

Figure 31. A,**B**: Average results of varying number of PMs (x-axis) and g_{tonic} (y-axis) for 5 simulations where g_{syn}=0.15 nS (**A**) and 0.2 nS (**B**). Individual simulations where no bursting was found were not included in the average. **C**,**D**: Likelihood of bursting in 5 simulations where g_{syn}=0.15 nS (**C**) and 0.2 nS (**D**). White region indicates bursting for all 5 simulations and black region indicates no bursting for any simulation.

network-wide bursting was measured. The white regions are where bursting occurs for all five simulations, and the black regions are where no network-wide bursting is recorded. Figure 31B,D illustrates that the network is able to burst with fewer numbers of PMs, and is also capable of producing a large range of frequencies with fewer PMs. However, the likelihood of producing network-wide bursting in this region is minimal (top left of Figure 31D). The network does produce bursting when few PMs are present, but it does not consistently produce bursting at the same points in parameter space. This is the cause of the variability seen in Figure 30D.

4.2.5 Sparsely Connected Networks

The simulations were repeated using a sparsely connected population and the results were compared to the all-to-all coupling simulations given above. For these simulations, the probability of connection was reduced to 10% (as an example of very sparse connectivity) and the level of synaptic conductance was increased so that the mean level of synaptic current provided to each cell remained approximately the same. For the sparsely connected networks, we explored three values of synaptic conductance, g_{syn}=1.0, 1.5, and 2.0 nS, that roughly correspond to g_{syn}=0.1, 0.15, and 0.2 nS using the all-to-all connectivity presented above. The results of the simulations employing the sparsely connected networks (not shown) are completely consistent with all results employing all-to-all connectivity. Both input and output ranges of the sparsely connected networks increased as the number of PMs increased in a similar fashion to the corresponding levels of synaptic conductance with all-to-all coupling. Also, the magnitudes of the ranges of frequencies measured were similar.

4.3 Discussion

These simulations were performed to investigate the functional significance of PM cells in the pBC excitatory network. The simulations employ two types of heterogeneity: cell-type heterogeneity (PMs and NPMs) and parameter heterogeneity within a given cell-type that is based on experimental data. Before running the data-based simulations presented here, we performed several simulations (not shown) using less heterogeneous parameter distributions: a semi-homogeneous parameter space (g_{Leak} was kept constant for all cells; g_{NaP} was constant within each subpopulation of PMs or NPMs) and a one-dimensional heterogeneous parameter space (g_{Leak} was kept constant for all cells whether PM or NPM; mean g_{NaP} was different for PMs and NPMs and varied with a SD of +/- 10%, and then +/- 30%). The semi-homogeneous simulations produced networks with reduced input and output ranges compared to networks with more heterogeneous parameter distributions, which might be expected based on previous studies examining the role of heterogeneity in this network [19]. Although there were minor quantitative differences, the simulations using less heterogeneous and less data-based parameter distributions, as well as the simulations using sparsely connected networks provide results that are qualitatively similar to the results of the data-based simulations presented here. The major conclusion of this study was reiterated in every simulation performed, that is, pacemakers can increase the input and output range of a bursting network.

4.3.1 Controllability

The absolute values for input range are not meaningful because the percentages calculated are a function of the size of parameter space chosen (g_{tonic} varies from 0 nS to 1.5 nS in 0.1 nS increments). If g_{tonic} were allowed to increase up to 2.0 nS, then all calculated percentages would be reduced. However, the relative differences between the input ranges for different numbers of PMs and for different levels of g_{syn} are important. The input ranges given in Figure 27 and Table 8 reveal that network-wide bursting is easier to obtain when the fraction of the network population made up of PMs is increased. Like input range, output range shows a generally increasing trend as the number of PMs is increased. This highlights an important difference between the controllability potential of synaptic conductance vs. the number of PMs in a network. Increasing g_{syn} can increase input range but at the cost of output range. Alternatively, increasing the number of PMs in the network can increase both input range and output range.

Comparing input and output range for several values of g_{syn} reveals an optimal synaptic conductance near g_{syn}=0.15 nS and 0.2 nS. Therefore, we ran multiple simulations at these levels of synaptic conductance. Examining the results of these simulations revealed that large output ranges were possible with few PMs at g_{syn}=0.2 nS, but the output range in this region was highly variable due to the inability to unfailingly generate networks capable of producing network-wide bursting. In general, the network input-output range increased as the percentage of PMs increased under these optimal synaptic coupling conditions.

The reported estimates for the number of PMs in the pBC vary from 5% to ~50% for different *in vitro* slice preparations and recording conditions [7-9, 11, 13]. Since the PM or NPM state of a pBC cell is modulatable [32, 46], it is possible that the number of PMs in this network is modulated in order to meet particular dynamic range requirements. Indeed, our current and original model analyses indicate that any neuromodulatory conditions that change the g_{NaP}/g_{Leak} ratios within the network can potentially change the relative numbers of PMs and NPMs and hence the network's dynamic performance. Thus, the varying estimates under different recording conditions may in part reflect the modulated state of the pBC. With optimal values of g_{syn} in our simulations, the biggest increase in dynamic range occurs when the number of PMs increases above ~20% of the population (see Figure 29 - Figure 31). Future studies will use reduced order models to investigate the mechanism and significance of this threshold-like effect of the number of PMs on network dynamics.

4.3.2 Limitations of the Model

These simulations employ a minimal model of pBC cells that lack some voltage-gated ionic currents known to exist in these cells, such as the LVA or HVA calcium channels [51]. This minimality undoubtedly plays a role in the inability of the model to perfectly match the experimental data. In constructing our network models, we sought to rigorously incorporate conductance density distributions, their variability, and voltage dependencies that are consistent with the experimental data. An important model parameter that has not yet been directly verified by measurements, however, is the kinetics for the voltage-dependent slow inactivation of NaP incorporated in the model. This parameter controls the dynamics of the single-neuron rhythmic bursting cycle and synchronized rhythmic bursting at the population level.

Since model parameters were chosen from a two-dimensional heterogeneous parameter space, ideally, multiple simulations should be run so that any variability among simulations can be averaged out. This is computationally time consuming. Figure 26 contains almost 4000 simulations, where each simulation is a network of 50 cells. However, our results indicate that more simulations are not necessary. When multiple simulations were run for a single value of synaptic conductance, all simulations displayed similar trends. Also, as stated above, all simulations using less heterogeneous parameter distributions and sparsely connected networks provided results consistent with the results presented in this study.

The simulations that produced network-wide bursting with few or no PMs typically provided minimal output ranges. Although some simulations with few PMs were able to produce large output ranges (Figure 30D), the likelihood of producing network-wide bursting here was low (Figure 31D). Attempts were made to choose data based parameters for the simulations. However, the limitations of the minimal model and of the parameter selection technique could be the source of the inability to unfailingly produce robust network-wide bursting with fewer numbers of PMs in the population.

Whether or not the NaP current provides the primary mechanism for burst termination and regenerative reactivation of the network in *in vitro* slice preparations remains to be clearly resolved. Published investigations of this mechanism appear to greatly depend on the experimental preparation (i.e. thin vs. thick slices *in vitro* vs. the more intact network *in situ*) [7, 9, 12, 14, 24]. Our results (Figure 26) suggest that at least for preparations with a relatively isolated pBC network (e.g. thin *in vitro* slice preparations) and for a fixed level of synaptic conductance, reducing g_{NaP} and hence the number of PMs, in general, reduces the frequency of network-wide bursting until the rhythm is eventually abolished. This agrees with some experimental results where g_{NaP} was reduced pharmacologically by riluzole or low concentrations of TTX, presumably reducing g_{NaP}/g_{Leak} ratios to parameter space regions with few PMs [24, 52]. Our model does not include the cadmium-sensitive bursters found in the pBC of slice preparations from mice [7, 9, 10, 12], but not rats [9]. Further modeling and simulations are required to determine the effects of adding these pacemakers to our network models. At present, little is known about the biophysical parameters of the CAN current, and these cells may [10] or may not [9] provide voltage-dependent control of PM oscillation frequency, which would impart a very different contribution to the input-output range of the network. Indeed, a unique property of NaP-dependent mechanisms may be the enabling of a broad range of tunable network oscillation frequencies, which is inherent in the voltage-dependent properties of this conductance mechanism. In considering the functional significance of any type of PM mechanism, the issue of frequency control may be fundamental. That is, it is not simply the capability of a particular cellular pacemaker mechanism when coupled with excitatory synaptic interactions to organize a network-wide rhythm in the pBC, but it is the inherent ability of any mechanism to allow functionally for frequency control over a wide dynamic range. This control is a prominent feature of experimental data, at least for the isolated pBC in slices *in vitro* under conditions where tonic drive is varied (e.g. [66]).

4.3.3 Rhythmic Networks

While we have analyzed dynamics of excitatory networks incorporating bursting cells to investigate rhythm generation mechanisms in the pBC, our results would pertain to rhythmogenesis in the isolated pBC as in slice preparations *in vitro*, or under hypoxic conditions in perfused brainstem preparations *in situ* [14], where there is evidence for NaP-dependent mechanisms. As we have originally pointed out [39], when the pBC is embedded in the brainstem respiratory network in more intact states of the system, as *in vivo*, phasic (and possibly tonic) inhibitory inputs to the pBC become important for dynamically regulating the evolution/termination of pBC inspiratory activity [113]. We have proposed [39] for example, that network-based phasic inhibition contributes importantly to the termination of pBC network-wide bursting in the intact system, as opposed to termination solely by the slow inactivation kinetics of NaP and interactions of

NaP and leak currents. Thus it remains an important theoretical and experimental problem to understand rhythm generation when inhibitory network mechanisms are overlaid on the excitatory network interactions that we have analyzed here.

Although our model is based on intrinsic bursting cells in the pBC, this study is representative of a particular class of rhythmic bursting networks – those where the connectivity is predominantly mediated by excitatory synapses. Examples include rhythmic bursting in transverse brainstem slices [1, 13], rhythmic activity in disinhibited embryonic spinal cords [114, 115], rhythmic activity in disinhibited medial septum and diagonal band complex [116], and 7-14 Hz oscillations in motor cortex [117]. In such networks, the synaptic excitation is responsible for the coordination and spread of activity through the network at the start of an episode of activity; in other cases such excitation may play a key role in the initiation of a burst of activity as well. In all these cases, burst episode initiation is attributed to some combination of intrinsic cellular properties and/or recurrent excitatory coupling. Burst termination can be due to the slower kinetics of ionic currents intrinsic to the component neurons (e.g. this model) or the slower kinetics associated with synaptic depression [118].

4.3.4 Model Predictions

To date, we are unaware of any experimental studies that quantify dynamic range under conditions that putatively alter the number of PMs. Based on the simulation results, we expect both the input and output range of the network would be reduced as the fraction of PMs in the network is reduced. Likewise, if the conductance density of NaP channels is augmented, then we predict that neurons that were previously NPMs would become PMs and would produce an increased dynamic range. Some have claimed [9, 38] and our modeling studies have shown that network-wide bursting is possible after sufficiently reducing NaP such that no PM activity is seen in the network [19]. However, our simulations suggest that under these conditions the dynamic range of the network is greatly reduced. Substance P has been shown to reactivate network-wide bursting after ostensibly blocking all PMs [9, 12]. Even if this reactivation is caused by the apparent ability of substance P to restore PM activity to some cells where PM activity was previously abolished [12], based on our simulation results, we would still expect the dynamic range of the network to be reduced under these conditions. Experiments to test the model predictions would involve measuring the range of frequencies produced by the network while varying, for example, the level of tonic activation of AMPA receptors or tonic excitation with extracellular potassium concentration under control conditions and when g_{NaP} and thus PM activity has been attenuated by application of riluzole or small amounts of TTX. Our model analog to the experimental figure this would produce is given in Figure 32 where we plot frequency vs. g_{tonic} for different numbers of PMs. Experimentally varying the level of AMPA receptor activation or extracellular potassium within the pBC is qualitatively equivalent to varying E_K [24, 66], E_L [18], or g_{tonic} [19] in the model. Figure 32 can be compared to future experimental tests of these model predictions.

Hypoxia increases NaP conductance density [119-121], and recent studies have shown the importance of NaP-dependent bursting cells during hypoxia [12, 14]. If hypoxia increases the number of PMs in the network, this would cause a shift in parameter space to a region capable of producing higher frequency rhythms. This is a potential mechanism for obtaining the initial increase in burst frequency observed during

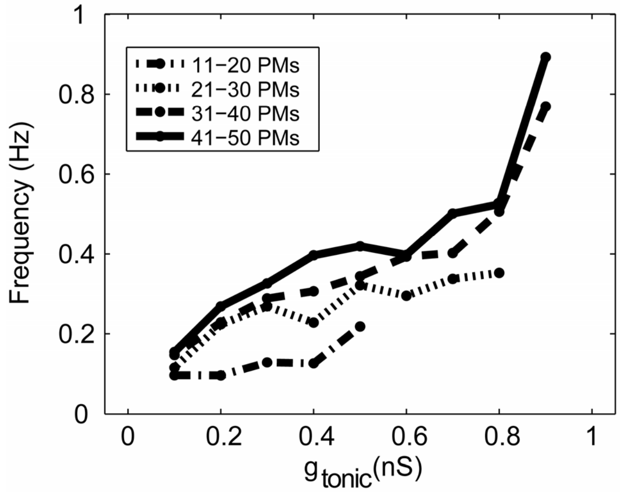

Figure 32. Frequency vs. g_{tonic} for different numbers of PMs when g_{syn}=0.15 nS. Reducing the number of PMs reduces both the input range and the output range of the network. No bursting is produced for 0 PMs or 1-10 PMs.

hypoxia [12, 41, 122]. Again, the dynamic range of the network could be examined at different levels of pBC hypoxia. In general such comparisons under any experimental conditions that are found to either selectively augment g_{NaP} or augment g_{NaP}/g_{Leak} ratios to increase the number of PMs would be instructive.

4.3.5 Conclusions

Although the significance and abundance of PMs in the pBC are not completely understood, the existence of these cells is not questioned. We used modeling studies to quantitatively explore the role that one of the main types of PMs (i.e. NaP-dependent) found in the pBC plays in this bursting network. Networks containing no PMs were able to produce regular, synchronous network-wide bursting (albeit with a low probability of bursting, as well as a low input and output range), demonstrating that PMs are not critical for rhythm generation provided excitatory synaptic coupling strength is high. Thus, the NaP current can provide not only a mechanism for rhythmic bursting of individual PMs, but also a mechanism for synchronized rhythmic bursting and its termination at the network level. However, our modeling studies suggest that including PMs in the network allows the input and output range to more than triple compared to networks with no PMs. Indeed, the fraction of PMs greatly affects the controllability of the rhythm. Unlike synaptic coupling which requires a trade-off between input range and output range, increasing the number of PMs can increase both the input and output range of the network. Additional experimental tests as suggested by our results will be required to either confirm or refute our model prediction that PMs increase the robustness of rhythm generation.

CHAPTER 5: IMPROVED PRE-BOTZINGER COMPLEX CELL MODEL

In this chapter, we will improve the pBC model used in the previous chapter by including some of the ionic currents now known to exist in these cells. We will use the improved model to explore the role of these additional ion channels in shaping burst dynamics. The model developed in this chapter, as well as the HM model developed in previous chapters will provide the individual component models for future network models of the transverse slice.

We have developed an improved single-compartment, electrophysiological, pBC cell model. The improved pBC model builds on the minimal model of Butera et al. [18, 19] used in the previous chapter. Although the original model contains the mechanism for burst generation, it is still an overly simplistic model and fails to include many of the ionic currents now known to exist in pBC cells such as the low-voltage-activated (LVA) and high-voltage-activated (HVA) calcium currents [15, 51], the hyperpolarization-activated cationic current [16, 123], and the fast transient potassium current [17]. Our results indicate including these additional currents extends the bursting capabilities of these cells. Our results also reveal how various ionic currents differentially contribute to burst dynamics.

5.1 Methods

The currents used in the improved pBC model are described according to the methods already discussed in APPENDIX C and Sec. 2.1.2; therefore, the description will not be repeated here. Detailed equations and parameters describing each current of the

Table 9. Initial conditions for improved pBC model.

$V(0) = -60.86$ mV
$h(0) = 0.787$
$n(0) = 0$
$m_L(0) = 0.003$
$h_L(0) = 0.834$
$m_{HVA}(0) = 0.003$
$m_T(0) = 0.317$
$h_T(0) = 0.023$
$m_A(0) = 0.252$
$h_A(0) = 0.001$
$m_H(0) = 0.080$

Table 10. Parameters values for improved pBC model.

$\overline{g}_{Na} = 28.0$ nS	$\overline{g}_H = 2.0$ nS
$\overline{g}_{NaP} = 2.8$ nS	$E_{Na} = 50$ mV
$\overline{g}_K = 18.0$ nS	$E_K = -85$ mV
$\overline{g}_{KLK} = 1.8$ nS	$E_{KLK} = -75$ mV
$\overline{g}_{NSLK} = 0.6$ nS	$E_{NSLK} = -30$ mV
$\overline{g}_T = 2.0$ nS	$E_{Ca} = 40$ mV
$\overline{g}_{HVA} = 0.5$ nS	$E_H = -40$ mV
$\overline{g}_L = 2.0$ nS	$C_m = 21$ pF
$\overline{g}_A = 2.5$ nS	

improved pBC model are listed in APPENDIX D. All initial conditions and other model parameters are listed in Table 9 and Table 10, respectively.

5.2 Model Development

The improved pBC model builds on the minimal model of Butera et al. [18, 19] by incorporating additional ionic currents now known to exist in the pBC. The model formulation utilizes voltage-clamp data from pBC cells not available when the model was originally created [15, 16, 51]. The original minimal pBC model includes four channels: the fast sodium, delayed rectifier potassium, and leak channels that cause the action potential, as well as a (slowly inactivating) persistent sodium channel responsible for bursting ([18]; see also APPENDIX C). Five additional currents are included in the improved model: an LVA calcium current, a slowly inactivating HVA current, a non-inactivating HVA current, a fast transient potassium current, and a hyperpolarization activated cationic current. A detailed description of the basis for each of these currents is given below. Figure 33 illustrates the gating characteristics of all currents in the model.

5.2.1 Spiking Currents

The currents responsible for generating the action potential in the original and improved pBC model are the fast sodium (I_{Na}) and delayed rectifier potassium (I_K) currents. Descriptions of these currents are taken directly from the original model of Butera et al. [18]. As described in Butera et al. [18], these currents are a simplified version of the Hodgkin-Huxley formulation [21]. The simplifications are as follows: the activation variable, *m*, is assumed to activate fast enough that it can be considered to be instantaneous , and the behavior of the *h* variable is assumed to be similar enough to the n variable that it can be approximated by $h = 1 - n$ [124, 125].

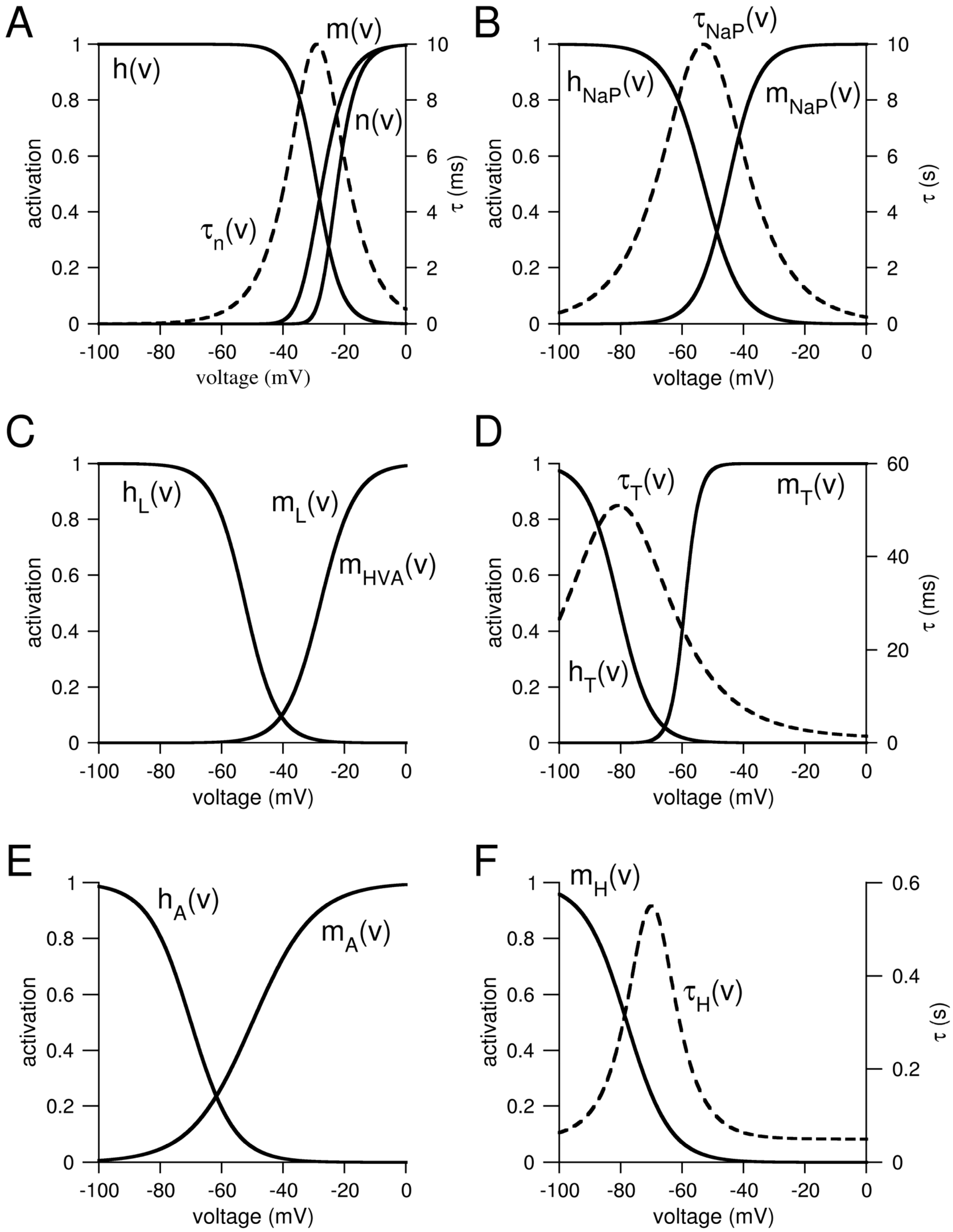

Figure 33. Gating characteristics of voltage-dependent currents in the improved pBC model. Only time constants with voltage-dependent characteristics are included (dashed lines). **A**: Spiking currents. I_{Na} and I_K. $h = 1\text{-}n$. **B**: Persistent sodium current. I_{NaP}. **C**: HVA calcium currents. I_L and I_{HVA}. m_L and m_{HVA} curves are identical. **D**: LVA calcium current. I_T. **E**: Fast transient potassium current. I_A. **F**: Hyperpolarization activated cationic current. I_H.

5.2.2 Persistent Sodium Current

Butera et al. [18] was the first to propose the persistent sodium (NaP) current as a bursting mechanism for pBC cells based on pharmacological/physiological experiments combined with arguments about the dynamics of bursting and subsequent simulations. This prediction was later verified experimentally [8, 10, 66]. The description of the NaP current (I_{NaP}) used in the improved pBC model is taken from Butera et al. [18] and includes the modifications made in Sec. 4.1.2 (i.e. more hyperpolarized (in)activation values and a modified slope factor). The time constant of inactivation for the NaP current is much larger in the pBC model than the time constant used in the HM model of Chapter 2. The inactivation dynamics for the NaP current (h_{NaP}) have not yet been described in pBC cells; therefore, the NaP inactivation parameters of the pBC cell model were chosen to replicate the dynamics of physiological experiments.

5.2.3 Calcium Currents

The pBC also contains LVA and HVA calcium currents [15, 51, 126-128]. The LVA, or T-type, current (I_T) activates at lower voltages and quickly inactivates. In the improved model we subdivided the HVA currents into two components: a slowly inactivating, or L-type, current (I_L), and a non-inactivating current (I_{HVA}). The voltage-clamp data of Elsen and Ramirez [15, 51] was used to determine the (in)activation and time constant parameters for the LVA and HVA currents. The inactivation time constant of the L-type current is similar to the values reported by Mironov and Richter [127, 128].

5.2.4 Fast Transient Potassium Current

The presence of a fast transient potassium current (I_A) is suggested by the results of Rekling et al. [17] where some cells exhibit delayed excitation in response to a hyperpolarizing prepulse. Since voltage clamp data is not yet available for A currents in pBC cells, a generic model of vertebrate A currents was implemented in the improved pBC model [129].

5.2.5 Hyperpolarization Activated Current

The role of the H current in pBC cells is unresolved. Mironov et al. [16] report no contribution of I_H to rhythm generation. However, Thoby-Brisson et al. [123] report an important role of I_H in modulating respiratory frequency. Including I_H in the improved pBC model could shed light on the potential role of this current in respiratory rhythm generation. The voltage-clamp data of Mironov et al. [16] was used to set the parameters of the H current in the improved pBC model.

5.2.6 Passive Properties

The leak conductance for the improved pBC model was subdivided into two components: a potassium leak current (I_{KLK}) and a non-specific leak current (I_{NSLK}) with reversal potentials of -30 mV and -70 mV, respectively (J.C. Smith, personal communication). Separating the leak into two components allows us to more accurately model the effects of increasing the external potassium concentration, a common method of experimentally increasing excitability [1, 66]. The membrane capacitance of the improved pBC model is the same as the original model (21 pF), and resting input impedance for the improved model is near 400 MΩ. Both of these values are within the range of values reported by Del Negro et al. [8].

5.3 Results

The significance of including additional currents to the original model is explored. First we will illustrate the activity of each current during a burst. Then we will consider how the inclusion of additional currents affects the range of bursting characteristics (i.e. burst period and burst duration). Finally we will examine how specific ionic currents can be used to control different aspects of these bursting measures.

Figure 34 illustrates the oscillatory activity of the improved pBC model as E_{KLK} is increased (modeling the effect of increasing the extracellular potassium concentration). This activity is similar to that of the original model of Butera et al. (see Figure 4 of [18]) and the experimental data [1, 8, 66]. As the level of excitation is increased, the model progresses from silence, to bursting, to beating (Figure 34). Burst duration is measured from the peak of the first spike to the peak of the final spike inside a burst. Burst period is measured from the peak of the first spike in a burst to the peak of the first spike in a subsequent burst. As seen in Figure 34, burst period and burst duration decrease as the level of excitation is increased.

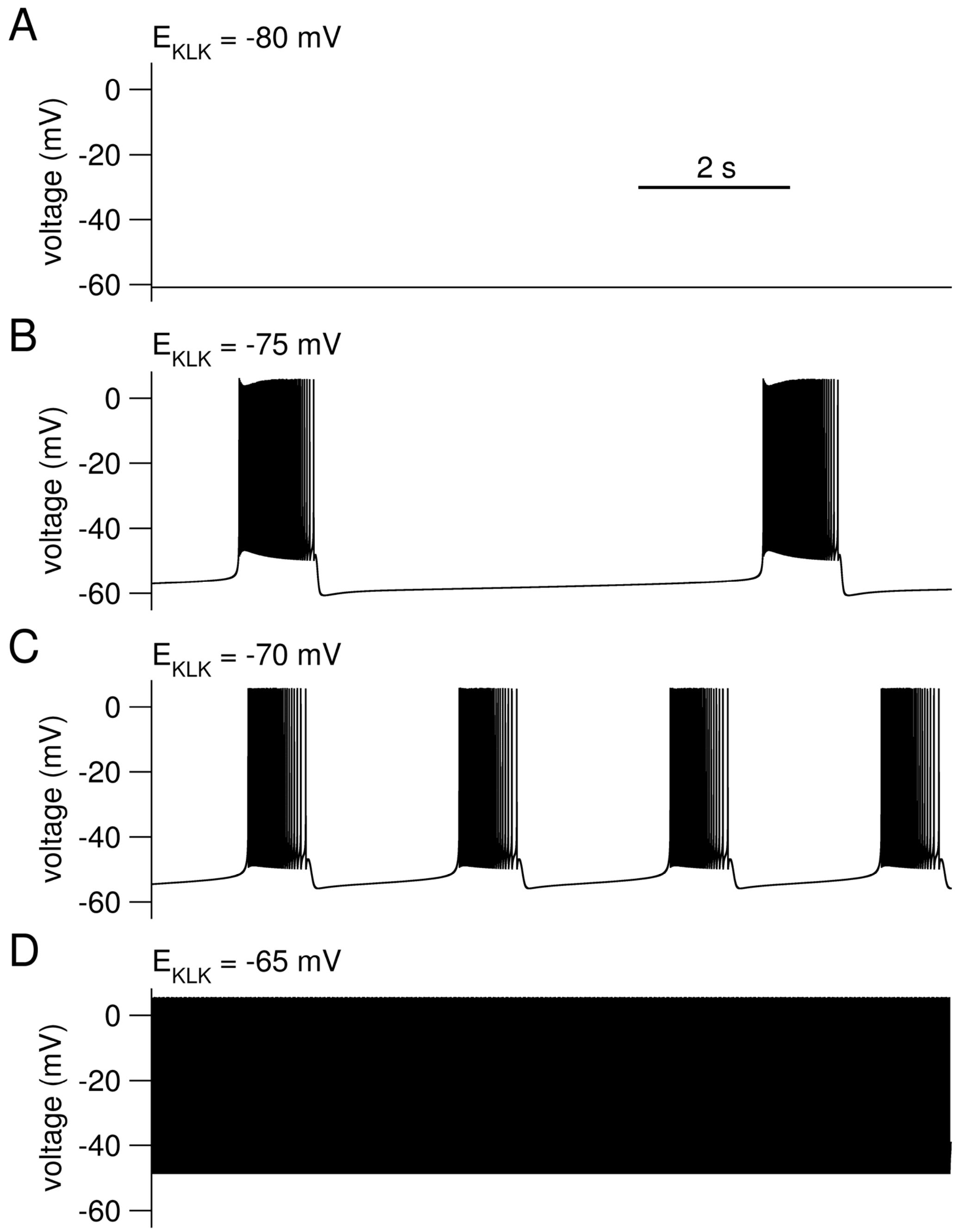

Figure 34. Oscillatory behavior of improved pBC model. Model progresses from silence to bursting to beating as E_{KLK} is increased. **A**: E_{KLK} = -80 mV, model is silent. **B**: E_{KLK} = -75 mV, model is bursting. **C**: E_{KLK} = -70 mV, model is bursting. Burst duration and burst period are reduced compared to bursting activity in **B**. **D**: E_{KLK} = -65 mV, model is tonically firing.

5.3.1 Model Currents

Figure 35 illustrates the behavior of each current in the improved pBC model during a burst. The activity of each current is described below.

5.3.1.1 Spiking Currents

The fast sodium and delayed rectifier potassium currents are responsible for the depolarization and repolarization of the action potential (Figure 35B). The large magnitude of I_{Na} is caused by the instantaneous activation implemented as part of the model simplification. Setting the maximum conductance of the fast sodium current to zero completely eliminates the intraburst spiking activity, but does not affect the underlying oscillations (similar to Figure 10 of Butera et al. [18]).

5.3.1.2 Persistent Sodium Current

As with the original model, the persistent sodium current (Figure 35C) is the mechanism that enables bursting in the improved model. The subthreshold activation of I_{NaP} is responsible for initiating the burst, and the slow inactivation of I_{NaP} is responsible for terminating the burst. As seen in Figure 35C, I_{NaP} is increasingly activated during the interburst interval until, when I_{NaP} becomes large enough, action potential firing and subsequent bursting activity is initiated. A plot of the I_{NaP} inactivation variable, *h*, during the bursting cycle is illustrated in Figure 36. As *h* is increasingly inactivated, the cell eventually does not receive enough inward current to continue firing action potentials and the burst is terminated. A more detailed description of the mechanism for mode transitions is given in Butera et al. (see Figure 9 of [18]).

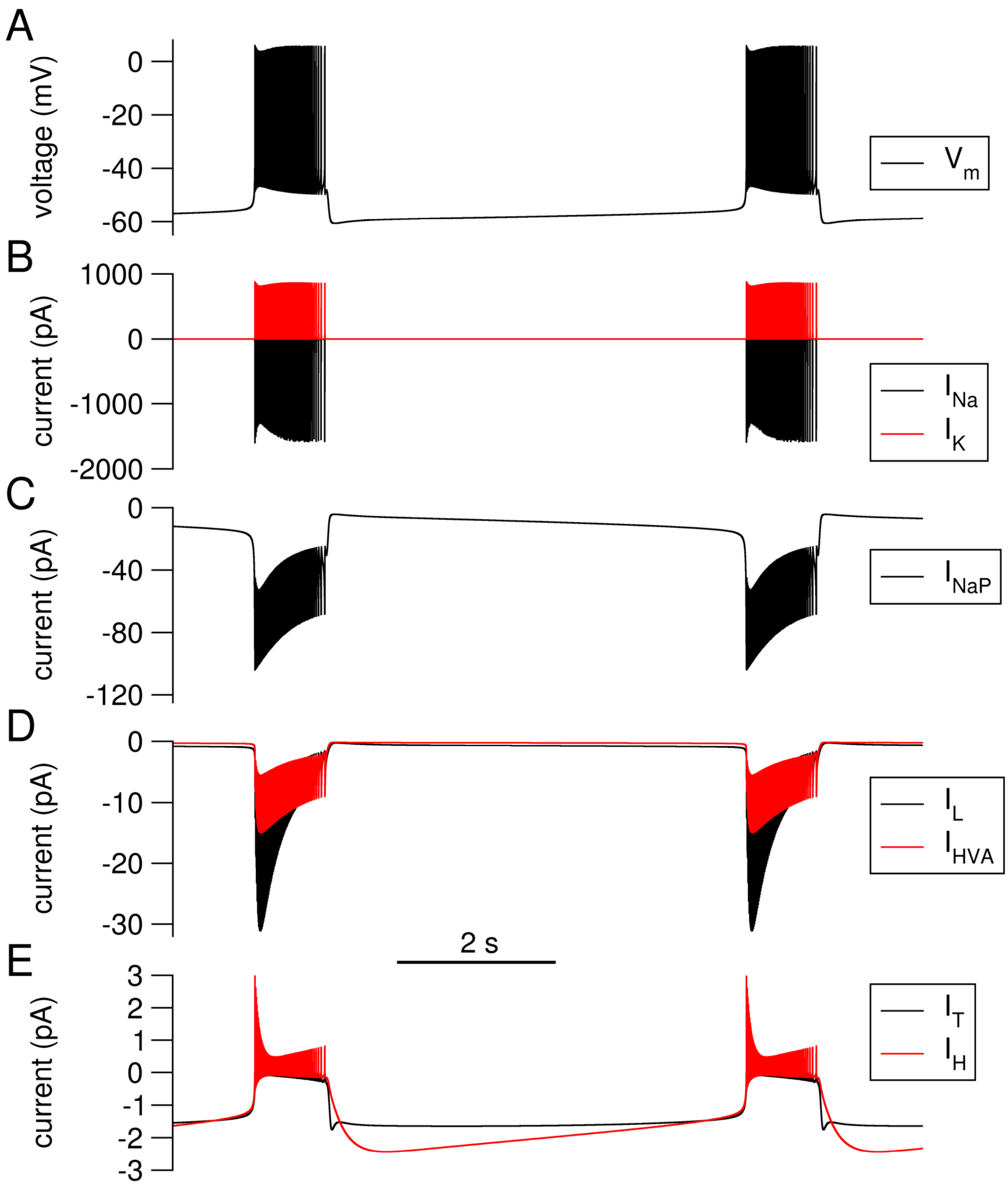

Figure 35. Model currents during a burst. **A**: Membrane voltage when E_{KLK} = -75 mV. **B**: Spiking currents. **C**: The persistent sodium current is responsible for bursting. **D**: Two components of the HVA calcium current. **E**: LVA calcium current and H current.

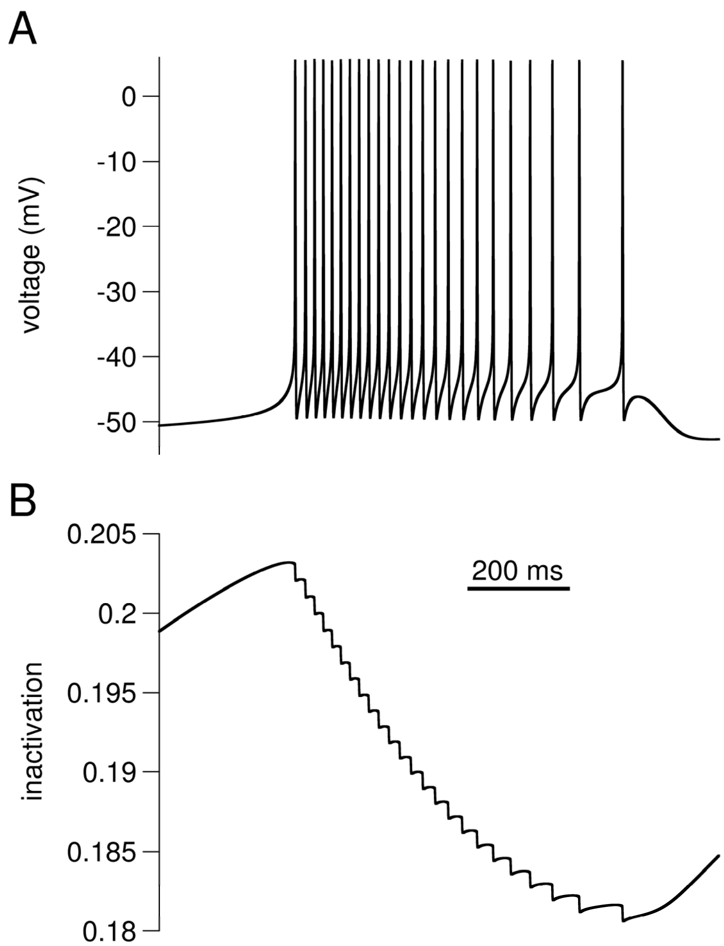

Figure 36. Inactivation variable, h_{NaP}, during a burst. **A**: Membrane potential. Spike frequency adaptation is displayed during a burst. **B**: Inactivation of the persistent sodium current, h_{NaP}. When h_{NaP} is sufficiently inactivated, the cell lacks the necessary inward current to sustain firing activity and the burst terminates.

5.3.1.3 Additional Currents

We will now examine during which phase of the bursting cycle each additional current is activated. Figure 35D illustrates the behavior of the two HVA calcium currents added to the model. The slowly inactivating HVA current, I_L, is quickly activated as the burst begins and inactivates throughout the intraburst interval. The non-inactivating current, I_{HVA}, inactivates slowly throughout the intraburst interval as the frequency of spiking inside the burst is reduced. Conversely, the LVA current is activated during the interburst interval and is inactivated during the burst (Figure 35E). The distinct properties of the calcium currents during a burst provide different methods of controlling the burst dynamics (see below).

The time course of I_H is also provided in Figure 35E. I_H produces an inward current during the interburst interval, but reverses sign during the burst and provides additional outward current. Unlike I_{NaP} which increasingly activates during the interburst interval, the H current is most activated at the beginning of the interburst interval and slowly reduces in amplitude throughout the remainder of the interburst interval. The A current (not shown), due to its hyperpolarized half-inactivation, is almost completely inactivated during normal bursting and requires hyperpolarization to make a contribution to the firing behavior of this model. Therefore, we expect this current would play a greater role in future network simulations that include inhibition.

5.3.2 Burst Dynamics

Next we compare the burst dynamics of the original and improved pBC models. Here, burst dynamics refers to the range of achievable burst periods and burst durations, as well as the range of applied input current over which bursts can be obtained. Compared to the original model employing its nominal parameter set, the improved model provides a much greater range of burst dynamics (Figure 37). However, Figure 6 of Butera et al. [18] reveals that the bursting range of the original model is increased with increased g_{NaP}. If g_{NaP} is increased to 4.0 nS in the original model, the range of applied current (I_{stim}) that generates bursting is from 3 to 17 nA. The obtainable range of burst periods is similar to that of the improved model, but the range of obtainable burst

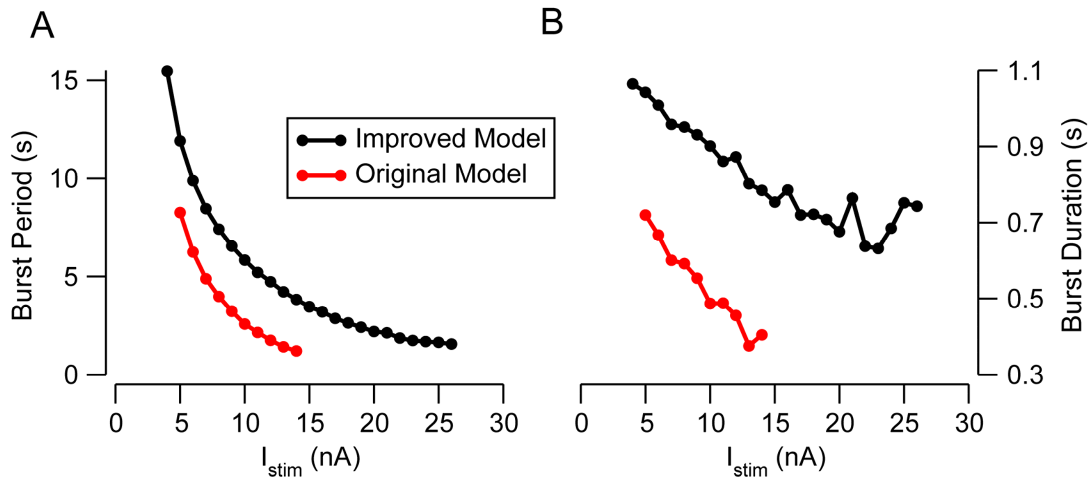

Figure 37. Burst period (**A**) and burst duration (**B**) of the improved and original pBC models for several levels of applied input current. Original model employs the nominal parameter set.

durations is about half that of the improved model (from ~ 0.8 to 1.0 seconds). Manual exploration of parameter space reveals that the improved pBC model is capable of producing burst durations from 0.3 to over 5.0 seconds. Thus, the improved pBC model provides better performance concerning burst dynamics, even when g_{NaP} of the original model is increased. The burst period and burst duration of the improved model are also within the range observed in many experiments [1, 7, 10, 66]. These results are encouraging since we would hope that adding currents to the original model would provide a range of burst dynamics at least as large as the original model and similar to that of experimental data. Other benefits of including the additional currents into the pBC model are described in the next section.

5.3.3 Significance of Additional Currents

The currents included in the improved pBC model provide additional controllability of burst dynamics not available in the original model (Figure 38). Figure

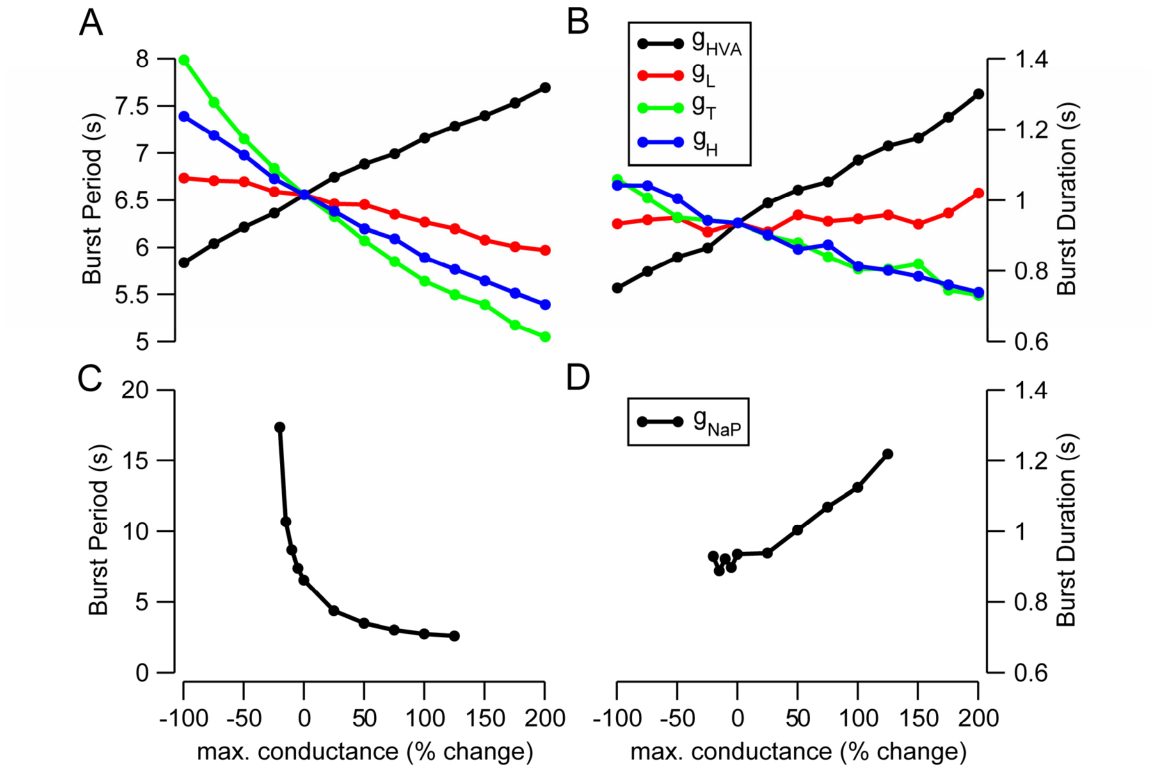

Figure 38. Controllability of burst dynamics in the improved pBC model. Burst period (**A,C**) and burst duration (**B,D**) dependence on calcium (I_{HVA}, I_L, and I_T) and H (I_H) currents (**A,B**) and the persistent sodium (I_{NaP}) current (**C,D**). Maximum conductance is varied from -100 to +200% of its nominal value (i.e. the value listed in Table 10).

38 illustrates the effect of varying the maximum conductance of various channels on the burst period and burst duration of the improved pBC model. Figure 38A,B reveals the differing contributions to burst period and burst duration of the calcium currents and the H current. The maximum conductance of I_{HVA} is positively correlated with burst period and burst duration (Figure 38A,B). In the original and improved pBC models, increasing the maximum conductance of I_{NaP} decreases the burst period while increasing burst duration (Figure 38C,D). Thus, including the HVA current in the improved model provides controllability not present in the original model, i.e. the ability to increase both burst period and burst duration by augmenting the channel density of an ionic current.

Interestingly, increasing the maximum conductance of the other high voltage-activated calcium channel in the improved model, I_L, has an effect similar to that of I_{NaP} (Figure 38). However, burst period is quite sensitive to reductions of I_{NaP}, whereas a reduction of I_L offers a more graded response (Figure 38A,B). Reducing the maximum conductance of I_{NaP} by more than 20% of its nominal value eliminates the models ability to generate bursting.

Both I_T and I_H provide a similar influence on burst duration and burst period, and this influence is opposite that of I_{HVA} (Figure 38A,B). As mentioned in Sec. 5.2.5, the role of I_H in rhythm generation is unclear. Our results suggest that decreasing I_H will increase both the burst period (or decrease burst frequency) and burst duration. This is inconsistent with both previously published reports of the role of I_H that suggest I_H either plays no role in rhythm generation [16], or blocking I_H increases burst frequency [123]. This issue is addressed in Sec. 5.4.2.

The inclusion of I_{HVA} allows for larger burst durations than the original model is capable of producing. The original model can produce burst durations near 1.1 second when g_{NaP} is increased [18], but the improved model can produce burst durations greater than 2 seconds (by increasing the density of HVA channels), which is similar to the values measured in some pacemaker cells in the pBC [10]. In the original model, increasing the applied stimulus current decreases the burst duration. This is also true with the nominal parameter set of the improved pBC model (Figure 37). However, when g_{HVA} is sufficiently increased, the improved model will display an increase in burst duration when the amplitude of the stimulus current is increased (not shown).

5.4 Discussion

We have developed an improved pBC cell model by increasing the complexity of the Butera et al. model [18] through the addition of several ionic currents now known to exist in these cells. The improved model reproduces the behaviors of the original model, extends the range of burst dynamics, and provides additional capabilities for controlling burst dynamics.

5.4.1 Burst Dynamics

One shortcoming of the original model is the sensitivity to parameters changes (e.g. the limited range of applied current that produces bursting). The improved model bursts over a greater range of applied currents, and is capable of producing a greater range of burst durations than what is possible in the original model. Indeed, the original model is incapable of generating bursts with a burst duration much larger than 1 second. On the other hand, the improved model is able to generate bursts with a burst duration greater than 2 seconds. Some pBC cells are able to generate burst durations in this range when synaptically isolated [10].

The additional currents of the improved pBC model also provide an increased ability to control burst period and burst duration compared to the original model. The HVA, T, and H currents allow burst period and burst duration to be increased or decreased in conjunction as their individual densities are varied. Varying the NaP current alone forces the burst period and burst duration to increase and decrease separately. The L current provides a mechanism for varying burst period and duration in similar to NaP, but in a manner that is not as sensitive to small changes in channel density.

As seen in Figure 35E, I_T and I_H are activated (and inward) during the interburst interval. This behavior explains the results of Figure 38A,B that demonstrate an increase in the density of either current will decrease burst period and burst duration. The increased inward current during the interburst interval reduces the time available for inactivation of NaP, or h_{NaP}, in between the bursts, which provides a reduced ability for h_{NaP} to de-inactivate during the burst. On the other hand, I_{HVA} is activated (and inward) only during the burst itself (Figure 35D). Since I_{HVA} does not inactivate, the hyperpolarization in between bursts does not affect its dynamics; therefore, I_{HVA} does not directly contribute to reducing the duration of the interburst interval. This characteristic of the HVA current at least partly explains the ability to increase burst period and burst duration as g_{HVA} is increased (Figure 38A,B).

Thoby-Brisson and Ramirez [10] demonstrate that CAN-bursters have larger burst durations (also called Type-2, or slow bursters in [10]). Our results indicate that adding HVA calcium channels indeed has the ability to extend burst duration, which suggests that one important difference between CAN bursters and NaP bursters may be an increase in the density of HVA calcium channels. Conversely, very small burst durations are also obtainable in the improved model when the density of the HVA calcium current is reduced and the densities of the T and H current are increased (as suggested by the results of Figure 38A,B). The smaller burst durations are more common in NaP-dependent bursters (also called Type-1, or fast bursters in [10]).

5.4.2 Limitations of the Model

Our results investigating the role of I_H in the pBC do not agree with either of the (conflicting) published reports regarding this issue [16, 123]. The lack of effect reported by Mironov et al. [16] could be contributed to the sparsity of this current (I_H is found in 15% of inspiratory pBC cells according to [16]) using their experimental preparation. The results of Thoby-Brisson and Ramirez [123] suggesting a decrease in I_H provides an increase in burst frequency are opposite of the results of our model. The reason for these differences is not obvious. It is possible the pharmacological blockers used are affecting more than just H channels, or our model does not include other mechanisms that would interact with I_H. The potential mechanisms do not include network interactions for the results of Thoby-Brisson and Ramirez [123] since their results were similar with or without the application of CNQX to block synaptic transmission. Thus, the counter-intuitive results of Thoby-Brisson and Ramirez [123] remained unexplained.

The model developed in this chapter is a model of the NaP-dependent burster found in the pBC. Additional mechanisms are required to model the CAN-bursters found in the pBC of transverse slice preparations from mice [9]. This will include a model of the CAN current itself, a model of the internal calcium concentration (perhaps similar to the one described in Sec. 2.1.2), a mechanism for burst initiation, and a mechanism responsible for burst termination (such as a BK or SK current).

5.4.3 Conclusions

The improved pBC model developed here not only provides a more accurate description of pBC cells by including additional currents now known to exist, but also provides a greater range of burst dynamics and controllability not available with the original model. For example, the HVA current allows the improved model to produce burst durations longer than the burst durations obtained by the original model, and this HVA-dependent mechanism may partially account for the different firing behaviors of the two types of pacemakers found in the pBC [10]. I_{HVA}, I_T, and I_H also provide a mechanism for increasing or decreasing burst period and burst duration concurrently, a feature not possible with the original model. Future network models that incorporate the improved pBC model developed in this chapter will enhance our understanding of how these currents contribute to network-wide rhythm generation.

CHAPTER 6: CONCLUSIONS

The ultimate goal of our research is to understand how the brain generates and transmits the respiratory rhythm. An understanding of the properly functioning network is required before the pathophysiology of diseases resulting in a malfunctioning network can be addressed. The transverse slice containing the pBC (for rhythm generation) and HMs (for rhythm transmission) is an important experimental preparation for studying respiration *in vitro*. We have developed Hodgkin-Huxley style ionic current models of respiratory neurons located in the transverse slice. These models allow us to investigate the role of various ion channels in neuronal firing at both the single cell and network level.

A single cell model of a hypoglossal motoneuron revealed the role of calcium and calcium-dependent potassium channels for generating the complex HM action potential shape. Age-dependent changes in these and other channels potentially explain the age-dependent characteristics of HMs. An automated optimization technique was used to optimize the HM model to more closely match experimental measures of action potential shape. Models of the burst generating cells in the transverse slice reveal that altering the ratio of critical subthreshold conductances can transform a pBC model into an intrinsic burster, or pacemaker neuron. As the number of pacemakers in an excitatory network is increased, the robustness of the network is enhanced. Including additional ion channels into the pBC model (i.e. HVA and LVA calcium channels, H channels, and A channels) augments the single cell bursting characteristics. The models developed in this study will be the foundation of future network models of the transverse slice.

6.1 Ionic Current Models

The first model developed in this study is an ionic current model of a HM, the cell responsible for transmitting the respiratory rhythm generated by the pBC out of the transverse slice and to the muscles. Compared to the action potential of the squid giant axon described by Hodgkin-Huxley, the HM action potential also displays an ADP and mAHP following the spike. The ADP is caused by an influx of calcium from calcium channels activated by the large depolarization of the action potential. This calcium influx in turn activates a calcium-activated potassium channel that causes a large hyperpolarization (or mAHP) following the ADP. We employed an analytical sensitivity analysis technique to quantitatively confirm the role of each channel in shaping action potential dynamics. Sensitivity analysis also provides predictions of membrane potential changes that are generally accurate within 20% of the nominal value. Once the role of each channel in shaping membrane voltage was determined, the model was used to analyze the age-dependent changes observed in HMs.

The hyperpolarization-activated cationic current in HMs increases in density by 10-fold as the rat ages from neonatal and adult. This age-dependent change is easily modeled by increasing the maximum conductance of the H current. These simulations suggest that the increase in H current density alone can account for the decrease in mAHP duration observed in HMs. Other age-dependent changes include a change in calcium current density and firing properties. Since the firing behavior of HMs is strongly influenced by calcium channels, we examined the model activity as the calcium channel conductances were varied. We found that the firing behavior of the HM model could change from an adapting firing pattern to an accelerating firing pattern as the densities of the fast inactivating calcium channels were increased. Using the model, we were able to confirm that the effects were caused by the contribution of the calcium channels to the calcium-dependent potassium current by excluding certain calcium channels from the equation describing calcium dynamics. All of these age-dependent studies demonstrate the usefulness of neuronal models for studying neural behavior since reproducing these studies experimentally is an impossible task.

We used a previously developed ionic current model of a pBC cell to explore the significance of intrinsic bursters for rhythmogenesis. This minimal model includes four channels: the fast sodium, delayed rectifier potassium, and leak channels that cause the action potential, as well as a (slowly inactivating) persistent sodium channel responsible for bursting. We altered the ratio of the persistent sodium conductance to the leak conductance to create two subpopulations of model cells, some with the intrinsic ability to burst and others that were incapable of bursting. These network models, with parameters biased by experimental distributions of persistent sodium and leak conductance parameters, were used to investigate how variations of critical subthreshold conductances can affect network dynamics (see below).

We then improved the minimal pBC model by including other currents found in these cells. These currents include one low- and two high-voltage activated calcium currents, a hyperpolarization activated cationic current, and a fast transient potassium current. Inclusion of these currents in the minimal pBC model extends the range of bursting dynamics exhibited by these models. The results reveal the differential roles of the various ion channels in shaping the bursting characteristics of these cells. These results are useful for future simulations that incorporate the effects of neuromodulators in this network.

Although the HM and improved pBC models share many of the same ionic currents, their firing characteristics are drastically different. Although there are several minor discrepancies between the formulations of each current, the primary reason for the difference in firing characteristic is the presence of the calcium-dependent potassium current in the HM model. The large influx of calcium following the action potential quickly activates the calcium-dependent potassium current in the HM model and this current generates the mAHP. These calcium-dependent mechanisms dominate the control of the firing behavior of HMs.

6.2 Role of Pacemakers

The number and necessity of pacemakers in the pBC is currently a strongly debated topic in respiratory neuroscience. Since modeling is ideally suited for addressing issues requiring mechanistic analysis, we used modeling studies to explore the significance of pacemakers in the pBC. Our results reveal that as the fraction of the network population that is made up of intrinsic bursters is increased, the robustness of network dynamics is also increased. Robustness is quantified in terms of both the input range (the size of parameter space where network-wide synchronous rhythmic bursting occurs) and output range (the range of bursting frequencies that the network produces across this input range) of the network. Our study is the first to quantitatively address the question of the contributions of pacemaker neurons to the dynamic performance of excitatory networks.

Our network simulation results confirmed previous results that demonstrate network-wide bursting is possible in an excitatory network made up exclusively of non-pacemakers; however, under these conditions the input and output range is greatly reduced. Inclusion of pacemakers allows the input and output range to more than triple compared to networks containing only non-pacemakers. The largest increase in dynamic range occurs when the network contains greater than 20% pacemakers. Our simulations revealed that although increasing synaptic coupling strength can increase input range, increased coupling decreases output range. Alternatively, increasing the number of pacemakers increases both input and output range. Our simulations provide an important contribution to the current pacemaker debate in respiratory neuroscience, and we expect future experimental confirmation of our model predictions.

6.3 Model Optimization

The complicated and time-consuming task of hand-tuning model parameters is a necessary component of model development. However, automated optimization techniques are often employed to fine-tune model parameters after the modeler has determined parameters close to the desired goal. We used a genetic algorithm to optimize our HM model to more closely match experimental measures of action potential shape. A genetic algorithm was chosen for this problem because they have previously been shown to perform well when optimizing complex neural models. The genetic algorithm revealed the importance of including all parameters in an automated optimization technique. Indeed, the best models were obtained almost exclusively by average changes of less than 5% of parameters other than maximum conductances, a common target of neuron model optimizations. While optimizing our HM model, we compared three different fitness functions: a template-based fitness function, a feature-based fitness function, and a combination of the template- and fitness-based fitness functions. Our results revealed that a feature-based fitness function outperforms the template-based fitness function for fitting the complex action potential shape of HMs. The combined fitness function provides additional benefit if input impedance (a measure not included in the template-based fitness function) is excluded from the calculations.

6.4 Future Research Directions

Several future research directions of this study are proposed, some of which have already begun. The HM and pBC models developed in this study will be enhanced by incorporating the effects of neuromodulators acting on this network. The actions of neuromodulators such as 5-HT and substance P on HM and pBC cells have been thoroughly studied and their inclusion in future models will provide a deeper understanding of the function of these cells in respiration. Our HM and pBC models are also the building blocks of a future comprehensive network model of the entire transverse slice. While our individual cell models allow us to examine the direct effects of perturbations on single cells, a comprehensive network model will allow us to understand the indirect effects transmitted throughout the network by perturbations of individual cells in the network.

The results of the genetic algorithm study can be extended to explore the age-dependent changes we investigated through hand-tuning of model parameters. Although we used a list of experimental measures of action potential shape for neonatal HMs, a similar list for adult neurons is currently available. Based on our genetic algorithm studies, we recommend using these experimental measures in a feature-based fitness function to transform the model from a neonatal HM model into an adult HM model. A similar approach can be used to transform the HM model into a model of the pre-motoneurons with similar action potential characteristics located in the transverse slice. Such research endeavors could easily take advantage of the simulation framework already developed in this study.

The research presented here provides a critical step towards understanding the vital role of the brain in generating and transmitting the respiratory rhythm. Future modeling studies will use the models and techniques we have developed as their foundation and may some day contribute to improving the quality of life of individuals suffering from debilitating diseases affecting the neural control of respiration.

APPENDIX A: HM MODEL EQUATIONS

Sodium Current: I_{Na}

$$I_{Na} = \bar{g}_{Na} m^3 h (V - E_{Na})$$

$$m_\infty(\mathrm{V}) = \frac{1}{1 + e^{-(\mathrm{V}+36)/8.5}} \qquad \tau_m(\mathrm{V}) = 0.1$$

$$h_\infty(\mathrm{V}) = \frac{1}{1 + e^{(\mathrm{V}+44.1)/7}} \qquad \tau_h(\mathrm{V}) = \frac{3.5}{e^{(\mathrm{V}+35)/4} + e^{-(\mathrm{V}+35)/25}} + 1$$

Persistent Sodium Current: I_{NaP}

$$I_{NaP} = \bar{g}_{NaP} m_{NaP} h_{NaP} (V - E_{Na})$$

$$m_{NaP\infty}(\mathrm{V}) = \frac{1}{1 + e^{-(\mathrm{V}+47.1)/4.1}} \qquad \tau_{mNaP}(\mathrm{V}) = 0.1$$

$$h_{NaP\infty}(\mathrm{V}) = \frac{1}{1 + e^{(\mathrm{V}+65)/5}} \qquad \tau_{hNaP}(\mathrm{V}) = 150$$

Delayed-Rectifier Current: I_K

$$I_K = \bar{g}_K n^4 (V - E_K)$$

$$n_\infty(\mathrm{V}) = \frac{1}{1 + e^{-(\mathrm{V}+30)/25}} \qquad \tau_n(\mathrm{V}) = \frac{2.5}{e^{(\mathrm{V}+30)/40} + e^{-(\mathrm{V}+30)/50}} + 0.01$$

Leak Current: I_{leak}

$$I_{leak} = g_{leak}(V - E_{leak})$$

LVA Calcium Current: I_T

$$I_T = \bar{g}_T m_T h_T (V - E_{Ca})$$

$$m_{T\infty}(\mathrm{V}) = \frac{1}{1 + e^{-(\mathrm{V}+38)/5}} \qquad \tau_{mT}(\mathrm{V}) = \frac{5}{e^{(\mathrm{V}+28)/25} + e^{-(\mathrm{V}+28)/70}} + 2$$

$$h_{T\infty}(\mathrm{V}) = \frac{1}{1 + e^{(\mathrm{V}+70.1)/7}} \qquad \tau_{hT}(\mathrm{V}) = \frac{20}{e^{(\mathrm{V}+70)/65} + e^{-(\mathrm{V}+70)/65}} + 1$$

HVA Calcium Current: I_N

$$I_N = \bar{g}_N m_N h_N (V - E_{Ca})$$

$$m_{N\infty}(\mathrm{V}) = \frac{1}{1 + e^{-(\mathrm{V}+30)/6}} \qquad \tau_{mN}(\mathrm{V}) = 5$$

$$h_{N\infty}(\mathrm{V}) = \frac{1}{1 + e^{(\mathrm{V}+70)/3}} \qquad \tau_{hN}(\mathrm{V}) = 25$$

HVA Calcium Current: I_P

$$I_P = \bar{g}_P m_P (V - E_{Ca})$$

$$m_{P\infty}(\mathrm{V}) = \frac{1}{1 + e^{-(\mathrm{V}+17)/3}} \qquad \tau_{mP}(\mathrm{V}) = 10$$

Calcium-Dependent Potassium Current: I_{SK}

$$I_{SK} = \bar{g}_{SK} z_{SK}^2 (V - E_K)$$

$$z_{SK\infty}([Ca^{2+}]_i) = 1 \Big/ \left(1 + \left(\frac{0.003}{[Ca^{2+}]_i} \right)^2 \right) \qquad \tau_{zSK}([Ca^{2+}]_i) = 1$$

Fast-Transient Potassium Current: I_A

$$I_A = \bar{g}_A m_A h_A (V - E_K)$$

$$m_{A\infty}(\mathrm{V}) = \frac{1}{1 + e^{-(\mathrm{V}+27)/16}} \qquad \tau_{mA}(\mathrm{V}) = \frac{1}{e^{(\mathrm{V}+40)/5} + e^{-(\mathrm{V}+74)/7.5}} + 0.37$$

$$h_{A\infty}(\mathrm{V}) = \frac{1}{1 + e^{(\mathrm{V}+80)/11}} \qquad \tau_{hA}(\mathrm{V}) = 20$$

Hyperpolarization-Activated Current: I_H

$$I_H = \bar{g}_H m_H (V - E_H)$$

$$m_{H\infty}(\mathrm{V}) = \frac{1}{1 + e^{(\mathrm{V}+79.8)/5.3}} \qquad \tau_{mH}(\mathrm{V}) = \frac{475}{e^{(\mathrm{V}+70)/11} + e^{-(\mathrm{V}+70)/11}} + 50$$

APPENDIX B: SENSITIVITY ANALYSIS

Sensitivity analysis is used to determine the sensitivity of a state variable to a change in a model parameter [79]. In this case, it is used to determine the sensitivity of the membrane voltage to the maximum conductance of each current, as done in Nygren et al. [78]. A brief derivation is given below (see also [78]).

The general form of our model is

$$\frac{d}{dt}\mathbf{x} = \mathbf{f}(\alpha, x, t)$$

where x is the state variable of interest (membrane voltage, in our case), f is the model equation that depends on α, a model parameter (maximum conductance); x; and t, time. Taking the partial derivative of each side gives

$$\frac{\partial}{\partial \alpha_k}\left\{\frac{d}{dt}\mathbf{x}\right\} = \frac{\partial}{\partial \alpha_k}\mathbf{f}(\alpha, \mathbf{x}, t) =$$

$$J_{\mathbf{x}}^{\mathbf{f}}\frac{\partial \mathbf{x}}{\partial \alpha_k} + \frac{\partial \mathbf{f}}{\partial \alpha_k}$$

where

$$J_{\mathbf{x}}^{\mathbf{f}} = \begin{bmatrix} \frac{\partial f_1}{\partial x_1} & \cdots & \frac{\partial f_1}{\partial x_N} \\ \vdots & \ddots & \vdots \\ \frac{\partial f_N}{\partial x_1} & \cdots & \frac{\partial f_N}{\partial x_N} \end{bmatrix}$$

The time derivative can be written similarly and shows that

$$\frac{d}{dt}\mathbf{x}(\alpha, t) = J_{\alpha}^{\mathbf{x}}\frac{\partial \alpha}{\partial t} + \frac{\partial \mathbf{x}(\alpha, t)}{\partial t} = \frac{\partial}{\partial t}\mathbf{x}(\alpha, t)$$

because all parameters are time invariant. Therefore:

$$\frac{\partial}{\partial \alpha_k}\left\{\frac{\partial}{\partial t}\mathbf{x}\right\} = J_{\mathbf{x}}^{\mathbf{f}}\frac{\partial \mathbf{x}}{\partial \alpha_k} + \frac{\partial \mathbf{f}}{\partial \alpha_k}$$

Interchanging the order of integration

$$\frac{\partial}{\partial t}\left\{\frac{\partial}{\partial \alpha_k}\mathbf{x}\right\} = \frac{\partial}{\partial t}\boldsymbol{\varepsilon}_k = J_{\mathbf{x}}^{\mathbf{f}}\frac{\partial \mathbf{x}}{\partial \alpha_k} + \frac{\partial \mathbf{f}}{\partial \alpha_k}$$

where $\boldsymbol{\varepsilon}_k$, the sensitivity of $\mathbf{x}$ with respect to α_k, is defined as:

$$\boldsymbol{\varepsilon}_k = \frac{\partial}{\partial \alpha_k}\mathbf{x}$$

Thus the sensitivity variables are solved according to

$$\frac{\partial}{\partial t}\boldsymbol{\varepsilon}_k = J_{\mathbf{x}}^{\mathbf{f}}\frac{\partial \mathbf{x}}{\partial \alpha_k} + \frac{\partial \mathbf{f}}{\partial \alpha_k}$$

This equation is integrated in parallel with the model equations and produces the desired sensitivity functions.

APPENDIX C: ORIGINAL PBC MODEL DESCRIPTION

The model used for all simulations in Chapter 4 is a modified version of model 1 of Butera et al. [18] and is based on a single-compartment Hodgkin-Huxley [21] formalism. The membrane potential is found using the differential equation

$$\mathrm{dV/dt} = \left(-\sum I_{ionic} + I_{tonic} + I_{syn}\right)/\,\mathrm{C_m}$$

where V is the membrane potential (mV), C_m is the whole cell capacitance (21 pF), t is time (ms), I_{tonic} is the excitatory drive current (nA), I_{syn} is the synaptic current (nA) from other pBC cells in the network, and I_{ionic} are the ionic currents listed below and have the form

$$I_{ionic} = g\left(\mathrm{V} - E_{ionic}\right)$$

where E_{ionic} is the equilibrium reversal potential for the ionic species carried by the current and

$$g = \bar{g}x$$

where $\bar{g}$ is the maximum conductance of each current, and x is the product of one or more gating variables raised to integer powers, as described below.

The dynamics of the conductances of the ionic currents regulated by voltage-dependent activation or inactivation variables are described according to

$$\frac{dx}{dt} = \frac{x_\infty(\mathrm{V}) - x}{\tau_x(\mathrm{V})}$$

$$x_\infty(\mathrm{V}) = 1/\left(1 + e^{(\mathrm{V}-\theta_x)/\sigma_x}\right)$$

$$\tau_x(\mathrm{V}) = \bar{\tau}_x / \cosh[(\mathrm{V} - \theta_x)/2\sigma_x)]$$

where $x_\infty(V)$ is the steady-state voltage-dependent (in)activation function of x and $\tau_x(V)$ is the voltage-dependent time constant. $x_\infty(V)$ is a sigmoid with a half-(in)activation at V = θ_x and a slope factor σ_x. $\tau_x(V)$ is a bell-shaped curve that has a maximal value $\bar{\tau}_x$ at V = θ_x and a half-width determined by σ_x. Thus each gating variable is described by only three parameters.

Action potentials in the model are generated by a fast Na^+ current (I_{Na}) and a delayed-rectifier K^+ current (I_K). The equations for these currents are inspired by the HH-formulation, but the gating variables satisfy a reduced voltage-dependent description

$$I_{Na} = \bar{g}_{Na} m_\infty^3(\mathrm{V})(1-n)(\mathrm{V}-E_{Na})$$

$$I_K = \bar{g}_K n^4(\mathrm{V}-E_K)$$

where the parameters of I_{Na} are $\bar{g}_{Na}$ = 28 nS, E_{Na} = 50 mV, θ_m = -34 mV, and σ_m = -5 mV and the parameters of I_K are $\bar{g}_K$ = 11.2 nS, E_K = -85 mV, θ_n = -29 mV, σ_n = -4 mV, $\bar{\tau}_n$ = 10 ms.

The persistent sodium current is described by the following equation

$$I_{Na} = \bar{g}_{NaP} m_\infty(\mathrm{V}) h(\mathrm{V}-E_{Na})$$

where E_{Na} = 50 mV, θ_m = -45.1 mV, σ_m = -5 mV, θ_h = -53 mV, σ_h = 6 mV, $\bar{\tau}_h$ = 10,000 ms. $\bar{g}_{NaP}$ is varied in each simulation as described above.

The model has a passive leak current defined as

$$I_{Leak} = \bar{g}_{Leak}(\mathrm{V}-E_{Leak})$$

This current is K^+ dominated. E_L is set to -70 mV and $\bar{g}_{Leak}$ is varied in each simulation as described above. The reader is referred to Butera et al. [18, 19] for a more detailed description of the model.

APPENDIX D: IMPROVED PBC MODEL EQUATIONS

Sodium Current: I_{Na}

$$I_{Na} = \bar{g}_{Na} m_\infty^3(\mathrm{V})(1-n)(\mathrm{V}-E_{Na})$$

$$m_\infty(\mathrm{V}) = \frac{1}{1+e^{-(\mathrm{V}+34)/5}}$$

$$n_\infty(\mathrm{V}) = \frac{1}{1+e^{-(\mathrm{V}+29)/4}} \qquad \tau_n(\mathrm{V}) = \frac{10}{\cosh[(\mathrm{V}-29)/8)]}$$

Persistent Sodium Current: I_{NaP}

$$I_{Na} = \bar{g}_{NaP} m_{NaP\infty}(\mathrm{V}) h_{NaP}(\mathrm{V}-E_{Na})$$

$$m_{NaP\infty}(\mathrm{V}) = \frac{1}{1+e^{-(\mathrm{V}+45.1)/5}}$$

$$h_{NaP\infty}(\mathrm{V}) = \frac{1}{1+e^{(\mathrm{V}+53)/6}} \qquad \tau_{hNaP}(\mathrm{V}) = \frac{10{,}000}{\cosh[(\mathrm{V}-53)/12)]}$$

Delayed-Rectifier Current: I_K

$$I_K = \bar{g}_K n^4 \left(V - E_K\right)$$

$$n_\infty(\mathrm{V}) = \frac{1}{1+e^{-(\mathrm{V}+29)/4}} \qquad \tau_n(\mathrm{V}) = \frac{10}{\cosh[(\mathrm{V}-29)/8)]}$$

Leak Currents: I_{LK} and I_{NSLK}

$$I_{KLK} = g_{KLK}(V - E_{KLK})$$

$$I_{NSLK} = g_{NSLK}(V - E_{NSLK})$$

LVA Calcium Current: I_T

$$I_T = \bar{g}_T m_T h_T \left(V - E_{Ca}\right)$$

$$m_{T\infty}(\mathrm{V}) = \frac{1}{1 + e^{-(\mathrm{V}+59.05)/2.36}}$$

$$\tau_{mT}(\mathrm{V}) = 25$$

$$h_{T\infty}(\mathrm{V}) = \frac{1}{1 + e^{(\mathrm{V}+80.72)/5.31}}$$

$$\tau_{hT}(\mathrm{V}) = \frac{50}{\cosh[(\mathrm{V} - 80.72)/15)]} + 1$$

HVA Calcium Current: I_L

$$I_L = \bar{g}_L m_L h_L \left(V - E_{Ca}\right)$$

$$m_{L\infty}(\mathrm{V}) = \frac{1}{1 + e^{-(\mathrm{V}+27.82)/5.69}}$$

$$\tau_{mL}(\mathrm{V}) = 20$$

$$h_{L\infty}(\mathrm{V}) = \frac{1}{1 + e^{(\mathrm{V}+52.40)/5.23}}$$

$$\tau_{hL}(\mathrm{V}) = 450$$

HVA Calcium Current: I_{HVA}

$$I_{\mathrm{HVA}} = \bar{g}_{\mathrm{HVA}} m_{\mathrm{HVA}} \left(V - E_{Ca}\right)$$

$$m_{\mathrm{HVA}\infty}(\mathrm{V}) = \frac{1}{1 + e^{-(\mathrm{V}+27.82)/5.69}} \qquad \tau_{m\mathrm{HVA}}(\mathrm{V}) = 10$$

Fast-Transient Potassium Current: I_A

$$I_A = \bar{g}_A m_A h_A \left(V - E_K\right)$$

$$m_{A\infty}(\mathrm{V}) = \frac{1}{1 + e^{-(\mathrm{V}+50)/10}} \qquad \tau_{mA}(\mathrm{V}) = 1$$

$$h_{A\infty}(\mathrm{V}) = \frac{1}{1 + e^{(\mathrm{V}+70)/7}} \qquad \tau_{hA}(\mathrm{V}) = 25$$

Hyperpolarization-Activated Current: I_H

$$I_H = \bar{g}_H m_H \left(V - E_H\right)$$

$$m_{H\infty}(\mathrm{V}) = \frac{1}{1 + e^{(\mathrm{V}+78)/7}} \qquad \tau_{mH}(\mathrm{V}) = \frac{500}{\cosh[(\mathrm{V} - 70)/7)]} + 50$$

REFERENCES

[1] J. C. Smith, H. H. Ellenberger, K. Ballanyi, D. W. Richter, and J. L. Feldman, "Pre-Botzinger complex: a brainstem region that may generate respiratory rhythm in mammals," *Science*, vol. 254, pp. 726-9, 1991.

[2] P. A. Gray, W. A. Janczewski, N. Mellen, D. R. McCrimmon, and J. L. Feldman, "Normal breathing requires preBotzinger complex neurokinin-1 receptor-expressing neurons," *Nat Neurosci*, vol. 4, pp. 927-30, 2001.

[3] J. C. Smith, J. J. Greer, G. S. Liu, and J. L. Feldman, "Neural mechanisms generating respiratory pattern in mammalian brain stem-spinal cord in vitro. I. Spatiotemporal patterns of motor and medullary neuron activity," *J Neurophysiol*, vol. 64, pp. 1149-69, 1990.

[4] T. Suzue, "Respiratory rhythm generation in the in vitro brain stem-spinal cord preparation of the neonatal rat," *J Physiol*, vol. 354, pp. 173-83, 1984.

[5] N. M. Mellen, W. K. Milsom, and J. L. Feldman, "Hypothermia and recovery from respiratory arrest in a neonatal rat in vitro brain stem preparation," *Am J Physiol Regul Integr Comp Physiol*, vol. 282, pp. R484-91, 2002.

[6] S. M. Johnson, J. C. Smith, G. D. Funk, and J. L. Feldman, "Pacemaker behavior of respiratory neurons in medullary slices from neonatal rat," *J Neurophysiol*, vol. 72, pp. 2598-608, 1994.

[7] F. Pena, M. A. Parkis, A. K. Tryba, and J. M. Ramirez, "Differential contribution of pacemaker properties to the generation of respiratory rhythms during normoxia and hypoxia," *Neuron*, vol. 43, pp. 105-17, 2004.

[8] C. A. Del Negro, N. Koshiya, R. J. Butera, Jr., and J. C. Smith, "Persistent sodium current, membrane properties and bursting behavior of pre-botzinger complex inspiratory neurons in vitro," *J Neurophysiol*, vol. 88, pp. 2242-50, 2002.

[9] C. A. Del Negro, C. Morgado-Valle, J. A. Hayes, D. D. Mackay, R. W. Pace, E. A. Crowder, and J. L. Feldman, "Sodium and calcium current-mediated pacemaker neurons and respiratory rhythm generation," *J Neurosci*, vol. 25, pp. 446-53, 2005.

[10] M. Thoby-Brisson and J. M. Ramirez, "Identification of two types of inspiratory pacemaker neurons in the isolated respiratory neural network of mice," *J Neurophysiol*, vol. 86, pp. 104-12, 2001.

[11] S. Pagliardini, T. Adachi, J. Ren, G. D. Funk, and J. J. Greer, "Fluorescent tagging of rhythmically active respiratory neurons within the pre-Botzinger complex of rat medullary slice preparations," *J Neurosci*, vol. 25, pp. 2591-6, 2005.

[12] A. K. Tryba, F. Pena, and J. M. Ramirez, "Gasping activity in vitro: a rhythm dependent on 5-HT2A receptors," *J Neurosci*, vol. 26, pp. 2623-34, 2006.

[13] N. Koshiya and J. C. Smith, "Neuronal pacemaker for breathing visualized in vitro," *Nature*, vol. 400, pp. 360-3, 1999.

[14] J. F. Paton, A. P. Abdala, H. Koizumi, J. C. Smith, and W. M. St-John, "Respiratory rhythm generation during gasping depends on persistent sodium current," *Nat Neurosci*, vol. 9, pp. 311-3, 2006.

[15] F. P. Elsen and J. M. Ramirez, "Calcium currents of rhythmic neurons recorded in the isolated respiratory network of neonatal mice," *J Neurosci*, vol. 18, pp. 10652-62, 1998.

[16] S. L. Mironov, K. Langohr, and D. W. Richter, "Hyperpolarization-activated current, Ih, in inspiratory brainstem neurons and its inhibition by hypoxia," *Eur J Neurosci*, vol. 12, pp. 520-6, 2000.

[17] J. C. Rekling, J. Champagnat, and M. Denavit-Saubie, "Electroresponsive properties and membrane potential trajectories of three types of inspiratory neurons in the newborn mouse brain stem in vitro," *J Neurophysiol*, vol. 75, pp. 795-810, 1996.

[18] R. J. Butera, Jr., J. Rinzel, and J. C. Smith, "Models of respiratory rhythm generation in the pre-Botzinger complex. I. Bursting pacemaker neurons," *J Neurophysiol*, vol. 82, pp. 382-97, 1999.

[19] R. J. Butera, Jr., J. Rinzel, and J. C. Smith, "Models of respiratory rhythm generation in the pre-Botzinger complex. II. Populations Of coupled pacemaker neurons," *J Neurophysiol*, vol. 82, pp. 398-415, 1999.

[20] A. J. Berger, "Determinants of respiratory motoneuron output," *Respir Physiol*, vol. 122, pp. 259-69, 2000.

[21] A. L. Hodgkin and A. F. Huxley, "A quantitative description of membrane current and its application to conduction and excitation in nerve," *J Physiol*, vol. 117, pp. 500-44, 1952.

[22] I. A. Rybak, J. F. Paton, and J. S. Schwaber, "Modeling neural mechanisms for genesis of respiratory rhythm and pattern. I. Models of respiratory neurons," *J Neurophysiol*, vol. 77, pp. 1994-2006, 1997.

[23] I. A. Rybak, J. F. Paton, and J. S. Schwaber, "Modeling neural mechanisms for genesis of respiratory rhythm and pattern. II. Network models of the central respiratory pattern generator," *J Neurophysiol*, vol. 77, pp. 2007-26, 1997.

[24] I. A. Rybak, N. A. Shevtsova, W. M. St-John, J. F. Paton, and O. Pierrefiche, "Endogenous rhythm generation in the pre-Botzinger complex and ionic currents: modelling and in vitro studies," *Eur J Neurosci*, vol. 18, pp. 239-57, 2003.

[25] E. K. Kosmidis, O. Pierrefiche, and J. F. Vibert, "Respiratory-like rhythmic activity can be produced by an excitatory network of non-pacemaker neuron models," *J Neurophysiol*, vol. 92, pp. 686-99, 2004.

[26] M. A. Nogues, A. J. Roncoroni, and E. Benarroch, "Breathing control in neurological diseases," *Clin Auton Res*, vol. 12, pp. 440-9, 2002.

[27] H. C. Kinney, J. J. Filiano, L. A. Sleeper, F. Mandell, M. Valdes-Dapena, and W. F. White, "Decreased muscarinic receptor binding in the arcuate nucleus in sudden infant death syndrome," *Science*, vol. 269, pp. 1446-50, 1995.

[28] C. Mallard, M. Tolcos, J. Leditschke, P. Campbell, and S. Rees, "Reduction in choline acetyltransferase immunoreactivity but not muscarinic-m2 receptor immunoreactivity in the brainstem of SIDS infants," *J Neuropathol Exp Neurol*, vol. 58, pp. 255-64, 1999.

[29] A. Panigrahy, J. J. Filiano, L. A. Sleeper, F. Mandell, M. Valdes-Dapena, H. F. Krous, L. A. Rava, W. F. White, and H. C. Kinney, "Decreased kainate receptor binding in the arcuate nucleus of the sudden infant death syndrome," *J Neuropathol Exp Neurol*, vol. 56, pp. 1253-61, 1997.

[30] D. Bartlett, Jr., J. C. Leiter, and S. L. Knuth, "Control and actions of the genioglossus muscle," *Prog Clin Biol Res*, vol. 345, pp. 99-107; discussion 108, 1990.

[31] H. C. Kinney, "Abnormalities of the brainstem serotonergic system in the sudden infant death syndrome: a review," *Pediatr Dev Pathol*, vol. 8, pp. 507-24, 2005.

[32] F. Pena and J. M. Ramirez, "Endogenous activation of serotonin-2A receptors is required for respiratory rhythm generation in vitro," *J Neurosci*, vol. 22, pp. 11055-64, 2002.

[33] J. M. Ramirez, S. W. Schwarzacher, O. Pierrefiche, B. M. Olivera, and D. W. Richter, "Selective lesioning of the cat pre-Botzinger complex in vivo eliminates breathing but not gasping," *J Physiol*, vol. 507 (Pt 3), pp. 895-907, 1998.

[34] P. A. Gray, J. C. Rekling, C. M. Bocchiaro, and J. L. Feldman, "Modulation of respiratory frequency by peptidergic input to rhythmogenic neurons in the preBotzinger complex," *Science*, vol. 286, pp. 1566-8, 1999.

[35] S. P. Lieske, M. Thoby-Brisson, P. Telgkamp, and J. M. Ramirez, "Reconfiguration of the neural network controlling multiple breathing patterns: eupnea, sighs and gasps [see comment]," *Nat Neurosci*, vol. 3, pp. 600-7, 2000.

[36] G. D. Funk, J. C. Smith, and J. L. Feldman, "Generation and transmission of respiratory oscillations in medullary slices: role of excitatory amino acids," *J Neurophysiol*, vol. 70, pp. 1497-515, 1993.

[37] S. M. Johnson, N. Koshiya, and J. C. Smith, "Isolation of the kernel for respiratory rhythm generation in a novel preparation: the pre-Botzinger complex "island"," *J Neurophysiol*, vol. 85, pp. 1772-6, 2001.

[38] C. A. Del Negro, C. Morgado-Valle, and J. L. Feldman, "Respiratory rhythm: an emergent network property?," *Neuron*, vol. 34, pp. 821-30, 2002.

[39] J. C. Smith, R. J. Butera, N. Koshiya, C. Del Negro, C. G. Wilson, and S. M. Johnson, "Respiratory rhythm generation in neonatal and adult mammals: the hybrid pacemaker-network model," *Respir Physiol*, vol. 122, pp. 131-47, 2000.

[40] J. L. Feldman and C. A. Del Negro, "Looking for inspiration: new perspectives on respiratory rhythm," *Nat Rev Neurosci*, vol. 7, pp. 232-42, 2006.

[41] I. C. Solomon, N. H. Edelman, and J. A. Neubauer, "Pre-Botzinger complex functions as a central hypoxia chemosensor for respiration in vivo," *J Neurophysiol*, vol. 83, pp. 2854-68, 2000.

[42] S. M. Johnson, J. C. Smith, and J. L. Feldman, "Modulation of respiratory rhythm in vitro: role of Gi/o protein-mediated mechanisms," *J Appl Physiol*, vol. 80, pp. 2120-33, 1996.

[43] S. W. Schwarzacher, A. Pestean, S. Gunther, and K. Ballanyi, "Serotonergic modulation of respiratory motoneurons and interneurons in brainstem slices of perinatal rats," *Neuroscience*, vol. 115, pp. 1247-59, 2002.

[44] I. C. Solomon, "Modulation of gasp frequency by activation of pre-Botzinger complex in vivo," *J Neurophysiol*, vol. 87, pp. 1664-8, 2002.

[45] J. M. Ramirez, A. K. Tryba, and F. Pena, "Pacemaker neurons and neuronal networks: an integrative view," *Curr Opin Neurobiol*, vol. 14, pp. 665-74, 2004.

[46] F. Pena and J. M. Ramirez, "Substance P-mediated modulation of pacemaker properties in the mammalian respiratory network," *J Neurosci*, vol. 24, pp. 7549-56, 2004.

[47] A. Sawczuk and K. M. Mosier, "Neural control of tongue movement with respect to respiration and swallowing," *Crit Rev Oral Biol Med*, vol. 12, pp. 18-37, 2001.

[48] A. A. Lowe, "The neural regulation of tongue movements," *Prog Neurobiol*, vol. 15, pp. 295-344, 1980.

[49] R. B. Fogel, A. Malhotra, S. A. Shea, J. K. Edwards, and D. P. White, "Reduced genioglossal activity with upper airway anesthesia in awake patients with OSA," *J Appl Physiol*, vol. 88, pp. 1346-54, 2000.

[50] J. E. Remmers, W. J. deGroot, E. K. Sauerland, and A. M. Anch, "Pathogenesis of upper airway occlusion during sleep," *J Appl Physiol*, vol. 44, pp. 931-8, 1978.

[51] F. P. Elsen and J. M. Ramirez, "Postnatal development differentially affects voltage-activated calcium currents in respiratory rhythmic versus nonrhythmic neurons of the pre-Botzinger complex," *J Neurophysiol*, vol. 94, pp. 1423-31, 2005.

[52] H. Koizumi and J. C. Smith, "Functional heterogeneity of persistent sodium conductance with the respiratory network *in vitro*.," *Soc. Neurosci. Abst.*, vol. 424.1, 2004.

[53] G. G. Haddad, D. F. Donnelly, and P. A. Getting, "Biophysical properties of hypoglossal neurons in vitro: intracellular studies in adult and neonatal rats," *J Appl Physiol*, vol. 69, pp. 1509-17, 1990.

[54] R. Lape and A. Nistri, "Characteristics of fast Na(+) current of hypoglossal motoneurons in a rat brainstem slice preparation," *Eur J Neurosci*, vol. 13, pp. 763-72, 2001.

[55] R. Lape and A. Nistri, "Voltage-activated K+ currents of hypoglossal motoneurons in a brain stem slice preparation from the neonatal rat," *J Neurophysiol*, vol. 81, pp. 140-8, 1999.

[56] R. K. Powers and M. D. Binder, "Persistent sodium and calcium currents in rat hypoglossal motoneurons," *J Neurophysiol*, vol. 89, pp. 615-24, 2003.

[57] F. Viana, D. A. Bayliss, and A. J. Berger, "Calcium conductances and their role in the firing behavior of neonatal rat hypoglossal motoneurons," *J Neurophysiol*, vol. 69, pp. 2137-49, 1993.

[58] F. Viana, D. A. Bayliss, and A. J. Berger, "Multiple potassium conductances and their role in action potential repolarization and repetitive firing behavior of neonatal rat hypoglossal motoneurons," *J Neurophysiol*, vol. 69, pp. 2150-63, 1993.

[59] M. Umemiya and A. J. Berger, "Properties and function of low- and high-voltage-activated Ca2+ channels in hypoglossal motoneurons," *J Neurosci*, vol. 14, pp. 5652-60, 1994.

[60] M. Umemiya and A. J. Berger, "Single-channel properties of four calcium channel types in rat motoneurons," *J Neurosci*, vol. 15, pp. 2218-24, 1995.

[61] R. Lape and A. Nistri, "Current and voltage clamp studies of the spike medium afterhyperpolarization of hypoglossal motoneurons in a rat brain stem slice preparation," *J Neurophysiol*, vol. 83, pp. 2987-95, 2000.

[62] A. Sawczuk, R. K. Powers, and M. D. Binder, "Contribution of outward currents to spike-frequency adaptation in hypoglossal motoneurons of the rat," *J Neurophysiol*, vol. 78, pp. 2246-53, 1997.

[63] D. A. Bayliss, F. Viana, M. C. Bellingham, and A. J. Berger, "Characteristics and postnatal development of a hyperpolarization-activated inward current in rat hypoglossal motoneurons in vitro," *J Neurophysiol*, vol. 71, pp. 119-28, 1994.

[64] F. Viana, D. A. Bayliss, and A. J. Berger, "Postnatal changes in rat hypoglossal motoneuron membrane properties," *Neuroscience*, vol. 59, pp. 131-48, 1994.

[65] F. Viana, D. A. Bayliss, and A. J. Berger, "Repetitive firing properties of developing rat brainstem motoneurones," *J Physiol*, vol. 486 (Pt 3), pp. 745-61, 1995.

[66] C. A. Del Negro, S. M. Johnson, R. J. Butera, and J. C. Smith, "Models of respiratory rhythm generation in the pre-Botzinger complex. III. Experimental tests of model predictions," *J Neurophysiol*, vol. 86, pp. 59-74, 2001.

[67] I. A. Rybak, N. A. Shevtsova, K. Ptak, and D. R. McCrimmon, "Intrinsic bursting activity in the pre-Botzinger complex: role of persistent sodium and potassium currents," *Biol Cybern*, vol. 90, pp. 59-74, 2004.

[68] R. K. Powers, A. Sawczuk, J. R. Musick, and M. D. Binder, "Multiple mechanisms of spike-frequency adaptation in motoneurones," *J Physiol Paris*, vol. 93, pp. 101-14, 1999.

[69] W. C. Gerken, L. K. Purvis, and R. J. Butera, "Genetic algorithm for optimization and specification of a neuron model," *Neurocomputing*, vol. 69, pp. 1039-1042, 2006.

[70] M. C. Vanier and J. M. Bower, "A comparative survey of automated parameter-search methods for compartmental neural models," *J Comput Neurosci*, vol. 7, pp. 149-71, 1999.

[71] N. Keren, N. Peled, and A. Korngreen, "Constraining compartmental models using multiple voltage recordings and genetic algorithms," *J Neurophysiol*, vol. 94, pp. 3730-42, 2005.

[72] A. E. Tobin and R. L. Calabrese, "Endogenous and half-center bursting in morphologically inspired models of leech heart interneurons," *J Neurophysiol*, vol. 96, pp. 2089-106, 2006.

[73] Z. Syed, E. Vigmond, S. Nattel, and L. J. Leon, "Atrial cell action potential parameter fitting using genetic algorithms," *Medical and Biological Engineering and Computing*, vol. 43, pp. 561-571, 2005.

[74] B. Ermentrout, *Simulating, Analyzing, and Animating Dynamical Systems. A Guide to XPPAUT for Researchers and Students.* Philadelphia, PA: SIAM, 2002.

[75] J. Engel, H. A. Schultens, and D. Schild, "Small conductance potassium channels cause an activity-dependent spike frequency adaptation and make the transfer function of neurons logarithmic," *Biophys J*, vol. 76, pp. 1310-9, 1999.

[76] R. Bertram, "A computational study of the effects of serotonin on a molluscan burster neuron," *Biol Cybern*, vol. 69, pp. 257-267, 1993.

[77] V. Booth, J. Rinzel, and O. Kiehn, "Compartmental model of vertebrate motoneurons for Ca2+-dependent spiking and plateau potentials under pharmacological treatment," *J Neurophysiol*, vol. 78, pp. 3371-85, 1997.

[78] A. Nygren, C. Fiset, L. Firek, J. W. Clark, D. S. Lindblad, R. B. Clark, and W. R. Giles, "Mathematical model of an adult human atrial cell: the role of K+ currents in repolarization," *Circ Res*, vol. 82, pp. 63-81, 1998.

[79] R. A. Paulsen, Jr., J. W. Clark, Jr., P. H. Murphy, and J. A. Burdine, "Sensitivity analysis and improved identification of a systemic arterial model," *IEEE Trans Biomed Eng*, vol. 29, pp. 164-77, 1982.

[80] N. I. Kononenko, L. R. Shao, and F. E. Dudek, "Riluzole-sensitive slowly inactivating sodium current in rat suprachiasmatic nucleus neurons," *J Neurophysiol*, vol. 91, pp. 710-8, 2004.

[81] D. W. Robinson and W. E. Cameron, "Time-dependent changes in input resistance of rat hypoglossal motoneurons associated with whole-cell recording," *J Neurophysiol*, vol. 83, pp. 3160-4, 2000.

[82] A. L. Blatz and K. L. Magleby, "Single apamin-blocked Ca-activated K+ channels of small conductance in cultured rat skeletal muscle," *Nature*, vol. 323, pp. 718-20, 1986.

[83] R. K. Powers, "A variable-threshold motoneuron model that incorporates time- and voltage-dependent potassium and calcium conductances," *J Neurophysiol*, vol. 70, pp. 246-62, 1993.

[84] A. Sawczuk, R. K. Powers, and M. D. Binder, "Spike frequency adaptation studied in hypoglossal motoneurons of the rat," *J Neurophysiol*, vol. 73, pp. 1799-810, 1995.

[85] V. Booth and J. Rinzel, "A minimal, compartmental model for a dendritic origin of bistability of motoneuron firing patterns," *J Comput Neurosci*, vol. 2, pp. 299-312, 1995.

[86] S. E. Bowden, S. Fletcher, D. J. Loane, and N. V. Marrion, "Somatic colocalization of rat SK1 and D class (Ca(v)1.2) L-type calcium channels in rat CA1 hippocampal pyramidal neurons," *J Neurosci*, vol. 21, pp. RC175, 2001.

[87] M. Kobayashi, T. Inoue, R. Matsuo, Y. Masuda, O. Hidaka, Y. Kang, and T. Morimoto, "Role of calcium conductances on spike afterpotentials in rat trigeminal motoneurons," *J Neurophysiol*, vol. 77, pp. 3273-83, 1997.

[88] N. V. Marrion and S. J. Tavalin, "Selective activation of Ca2+-activated K+ channels by co-localized Ca2+ channels in hippocampal neurons," *Nature*, vol. 395, pp. 900-5, 1998.

[89] W. E. Cameron and P. A. Nunez-Abades, "Physiological changes accompanying anatomical remodeling of mammalian motoneurons during postnatal development," *Brain Res Bull*, vol. 53, pp. 523-7, 2000.

[90] A. J. Berger, D. A. Bayliss, and F. Viana, "Development of hypoglossal motoneurons," *J Appl Physiol*, vol. 81, pp. 1039-48, 1996.

[91] J. G. McLarnon, "Potassium currents in motoneurones," *Prog Neurobiol*, vol. 47, pp. 513-31, 1995.

[92] J. C. Rekling, G. D. Funk, D. A. Bayliss, X. W. Dong, and J. L. Feldman, "Synaptic control of motoneuronal excitability," *Physiol Rev*, vol. 80, pp. 767-852, 2000.

[93] S. Cullheim, J. W. Fleshman, L. L. Glenn, and R. E. Burke, "Three-dimensional architecture of dendritic trees in type-identified alpha-motoneurons," *J Comp Neurol*, vol. 255, pp. 82-96, 1987.

[94] S. Cullheim, J. W. Fleshman, L. L. Glenn, and R. E. Burke, "Membrane area and dendritic structure in type-identified triceps surae alpha motoneurons," *J Comp Neurol*, vol. 255, pp. 68-81, 1987.

[95] A. D. Lindsay, J. J. Greer, and J. L. Feldman, "Phrenic motoneuron morphology in the neonatal rat," *J Comp Neurol*, vol. 308, pp. 169-79, 1991.

[96] D. J. Withington-Wray, S. W. Mifflin, and K. M. Spyer, "Intracellular analysis of respiratory-modulated hypoglossal motoneurons in the cat," *Neuroscience*, vol. 25, pp. 1041-51, 1988.

[97] A. Mosfeldt Laursen and J. C. Rekling, "Electrophysiological properties of hypoglossal motoneurons of guinea-pigs studied in vitro," *Neuroscience*, vol. 30, pp. 619-37, 1989.

[98] F. Viana, L. Gibbs, and A. J. Berger, "Double- and triple-labeling of functionally characterized central neurons projecting to peripheral targets studied in vitro," *Neuroscience*, vol. 38, pp. 829-41, 1990.

[99] S. M. Altschuler, X. Bao, and R. R. Miselis, "Dendritic architecture of hypoglossal motoneurons projecting to extrinsic tongue musculature in the rat," *J Comp Neurol*, vol. 342, pp. 538-50, 1994.

[100] E. Mazza, P. A. Nunez-Abades, J. M. Spielmann, and W. E. Cameron, "Anatomical and electrotonic coupling in developing genioglossal motoneurons of the rat," *Brain Res*, vol. 598, pp. 127-37, 1992.

[101] P. A. Nunez-Abades and W. E. Cameron, "Morphology of developing rat genioglossal motoneurons studied in vitro: relative changes in diameter and surface area of somata and dendrites," *J Comp Neurol*, vol. 353, pp. 129-42, 1995.

[102] P. A. Nunez-Abades, F. He, G. Barrionuevo, and W. E. Cameron, "Morphology of developing rat genioglossal motoneurons studied in vitro: changes in length, branching pattern, and spatial distribution of dendrites," *J Comp Neurol*, vol. 339, pp. 401-20, 1994.

[103] L. K. Purvis and R. J. Butera, "Ionic current model of a hypoglossal motoneuron," *J Neurophysiol*, vol. 93, pp. 723-33, 2005.

[104] A. P. Davison, J. Feng, and D. Brown, "A reduced compartmental model of the mitral cell for use in network models of the olfactory bulb.," *Brain Res Bull*, vol. 51, pp. 393-399, 2000.

[105] C. M. Weaver and S. L. Wearne, "The role of action potential shape and parameter constraints in optimization of compartment models.," *Neurocomputing*, vol. 69, pp. 1053-1057, 2006.

[106] J. Tabak, C. R. Murphey, and L. E. Moore, "Parameter estimation methods for single neuron models," *J Comput Neurosci*, vol. 9, pp. 215-36, 2000.

[107] A. J. Chipperfield and P. J. Fleming, "The MATLAB Genetic Algorithm Toolbox," *IEE Colloquium on Applied Control Techniques Using MATLAB*, vol. 1995/014, 1995.

[108] G. B. Ermentrout, *Simulating, Analyzing, and Animating Dynamical Systems: A Guide to XPPAUT for Researchers and Students*. Providence, RI: SIAM, 2002.

[109] A. A. Prinz, C. P. Billimoria, and E. Marder, "Alternative to hand-tuning conductance-based models: construction and analysis of databases of model neurons," *J Neurophysiol*, vol. 90, pp. 3998-4015, 2003.

[110] Z. Liu, J. Golowasch, E. Marder, and L. F. Abbott, "A model neuron with activity-dependent conductances regulated by multiple calcium sensors," *J Neurosci*, vol. 18, pp. 2309-20, 1998.

[111] K. Ptak, G. G. Zummo, G. F. Alheid, T. Tkatch, D. J. Surmeier, and D. R. McCrimmon, "Sodium currents in medullary neurons isolated from the pre-Botzinger complex region," *J Neurosci*, vol. 25, pp. 5159-70, 2005.

[112] R. J. Butera, Jr., D. Terman, J. Rubin, and J. C. Smith, "Oscillatory bursting mechanisms in respiratory pacemaker neurons and networks.," in *Bursting: the genesis of rhythm in the nervous system*, S. Coombes and P. C. Bresloff, Eds.: , World Scientific Press, 2005, pp. 303-347.

[113] A. K. Tryba, F. Pena, and J. M. Ramirez, "Stabilization of bursting in respiratory pacemaker neurons," *J Neurosci*, vol. 23, pp. 3538-46, 2003.

[114] J. Streit, "Regular oscillations of synaptic activity in spinal networks in vitro," *J Neurophysiol*, vol. 70, pp. 871-8, 1993.

[115] M. J. O'Donovan, "Motor activity in the isolated spinal cord of the chick embryo: synaptic drive and firing pattern of single motoneurons," *J Neurosci*, vol. 9, pp. 943-58, 1989.

[116] F. Manseau, M. Danik, and S. Williams, "A functional glutamatergic neurone network in the medial septum and diagonal band area," *J Physiol*, vol. 566, pp. 865-84, 2005.

[117] M. A. Castro-Alamancos, P. Rigas, and Y. Tawara-Hirata, "~10 Hz resonance of excitatory networks in motor cortex: effects of voltage-dependent ion channel blockers," *J Physiol*, 2006.

[118] J. Tabak, W. Senn, M. J. O'Donovan, and J. Rinzel, "Modeling of spontaneous activity in developing spinal cord using activity-dependent depression in an excitatory network," *J Neurosci*, vol. 20, pp. 3041-56, 2000.

[119] A. K. Hammarstrom and P. W. Gage, "Hypoxia and persistent sodium current," *Eur Biophys J*, vol. 31, pp. 323-30, 2002.

[120] A. K. Hammarstrom and P. W. Gage, "Inhibition of oxidative metabolism increases persistent sodium current in rat CA1 hippocampal neurons," *J Physiol*, vol. 510 (Pt 3), pp. 735-41, 1998.

[121] E. M. Horn and T. G. Waldrop, "Hypoxic augmentation of fast-inactivating and persistent sodium currents in rat caudal hypothalamic neurons," *J Neurophysiol*, vol. 84, pp. 2572-81, 2000.

[122] P. Telgkamp and J. M. Ramirez, "Differential responses of respiratory nuclei to anoxia in rhythmic brain stem slices of mice," *J Neurophysiol*, vol. 82, pp. 2163-70, 1999.

[123] M. Thoby-Brisson, P. Telgkamp, and J. M. Ramirez, "The role of the hyperpolarization-activated current in modulating rhythmic activity in the isolated respiratory network of mice," *J Neurosci*, vol. 20, pp. 2994-3005, 2000.

[124] V. I. Krinskii and M. Kokoz Iu, "Analysis of the equations of excitable membranes. I. Reduction of the Hodgkins-Huxley equations to a 2d order system," *Biofizika*, vol. 18, pp. 506-11, 1973.

[125] J. Rinzel, "Excitation dynamics: insights from simplified membrane models," *Fed Proc*, vol. 44, pp. 2944-6, 1985.

[126] H. Onimaru, K. Ballanyi, and D. W. Richter, "Calcium-dependent responses in neurons of the isolated respiratory network of newborn rats," *J Physiol*, vol. 491 (Pt 3), pp. 677-95, 1996.

[127] S. L. Mironov and D. W. Richter, "L-type Ca2+ channels in inspiratory neurones of mice and their modulation by hypoxia," *J Physiol*, vol. 512 (Pt 1), pp. 75-87, 1998.

[128] S. L. Mironov and D. W. Richter, "Hypoxic modulation of L-type Ca(2+) channels in inspiratory brainstem neurones: intracellular signalling pathways and metabotropic glutamate receptors," *Brain Res*, vol. 869, pp. 166-77, 2000.

[129] B. Delord, "Diversity of firing frequency control by A-currents in vertebrate neurons: a modeling study," *Neuroreport*, vol. 10, pp. 2773-7, 1999.

VITA

Liston Keith "Luke" Purvis grew up in the small town of Raymond, Mississippi. During his childhood he enjoyed riding bikes around town with his friends, swimming at the local pool, spending time with his family (including many "2nd-Sundays"), playing with his cousin and brother, and annoying his sister. He attended Carver Elementary School and Raymond High School. After a brief stint playing high school baseball under Coach "Moose" Perry, Luke graduated from Raymond High in 1995 and started college across the street at Hinds Community College – where he met his future wife, Deborah. Luke transferred to Mississippi State University in 1997, married Deborah in 1999, and graduated with a B.S. in electrical engineering in 2000. Luke attended graduate school at the Georgia Institute of Technology. At Georgia Tech he received an M.S. in electrical engineering in 2004 and a Ph.D. in bioengineering in 2006. While in graduate school, Luke had 2.5 wonderful children: Peyton, Keith, and baby #3. Luke's future plans include loving and spending time with his family and devoting his career to making the world a better place.